

Upgrades to the Fluorescence Detectors of the Pierre Auger Observatory



THE UNIVERSITY
*of*ADELAIDE

Tristan William Sudholz

School of Physical Sciences
University of Adelaide

This dissertation is submitted for the degree of
Doctor of Philosophy

February, 2021

Declaration

I, Tristan William Sudholz, certify that this work contains no material which has been accepted for the award of any other degree or diploma in any university or other tertiary institution and, to the best of my knowledge and belief, contains no material previously published or written by another person, except where due reference has been made in the text. In addition, I certify that no part of this work will, in the future, be used in a submission for any other degree or diploma in any university or other tertiary institution without the prior approval of the University of Adelaide and where applicable, any partner institution responsible for the joint-award of this degree.

I give consent to this copy of my thesis, when deposited in the University Library, being made available for loan and photocopying, subject to the provisions of the Copyright Act 1968.

I also give permission for the digital version of my thesis to be made available on the web, via the University's digital research repository, the Library catalogue and also through web search engines, unless permission has been granted by the University to restrict access for a period of time.

Tristan William Sudholz

Abstract

Acknowledgements

Contents

Nomenclature	xiii
Introduction	1
1 Cosmic-Rays	3
1.1 History of Cosmic-Rays	3
1.2 Energy Spectrum and Mass composition	3
1.3 Production Method and Sources	5
2 Detection of Cosmic-rays	7
2.1 Extensive Air Showers	7
2.2 Electromagnetic Component	8
2.3 Hadronic Component	9
2.4 Fluorescence Production	9
2.5 Atmospheric Effects	11
2.6 Detectors and History	11
3 Pierre Auger Observatory	13
3.1 Surface Detector	13
3.1.1 AugerPrime	13
3.2 Fluorescence Detector	13
3.2.1 Photomultiplier Tubes	16
3.3 Communication System and CDAS	16
3.4 Event Reconstruction	16
3.4.1 Surface Detector	16
3.4.2 Fluorescence Detector	16
3.5 Enhancements and future upgrades	16
4 The Effects of Increased NSB on the FD Trigger and Reconstruction	17
4.1 Motivation	17
4.2 Background Information	17
4.2.1 Current Fluorescence Detector Operation	17
4.2.2 Night Sky Background and the Moon	22
4.2.3 Toy Model of the effect of increased NSB on aperture	22
4.3 Increasing NSB in Real Data to evaluate Reconstruction Efficiency	29
4.3.1 Method	29
4.3.2 Results	33
4.3.3 Discussion	33

4.4	Increasing NSB in Simulations to evaluate Trigger/Reconstruction Efficiency	33
4.4.1	Method	33
4.4.2	Comparison of Simulated Data to Real Data	36
4.4.3	Results	36
4.4.4	Discussion	36
4.5	Conclusion/Summary	36
5	Quantifying Characteristics of the FD PMT	41
5.1	Motivation	41
5.2	Background	41
5.3	PMT Linearity	42
5.3.1	Neutral Density Filters	42
5.3.2	Two LED Method	42
5.4	Effects of Temperature on PMT Gain	45
6	Computer Simulation of FD PMT	49
6.1	Motivation	49
6.2	Method and Theory	49
6.2.1	Theoretical value of Gain Variance?	50
6.3	Results of PMT Gain Variance Simulation	50
6.4	Simulation of Gain Variance Method	50
6.5	FD FLT under different NSB levels	50
7	Measuring FD PMT Gain Variance with CalA Data	57
7.1	Motivation	57
7.2	Using CalA to measure relative changes in Gain Variance	57
7.3	Electronic Noise	58
7.4	Pairs Method	58
7.4.1	Results	60
7.5	Averaging Sets of Traces Method	60
7.5.1	Results	60
7.6	Result of Averaging Sets of Traces Method with Least Trimmed Squares	69
7.7	Result of Averaging Sets of Traces Method using Noise Distribution	69
7.8	Attempts to measure Gain Variance directly in the Lab	69
8	Results of FD PMT Gain Variance from CalA Data	73
9	Laboratory Simulation of FD shift	75
9.1	Motivation	75
9.2	Method and equipment set-up	75
9.3	Results	75
9.4	Discussion	75
9.5	Conclusion	75
10	Evaluation of Cloud Cuts on Auger Event Data	77
10.1	Equipment used to detect cloud over the array	77
10.2	Method - Cloud Flags and Their Impact	77
10.3	Results - Effect on Mean Xmax and Spread in Xmax	79

10.4 Discussion - Are we being too conservative?	79
10.5 Conclusion	79
11 Conclusion	87
11.1 Future Work	87
Bibliography	89

Nomenclature

PAO	Pierre Auger Observatory
EAS	Extensive Air Shower
NSB	Night Sky Background
PE	Photo-electron
FD	Fluorescence Detector
SD	Surface Detector
PMT	Photomultiplier Tube
FLT	First Level Trigger

Introduction

- Define Cosmics Rays.
- The origins of the highest energy cosmic-rays still unknown.
- First detection by Pierre Auger in 1937 and the current detector looking at these energies is the Pierre Auger Observatory.
- Hybrid experiment containing both surface detectors and fluorescence detectors
- Surface detector has nearly 100% up-time while the fluorescence detectors only have 15% up-time.
- **** Proposal to extend the fluorescence detector up-time. To achieve this will have to operator while the moon is above the horizon. This will increase the level NSB and will have the PMTs run under a reduced gain to compensate. ****
- Photomultiplier Tubes are used as pixels within the camera of the fluorescence detectors and the aim of these thesis is to quantify the characteristics of the PMT under the reduced gain and increased.
- Outline a Summary of each chapter.

Cosmic-rays are particles that originate outside of the Earth atmosphere. These particles can be photons, hadronic or leptonic in nature [ref?]. In this thesis, when mentioning cosmic-rays I will mean the hadronic component unless specified otherwise. Cosmic-rays have been measurement over a large range of energies (over 6 decades in energy) and it has many interesting features have been observed in this energy spectrum. One of the longest running mysteries is what happens at the highest energy. Since the first detection of extensive air showers by Pierre Auger in 1937 [ref], many different experiments have endeavoured to solve this mystery. The Pierre Auger Observatory [ref] is currently in operation to observe cosmic-rays at the highest energies.

The Pierre Auger Observatory is a hybrid experiment consisting of both surface detectors and fluorescence detectors. (Outline location) The surface detector has a nearly 100% operation up-time ref while the fluorescence detectors only 15% operation up-time [ref]. (Outline how Auger detects cosmic-rays, just need a brief summary).

A current proposal to extend the fluorescence detector operation up-time. Extended up-time would be beneficial as the fluorescence detectors image the entire extensive air shower and would increase the number of showers observed through out yearly observation. To achieve the extended operation the fluorescence detectors would have to operated while the moon is above the horizon. While the moon is up, this would increased the Night Sky Background level and to compensate the Photomultiplier Tubes acting as the camera pixels would have to be run under reduced gain.

- Need graph of expected variance in ADC² for the moon above the horizon for different phases.

- Want to increase the duty cycle of FD by measuring EAS under moonlight. Most likely observe under quarter to half moon. This will increase the NSB upto a factor of 10.

- The aim of increasing the duty cycle of FD is to measure more EAS at the highest energy band ($> 10^{19.5}$ eV).

- Need more statistics at highest energy band to complement SD measurements.

The aim of this thesis is to quantify the characteristics of the Photomultiplier Tubes operating under this reduced gain and outline any operation strategies. Outline of each chapter is as follows:

- Chapter 1: Cosmic-rays

Does this work as a new line

- Chapter 2: Detection of Cosmic-Rays

Add text here

- Chapter 3: The Pierre Auger Observatory

Add text here

- Chapter 4 : Extensive Air Shower Selection Efficiency with Increased Night Sky Background

Add text here

- Chapter 5 : Quantifying Characteristics of the Fluorescence Detector Photomultiplier Tubes

Add text here

- Chapter 6 : Computer Simulation of the Fluorescence Detector Photomultiplier Tubes

Add text here

- Chapter 7 : Measuring Gain Variance of the Fluorescence Detector Photomultiplier Tubes with CalA data

Add text here

- Chapter 8 : Results of Measuring the Gain Variance of the Fluorescence Detector Photomultiplier Tubes

Add text here

- Chapter 9 : Laboratory Simulation of Fluorescence Detector Shifts

Add text here

- Chapter 10 : Effectiveness of Cloud Camera Cuts on Data Set

Add text here

- Chapter 11: Conclusion

Future Work

Chapter 1

Cosmic-Rays

1.1 History of Cosmic-Rays

First detection of ionizing radiation.

1785: Coulomb found that electroscopes can spontaneously discharge by the action of the air and not by defective insulation

1835: Faraday confirms the observation by Coulomb, with better insulation technology

1879: Crookes measures that the speed of discharge of an electroscope decreased when pressure was reduced

Cosmic-rays are particles that have arrived at Earth from outer space. These particles consist mainly of atomic nuclei ranging from protons to iron nuclei, with electrons and γ -rays making up less than 1% of the total flux [?]. The range of detected particles cover a huge range of energies from less than 10^{12} eV to greater than 10^{20} eV (the flux below $\sim 10^{11}$ eV is suppressed by the presence of the sun's magnetic field).

The discovery of cosmic-rays is attributed to Victor Hess in 1912 [?]. In a series of balloon flights Hess showed that the observed ionising radiation increased with altitude. From these measurements he concluded that a radiation of very high penetrating power enters the atmosphere from above. It has come to light recently [?] that another physicist D. Pacini also drew a similar conclusion in 1912 [?]. Instead of measuring the ionising radiation above the ground, Pacini conducted measurements below sea level by descending in the sea in the Bay of Livorno.

1938: High energy cosmic-rays detected by Pierre Auger

1.2 Energy Spectrum and Mass composition

Cosmic-rays have been detected over a large range of energies from GeV (10^9 eV) to above EeV (10^{18} eV). Spectrum in Figure 1.1 shows the break at the knee and ankle and which type of experiments are most suited to measurement each part. Cosmic-ray spectrum starts out at E^{-2} and can be as steep as $E^{-2.7}$ at the highest energies.

Cosmic-rays can consist of protons to iron.

CR spectrum has many feature. Main features are the knee, second knee and ankle. The knee is around 3×10^{15} .

Pierre Auger Observatory measurement of isotropy that shows that the cosmic-ray spectrum changes from predominately galactic to extra-galactic at the ankle.

Predicted Greisen-Zatsepin-Kuzmin (GZK) cut-off about 6×10^{19} . Cosmic-rays above this energy are theorised to interact with the cosmic microwave background radiation. Greisen

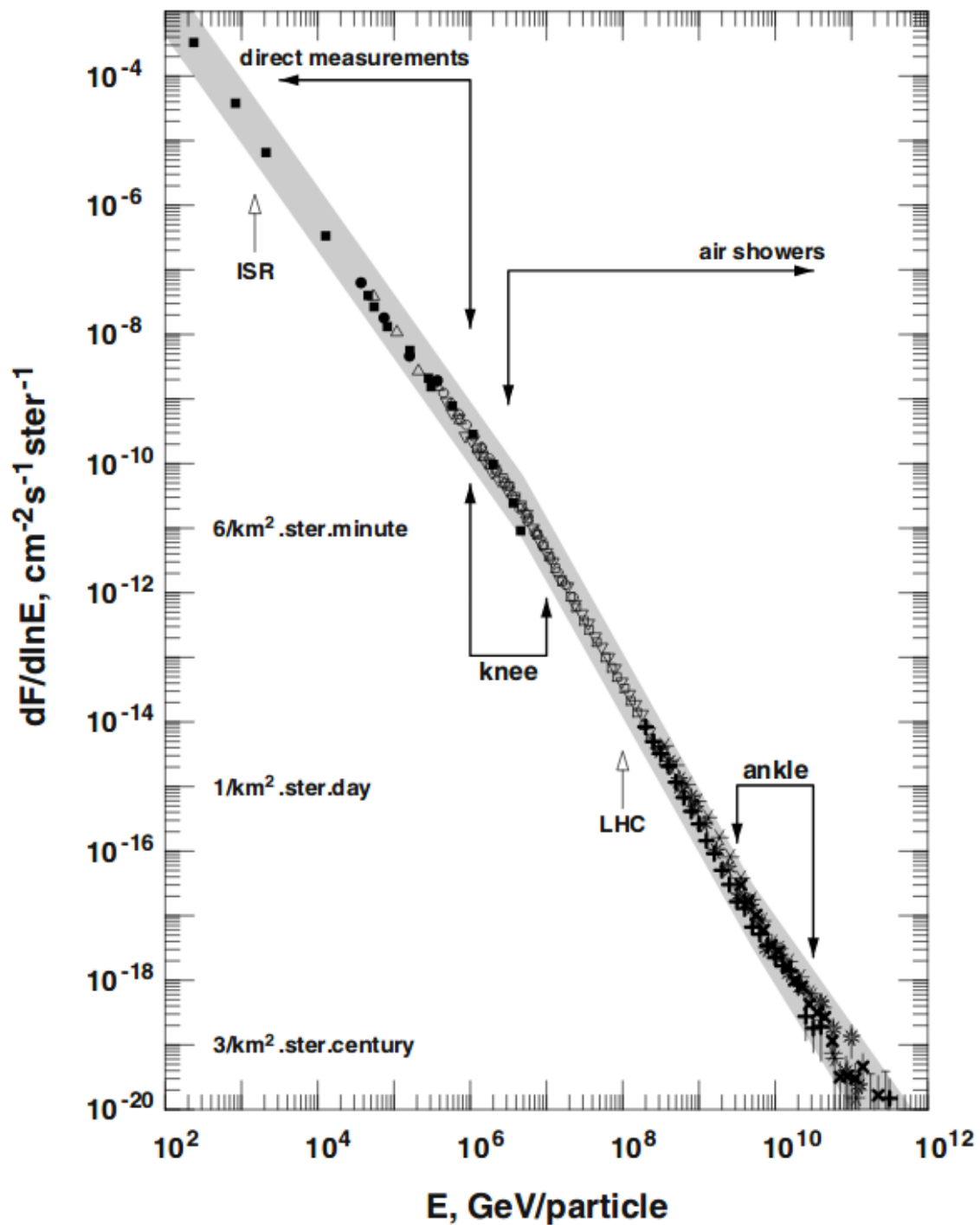


Figure 1.1: Measured energy spectrum of cosmic-rays from 100 GeV up to the highest detected energy.

independently of Kuz'man and Zatsepin all predicted this energy loss.

Pierre Auger Observatory measurement of X_{max} and the second moment $\sigma(X_{\text{max}})$ has mass composition information as well how this changes as a function of energy.

Mechanisms involved must be able to accelerate cosmic-ray particles to energies exceeding 10^{20} eV. The acceleration region must have the size of the order of the Larmor radius (r_L) to be capable of producing a particle of this energy. The Larmor radius is calculated

$$r_L = \frac{p_{\perp}}{Zq_eB} \quad (1.1)$$

where Z is the atomic number of the particle, p_{\perp} is the momentum perpendicular to the magnetic field, B is the magnetic field strength and q_e is the charge of an electron. There are two possible categories of acceleration: Bottom-Up processes and Top-Down processes.

Bottom-Up processes are where low energy particles are accelerated up to higher energy particles. Proposed bottom-up scenarios include stochastic acceleration. Stochastic acceleration of charged particles was first suggested by Enrico Fermi in 1949. It involves the repeated interaction of charged cosmic-rays with moving clouds of magnetised plasma in the interstellar medium. Magnetised clouds move with random velocities and charged cosmic-rays have a chance of either gaining or losing energy during an interaction. This process can explain the observed power law energy spectrum of cosmic-rays.

Top-Down processes are proposed mechanisms where ultra high energy cosmic-rays do not obtain their energy from an acceleration process. Their energy is imparted to these particles via the decay of supermassive ($m_X > 10^{20}$ GeV) relic particles from the Big Bang. These relic particles are known generically as 'X' particles. X particles decay into quarks and leptons. The quarks can then form jets of pions, with a small proton component. The top-down mechanisms are able to produce ultra high energy cosmic-rays with energies up to m_X , however they also predict the production of copious quantities of high energy photons and neutrinos.

Cosmic-rays lose energy as they travel throughout the universe. For protons the main energy loss is through photoproduction on astrophysical photon fields. For cosmic-rays with energies around 10^{20} eV, they can interact with any photon field. The most common and better known photon field is the Cosmic Microwave Background radiation. For nuclei, photo-disintegration can also occur, which results in the ejection of one or more nucleons from the nucleus.

1.3 Production Method and Sources

- Bottom-Up Acceleration

- Supernova explosions

- AGN jets

- other energetic processes

- dark matter annihilations.

- Top-Down Acceleration

- Decay of massive relic particles

- Typically associated with new physics beyond the standard model

Chapter 2

Detections of Cosmic-Rays

2.1 Extensive Air Showers

Use Earth's atmosphere as an interaction medium. Primary particle interacts with the molecules in the atmosphere to produce a cascade of secondary particles. This cascade of particles is referred to as an Extensive Air Shower (EAS). Hadronic primaries can produce pions, muons and other stuff. Mixture of a hadronic core with an electromagnetic component from the decay of π^0 .

Shower profile has particles produced until energy on individual secondary particles drop below the ionization threshold. Therefore the shower will reach a point of maximum particle number then will drop off.

Above energies of 100 TeV (10^{14} eV) direct detection becomes increasingly difficult [?]. Ground based observations are made by exploiting extensive air showers (EAS). EAS were first discovered by Pierre Auger in 1932 when noticed that cosmic-rays were arriving at different detectors at the same time. He formed the conclusion that they were secondary particles emitted from the same source [?].

An extensive air shower is a cascade of secondary particles that begins when the cosmic ray first interacts with the earths atmosphere. Three main components of an extensive air shower are:

- Electromagnetic - consisting of electrons, positrons and γ -rays resulting from the decay of charged and neutral pions and kaons.
- Hadronic component - consisting of heavy nuclei, charged pions and kaons.
- Muonic - consisting of muons and neutrinos resulting from the decay of charged pions and kaons.

The height at which cosmic rays interact within the atmosphere is dependent on their energy and composition. A measure of the amount of atmospheric matter above ground level is called the atmospheric or slant depth X . The unit of slant depth is usually g/cm². To calculate the slant depth, firstly need to define a vertical atmospheric depth.

$$X_v = \int_h^\infty \rho(h') dh' \quad (2.1)$$

where X_v is the vertical atmospheric depth and ρ is the atmospheric density. Now a slant depth can be defined.

$$X = \frac{X_v}{\cos(\theta)} \quad (2.2)$$

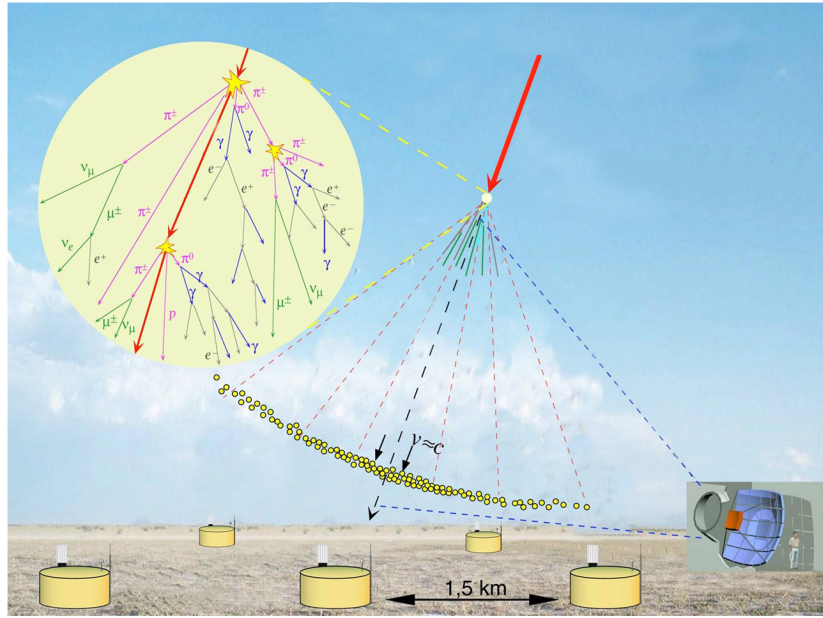


Figure 2.1: Diagram of Cosmic-ray Extensive Air Showers.

where θ is the angle from the zenith. Shower age s is a parameter often used to describe the development of an extensive air shower relative to shower maximum. The slant depth at which shower maximum occurs is defined as depth of maximum development (X_{max}). Shower age is defined as

$$s(X) = \frac{3}{(1 + 2X_{max}/X)} \quad (2.3)$$

2.2 Electromagnetic Component

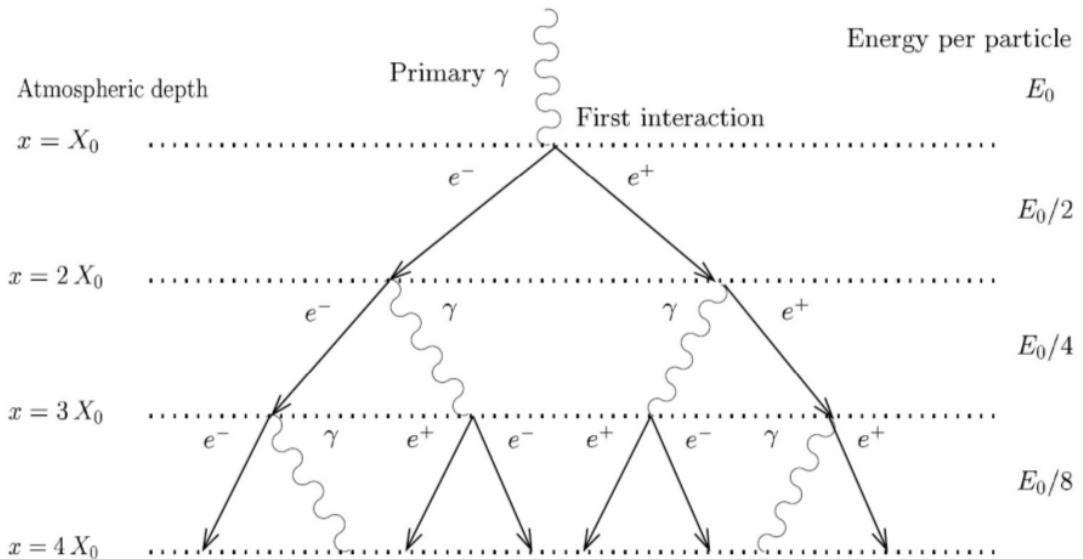


Figure 2.2: A graphical representation of the Heitler model.

To describe the electromagnetic shower, a simple model was proposed by Heitler [1]. In this model a γ -ray of E_0 interacts with an atmospheric nucleus (N), creating an electron-positron pair via pair-production

$$\gamma + N \rightarrow e^+ + e^- \quad (2.4)$$

Each of the electron and positron then give half of their energy to γ -ray via bremsstrahlung

$$e^\pm + N \rightarrow N + e^\pm + \gamma \quad (2.5)$$

This process continues as shown in Figure 2.2 until the energy of the particles falls below the critical energy E_C required for further particle production, and ionisation begins to dominate.

The energy of each shower particle after n radiation lengths will be

$$E(n) = \frac{E_0}{2^n} \quad (2.6)$$

Once the individual particles energy drops below the energy where ionisation dominates no more particles are produced. Therefore the maximum particle number is

$$N_{max} = \frac{E_0}{E_C} \quad (2.7)$$

2.3 Hadronic Component

A hadronic EAS is initiated the same way in the atmosphere as a electromagnetic shower but the interaction produces kaons and charged and neutral pions [?]. An approach similar to Heitler's treatment of electromagnetic cascades can be used to explain the basic properties of hadronic cascades. The atmospheric is divided into layers, with the thickness of each layer characterised by an interaction length λ_I . After travelling one interaction length, the primary hadron interacts with the atmosphere and produces $2N$ charged pions and N neutral pions. The neutral pions decay into two photons

$$\pi^0 \rightarrow \gamma + \gamma \quad (2.8)$$

These photons can initiate electromagnetic cascades, and the charged pions becoming the next generation of the hadronic shower. The process continues until the energy of the pions drops below a critical energy $E_{crit}^I \approx 20$ GeV. The critical energy is the point where the decay length becomes shorter than the interaction length. At this threshold, the charged pions decay

$$\pi^+ \rightarrow \mu^+ + \nu_\mu \quad (2.9)$$

$$\pi^- \rightarrow \mu^- + \bar{\nu}_\mu \quad (2.10)$$

2.4 Fluorescence Production

The charge particles of EAS interact with the nitrogen molecules in the atmosphere. This interaction turns the nitrogen molecule dipole like and when the nitrogen returns to a ground state, a photon is emitted. This emitted photon is termed fluorescence light. Fluorescence light is can be emitted isotropically and typically in the UV band (between 300 and 400 nm). *** Show wavelength profile ***

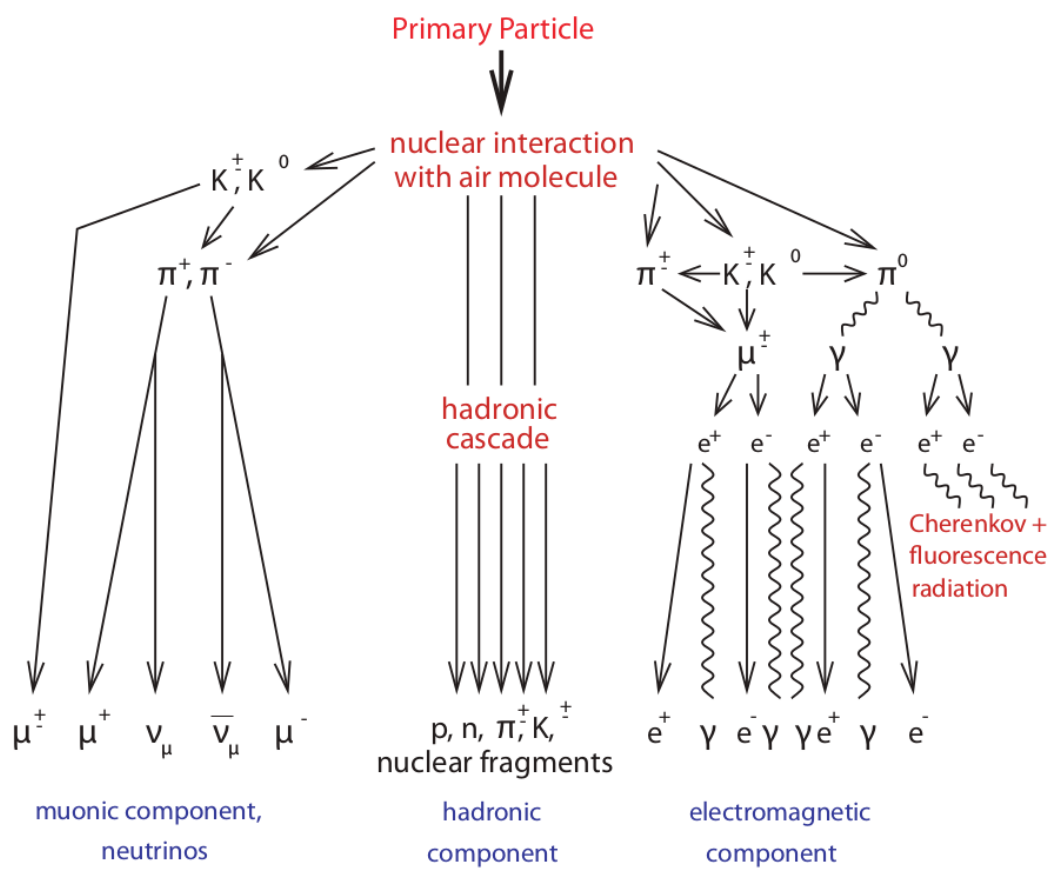


Figure 2.3: A graphical representation of the Heitler model for an extensive air shower initiated by a hadronic primary. Image taken from [?].

2.5 Atmospheric Effects

2.6 Detectors and History

Volcano Ranch 1959 until 1963. First giant air shower array, located near Albuquerque, New Mexico. The array consisted of nineteen detectors located on a triangular grid, with an additional 20th detector being used in several different position throughout operation. For some of the operating period, the 20th detector was shielded by 10 cm of lead to investigate the penetrating (mounic) component of extensive air showers. Each detector was a 3.3 m² plastic scintillator viewed by a 5 inch photomultiplier tube. The array was operated in two configurations: first used with spacing of 442 m (covering 2 km²) and later increased to a spacing of 884 m (covering 8 km²).

Haverah Park 1968 until 1987. A 12 km² ground array located at Haverah Park, England. This experiment used water Cherenkov tanks. The irregular design of the array was a consequence of limited land access which dictated the placement of detectors.

SUGAR (Sydney University Giant Airshower Recorder) 1968 until 1979. Located in the Pilliga State Forest, New South Wales, Australia. SUGAR was the first large detector to operate in the southern hemisphere (Pierre Auger Observatory being the second). At its peak operation, SUGAR consisted of 47 detectors situated over an area of approximately 70 km². The majority were located on a square grid of 1600 m spacing, with some detectors located on a smaller grid of either 800 or 400 m spacing to gather data on smaller showers. Each detector consisted of two liquid-scintillators separated by 50 m and buried approximately 1.5 m underground.

Yakutsk 1970 until present. Located in Yakutsk, Russia. It has undergone many reconfigurations throughout the years. An expansion in 1974 achieved a collecting area of approximately 18 km², but it was down sized in 1995 to cover about 10 km². Yakutsk contains scintillation detectors and up-ward facing PMTs. The up-ward facing PMTs are unique to Yakutsk (in terms of giant air shower arrays), that are used to detect the atmospheric Cherenkov light produced by EAS, from which a calorimetric estimation of primary energy can be made.

Fly's Eye (I and II) 1981 until 1992. While not the first detector to use the air fluorescence technique, it was the first detector to successfully detect large quantities of events. The first of two Fly's Eye detectors was built at Dugway Proving Grounds, Utah, approximately 160 km from Salt Lake City. Fly's Eye I began taking data in 1981, with a second detector, Fly's Eye II, was built 3.3 km away from Fly's Eye I and began operation in 1986. Both detectors consisted of PMTs to detect the fluorescence light emitted by atmospheric nitrogen.

AGASA (Akeno Giant Air Shower Array) 1990 until 2004. Prior to the construction of the Pierre Auger Observatory, AGASA was the largest air shower array in the world. It was located 120 km west of Tokyo, Japan. Originally divided into four separate branches, AGASA was unified in 1995 to operate as a single detector. Construction of the main array began in 1987, with the smaller arrays located at the site having been constructed earlier. Data collection started in 1990 and continued until January 2004. AGASA covered approximately 100 km² with 111 2.2 m² plastic scintillator detectors spaced approximately 1 km apart.

HiRes (High Resolution Fly's Eye) 1997 until 2006. The High Resolution Fly's Eye observatory (HiRes) was the successor to the Fly's Eye experiment. It was located in the same place as its predecessor at the Dugway Proving Grounds in Utah. Two detectors named HiRes I and II comprised the experiment and began operation in 1997 and 1999 respectively.

The two site were separated by a distance of 12.6 km.

Chapter 3

Pierre Auger Observatory

Science Goals of the Pierre Auger Observatory is to probe the origins and characteristics of cosmic rays above 10^{17} eV and to study the interactions of the most energetic particles observed in nature.

The Pierre Auger Observatory (PAO) is an hybrid detector that is located near Malargüe in the Mendoza Province, Argentina. PAO consists of 1660 Cherenkov water detector spread over 3000 km² by 24 fluorescence telescopes.

3.1 Surface Detector

The surface array consists of 1660 water Cherenkov tanks. The majority of tanks are configured with a spacing of 1500 metres while there is a small subset of tanks in front of the fluorescence telescopes at the Coihueco site with spacing of 750 metres.

The surface array has a duty cycle of nearly 100% and the maintenance cycle is so that no more then 20 tanks are down at any one time.

3.1.1 AugerPrime

3.2 Fluorescence Detector

There are four fluorescence detector site surrounding the surface array. At each fluorescence detector site there are six telescopes covering 180° in azimuth and 30° in elevation. At one site there are three extra telescopes with slightly greater then 90° in azimuth and cover 30° to 60° in elevation.

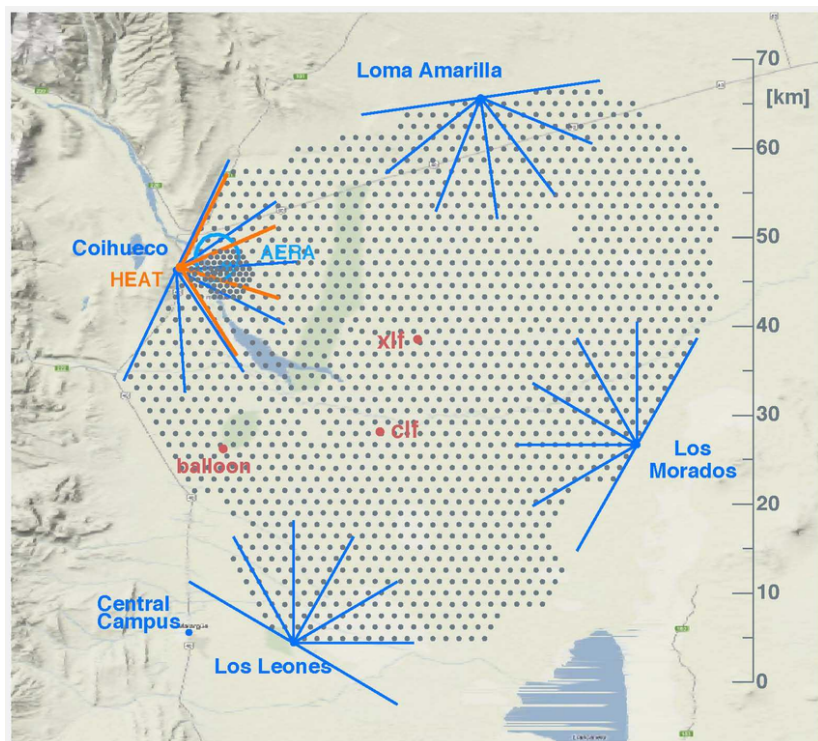


Figure 3.1: Image of layout of Pierre Auger Observatory located near Malargüe, Argentina.



Figure 3.2: Image of one of the fluorescence detector site (background) and one of the surface detectors (foreground).

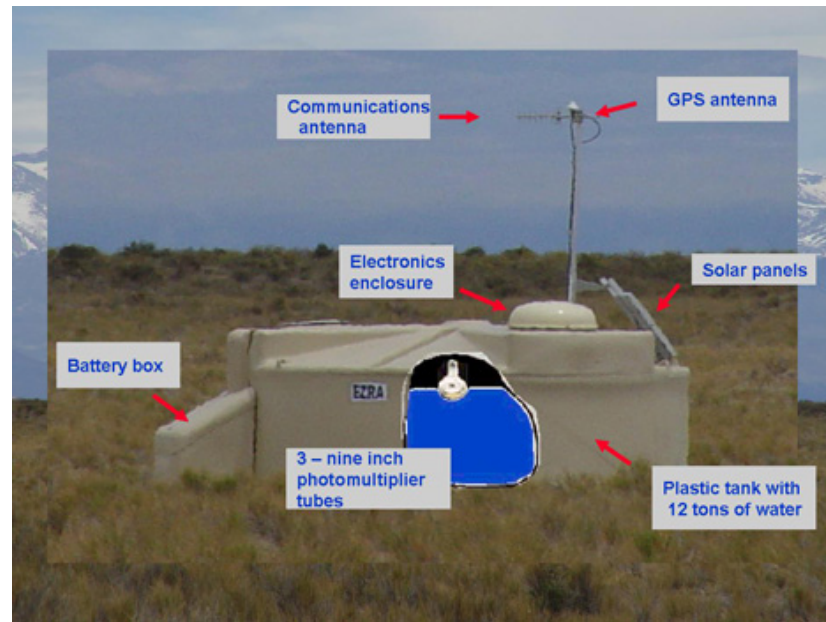


Figure 3.3: Basic schematic of a surface detector.

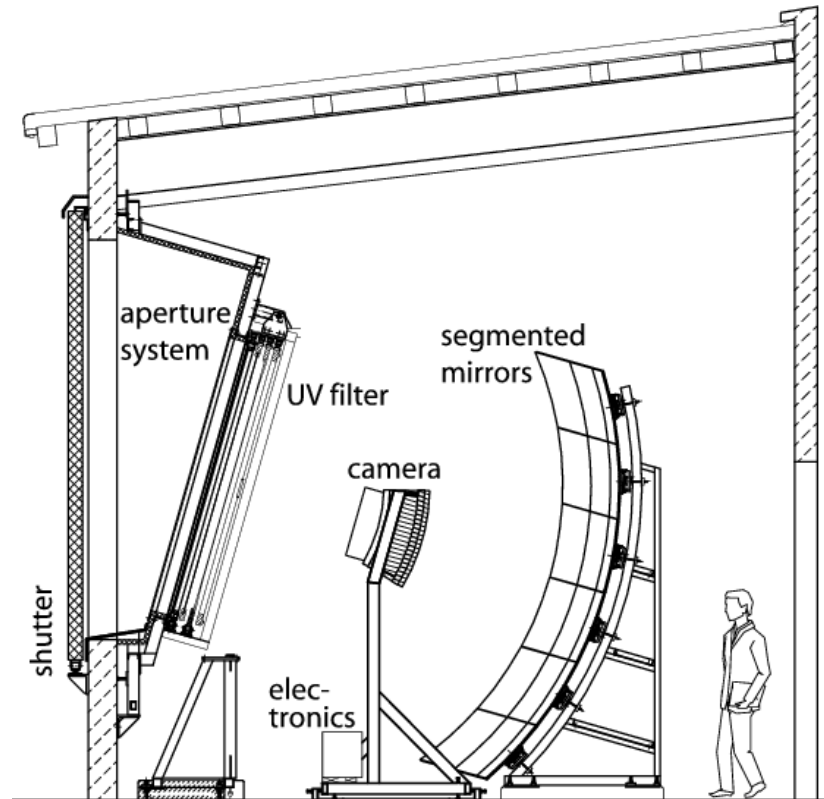


Figure 3.4: Basic schematic of a fluorescence telescope.

3.2.1 Photomultiplier Tubes

3.3 Communication System and CDAS

3.4 Event Reconstruction

3.4.1 Surface Detector

3.4.2 Fluorescence Detector

3.5 Enhancements and future upgrades

Chapter 4

The Effects of Increased Night Sky Background on the Fluorescence Detector's Trigger and Reconstruction

4.1 Motivation

The Pierre Auger Observatory has been operational since 2004 and the Collaboration is in the process of rolling out upgrades to improve the experiment. The current upgrade has been name AugerPrime ([ref](#)) and is a large project to improve both the Surface Detectors (SD) and the Fluorescence Detectors (FD). The FD portion of AugerPrime involves extending the duty cycle to observe Extensive Air Shower (EAS) events while the moon is above the horizon. The main purpose for extending the FD duty cycle to include observation times while the moon is visible is to increase the statistics per year for EAS events at the highest energy ($> 10^{19.5}$ eV).

In this chapter I use real data events and simulations to explore the effects of increasing the Night Sky Background (NSB) on the collaboration's reconstruction method and trigger efficiency. A real data set was used to evaluate the efficiency of the reconstruction method under different NSB intensities by artificially adding extra noise to signal traces. This method follows a study done by M. Unger [Find ref.](#). The method from M. Unger study was used as a basis. The results where examined in depth and found to mainly test the robustness of the collaboration's reconstruction algorithm. This analysis led to the use of the collaboration FD simulations to evaluate the effects of the increased NSB on both the FD triggers and reconstruction efficiency.

4.2 Background Information

4.2.1 Current Fluorescence Detector Operation

Currently an Fluorescence Detector (FDs) run is organised for nights when the illuminated fraction of the moon is less than 70% and the night has a minimum of 3 hours of operation with the moon below the horizon. The FD telescope shutters are opened when the sun is below -18° of the horizon (beginning of astronomical twilight). The FD shutters remain open while the average variance across the FD camera is less than $100 \text{ ADC}^2/100 \text{ ns}$ and

the variance of no individual pixels (which are photomultiplier tubes) is greater than 2000 ADC²/100 ns. ADC units is the digitised of the photomultiplier tube (PMT) anode signal in electrons to Analogue-to-Digital Converter (ADC) units and 100 ns is chosen as the time interval that the ADC is digitised over. The FD shutters at each site automatically close if the individual rain sensors are triggered or the measured wind speed is above 50 km/h at the individual FD sites. Using these guidelines the expected yearly FD duty cycle can be calculated. This calculation was performed by the collaboration in **DATE & ref** to estimate the theoretical the FD duty cycle and the result is shown in Table 4.1. Bad weather is mainly caused by rain, high wind speeds or lightning strikes in the FDs field of view. Failures include any software or hardware issues that prevented any of the FD telescopes from collecting data.

Theoretical up time	22%
Loss due to short nights (< 3 hrs)	-2%
Loss due to bad weather or failures	-5%
Total measurement time	15%

Table 4.1: Calculation of the yearly expected FD duty cycle done by the Collaboration. Bad weather is the inclusion of rain, high wind speeds and lightning strikes in the FDs field of view. Failures include any software or hardware issues that prevented any of the FD telescopes from collecting data.

Photons that enter the FD telescope pass through the optics, are converted to photo-electrons by PMT and are then converted to Analogue-to-Digital Converter units by the electronics. A basic diagram of how photons detected by an FD telescope are converted to ADC is shown in Fig. 4.1. The steps are split into 3 parts: the optics, PMT and electronics. When the photon reaches the PMT it produces a photo-electron and the electron signal from the PMT is converted to ADC units by the electronics.

The electron signal from the FD PMT is AC coupled, which means the average ADC of the NSB is zero. Instead the ADC variance is used to measure the number of photons at the diaphragm. When converting a NSB trace into a NSB photon count the NSB ADC variance is proportional to the variance in the NSB photon count. To find the ADC variance due to the NSB the electronic noise has to be removed from the background ADC variance traces. Removal of the electronic noise is achieved by using Eq. 4.1.

$$[\sigma_{\text{ADC}}^2]^{\text{sky}} = [\sigma_{\text{ADC}}^2]^{\text{back}} - [\sigma_{\text{ADC}}^2]^{\text{elec}} \quad (4.1)$$

where:

$[\sigma_{\text{ADC}}^2]^{\text{sky}}$ is the variance (ADC²/100 ns) caused by the NSB.

$[\sigma_{\text{ADC}}^2]^{\text{back}}$ is the variance (ADC²/100 ns) of background signal which is the combination of NSB and electronic noise.

$[\sigma_{\text{ADC}}^2]^{\text{elec}}$ is the variance (ADC²/100 ns) of the electronic noise. The variance of FD electronic noise is measured while the shutters are closed.

The typical mean ADC variance of the NSB measured by Auger ?? at Malargue is:

$$[\sigma_{\text{ADC}}^2]^{\text{sky}} = 25 \text{ ADC}^2 / 100 \text{ ns}$$

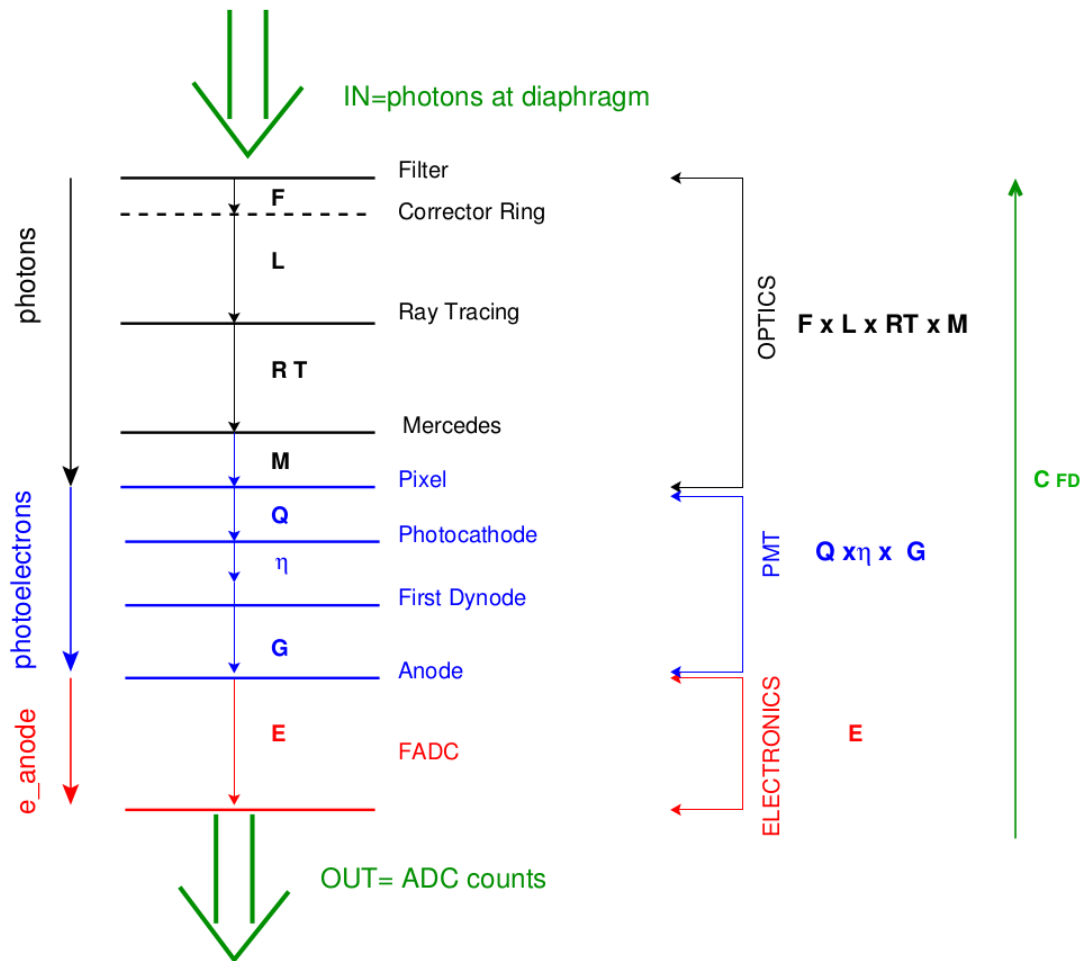


Figure 4.1: A diagram showing the steps that a photon passing through an FD telescope diaphragm will travel to be convert to an ADC. The steps are split into 3 parts: the optics, PMT and electronics. When the photon reaches the PMT it is converted to a photo-electron and the electron signal from the PMT anode is converted to ADC units by the electronics. - Define all of the symbols.

The variance in ADC² seen by the FD can be converted back to photon numbers at the diaphragm by the FD pixel calibration constant C_{FD} (photons/ADC units). The FD pixel calibration constant has been determined by illuminating the diaphragm with a known number of photons. This was originally done by a drum calibration which used a large device that covered the entire FD diaphragm and could illuminate the whole camera with a known number of diffuse photons. The drum calibration has now been retired and has been replaced with an experiment called the XY scanner [ref]. The XY scanner illuminates one pixel at the time and scans over the entire camera. The advantages of the XY scanner is that it is a more compact experiment with the aim of having the ability to be deployed more often to find the absolute calibration.

The FD pixel calibration factor C_{FD} can be used to find the variance of the NSB photons at the diaphragm from the measured ADC variance. An average variance of the NSB measured by an FD telescope under standard operational guidelines is σ_{ADC}² = 25 ADC² / 100 ns. The calculations to work out the variance of the photon count (RMS_{ph} / 100 ns) from the measured variance in ADC² is as follows:

$$\sigma_{\text{ph}}^2 = (C_{\text{FD}})^2 \times \sigma_{\text{ADC}}^2 \quad (4.2)$$

Using Eq. 4.2 and C_{FD} = 4.5 photons / ADC, the average fluctuations on the photon count can be calculated.

$$\sigma_{\text{ph}} = 23 \text{ photons} / 100 \text{ ns}$$

where σ_{ph} is the fluctuations on the photon count per 100 ns.

Finding the number of photons at the diaphragm takes more steps since the fluctuations are affected by more than the Poisson statistics of the photon number. The first step involves converting the ADC variance to photo-electron numbers. This step is achieved through using the combination of Eq. 4.3 and Eq. 4.4.

$$n_{\text{pe}} = \frac{\sigma_{\text{pe}}^2}{(1 + V_G)} \quad (4.3)$$

$$\sigma_{\text{pe}}^2 = [\sigma_{\text{ADC}}^2]^{\text{sky}} / A_G^2 \quad (4.4)$$

where σ_{pe} is the standard deviation of the photo-electron count, n_{pe} is the photon-electron count, V_G is the PMT gain variance factor ?? and A_G is the absolute gain (ADC/photo-electron) of the PMT. A_G is equal to:

$$A_G = \eta \times G \times E \quad (4.5)$$

where

η is the PMT collection efficiency at the first dynode.

G is the PMT gain.

E is the electronic conversion constant (ADC per anode electron).

An equivalent quantity can be used to calculate A_G and is:

$$A_G = \frac{1}{C_{\text{FD}} \times f \times Q} \quad (4.6)$$

where

C_{FD}	4.5 photons/ADC
Q	0.29
f	0.494

Table 4.2: Typical values for the constants used to calculate A_G which is the absolute gain (ADC/photo-electron). C_{FD} is the FD pixel calibration constant, Q is the Quantum efficiency of the PMT turning photons into photo-electrons and f is the photon collection efficiency of the telescope optics.

Photon Collection Efficiency	f	$F \times L \times T \times R \times M$
Filter Transmission	F	0.83
Corrector Ring lens Transmission	L	0.90
Mirror Reflectivity	R	0.90
Camera Shadow Factor	T	0.79
Mercedes Collection Efficiency	M	0.93

Table 4.3: Breakdown of all the components that go into the FD photon collection efficiency. Photon Collection Efficiency = Filter Transmission \times Corrector Ring lens Transmission \times Mirror Reflectivity \times Camera Shadow Factor \times Mercedes Collection Efficiency ($f = F \times L \times T \times R \times M$)

Q is the Quantum efficiency of the PMT turning photons into photo-electrons.

f is the photon collection efficiency of the telescope optics. The components that make up the telescope optics are shown in Table. 4.3.

Therefore A_G can be calculated from Eq. 4.5 using the values from Table 4.2. Typical measured values for C_{FD} , Q and f shown in Table 4.2. The PMTs used as camera pixels in the FDs are HAMAMATSU XP3062 and are operated at a gain of $\sim 5 \times 10^4$ electrons/photo-electron.

The next step is to convert the photo-electron numbers to number of photons at the diaphragm. This step is achieved through using Eq. 4.7.

$$n_{ph} = \frac{n_{pe}}{Q \times f} \quad (4.7)$$

From all of the equations stated above the following table shows the expected photon count at the aperture per 100 ns from the measured variance ($ADC^2 / 100$ ns).

Moon Illumination Fraction (%)	Variance ($ADC^2/100$ ns)	Photons / 100 ns @ Pixel	Photons / 100 ns @ diaphragm
0	25	23	46
50	250	227	459
100	2500	2267	4588

Table 4.4

4.2.2 Night Sky Background and the Moon

The Night Sky Background for Auger typically refers to airglow, zodiacal light, scattered starlight and any man-made light. Moonlight is a separate source of background light as an FD shift is typically operated when the moon is below the horizon. Table 4.5 shows the expected change in average background light observed by the FD telescopes for no moon, 1st/3rd quarter moon and full moon / twilight. 1st/3rd quarter moon is either one quarter or three quarters through the moon orbital cycle and is when 50% of the observable moon from earth is illuminated. From the table it can be seen that going from no moon to quarter moon to full moon jumps by a factor of ten in the observed ADC variance at each step. The large change in moon brightness for the different phases is due to the fact that the light is subject to spectral reflection not diffusion reflection.

Condition	Illumination Fraction	σ^2 [ADC ² /100 ns]	I _a [μ A]
no moon	0%	25	0.5
quarter moon	50%	250	5
full moon/twilight	100%	2500	50

Table 4.5: Expected average observed variance in ADC², and the anode current in μ A by the PMTs in the FD telescopes under different NSB conditions. No Moon is the typical conditions for operation of the FD shift.

Figure 4.2a plots the integral fraction of the night time within a year with the moon less than a particular illuminated fraction. Only times between astronomical dusk and dawn has been included. The solid line shows the percent of the year is astronomical twilight (sun at least 18°below the horizon). The dotted lines represent relaxed definition of twilight with the sun being at 15°, 12° and 9° below the horizon. The line curves up slowly due to that throughout the moon orbital cycle at times it will be above the horizon during daylight hours. After first quarter and before 3rd quarter the moon will be visible for longer at night time. Observing under indirect moonlight could increase the duty cycle by 5% to 10% across a year.

Figure 4.2b shows the relative change in brightness of the moon depending on the observed illuminated fraction. The red line is a fitted exponential to U-Band data taken at the La Palma observatory. The graph shows the large difference in moon brightness as the illuminated fraction increases which was also described in Table 4.5. The slope is comparable to actual data taken from the background files measured by the FD telescopes. The measured ADC variance plotted against fraction of illuminated moon is shown in Figure 4.3.

4.2.3 Toy Model of the effect of increased NSB on aperture

A simple measure of how well a detector will operate is to calculate the signal-to-noise (S/N) ratio. The steps that I followed were outlined in ???. The signal-to-noise ratio is denoted by:

$$\text{Signal to Noise} = \frac{S}{N} \quad (4.8)$$

where S is the signal and N is the noise amplitude. The first step is to calculate the noise (N) expected from a background signal (B). First the background photo-electron count rate (B) seen from the night sky is calculated via:

$$B \propto \epsilon A b \Delta \Omega \Delta t$$

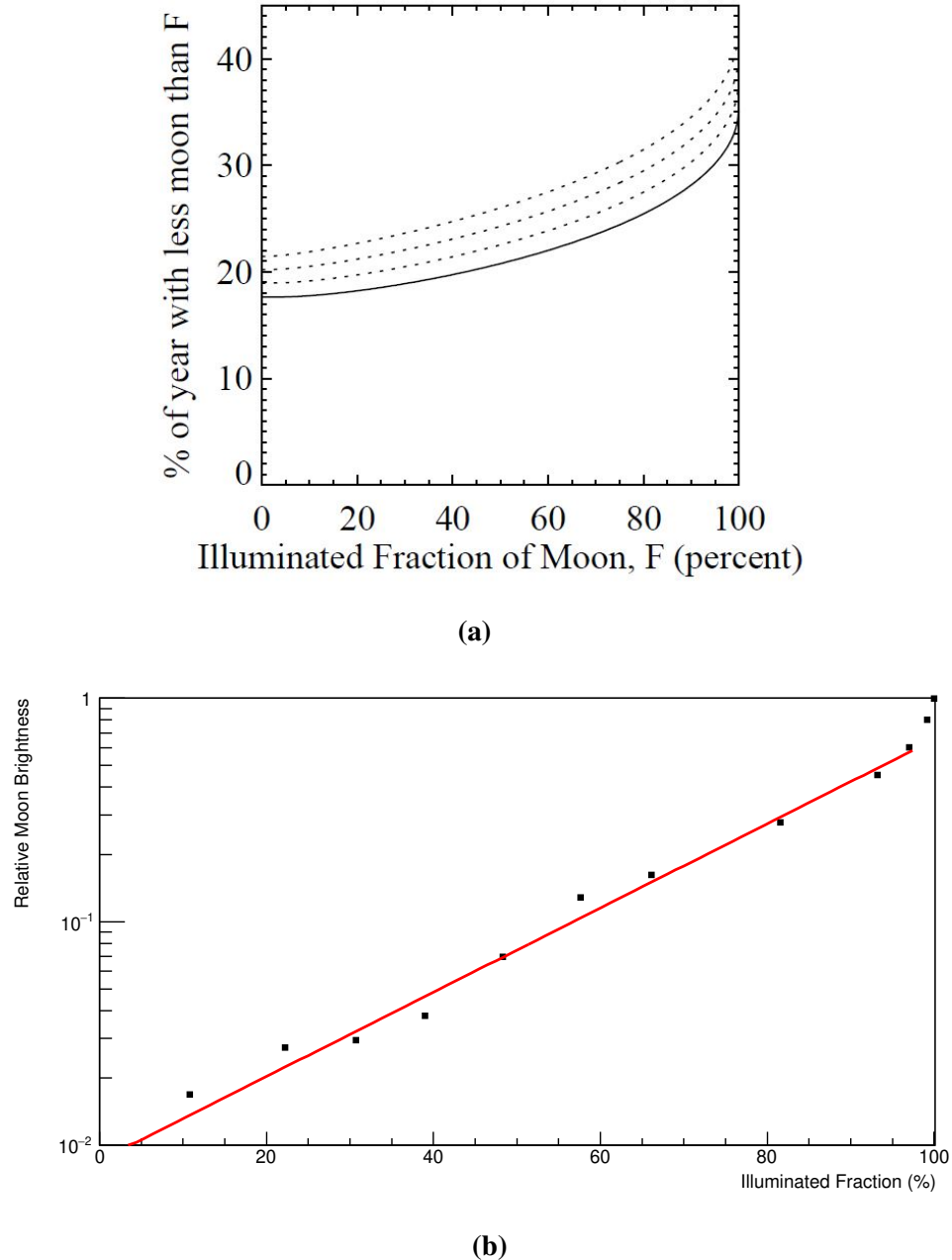


Figure 4.2: (a) Integral fraction of nights across the year with the moon with different illuminated fractions. Only times between dusk and dawn have been included. The solid line is the astronomical twilight (sun at least 18° below horizon). The dotted lines represent relaxed definitions of twilight with the sun being at 15° , 12° and 9° below the horizon. (b) Relative brightness of the moon in the night sky compared with a full moon as a function of illuminated fraction. Images taken from [ref\(GAP1996-034\)](#).

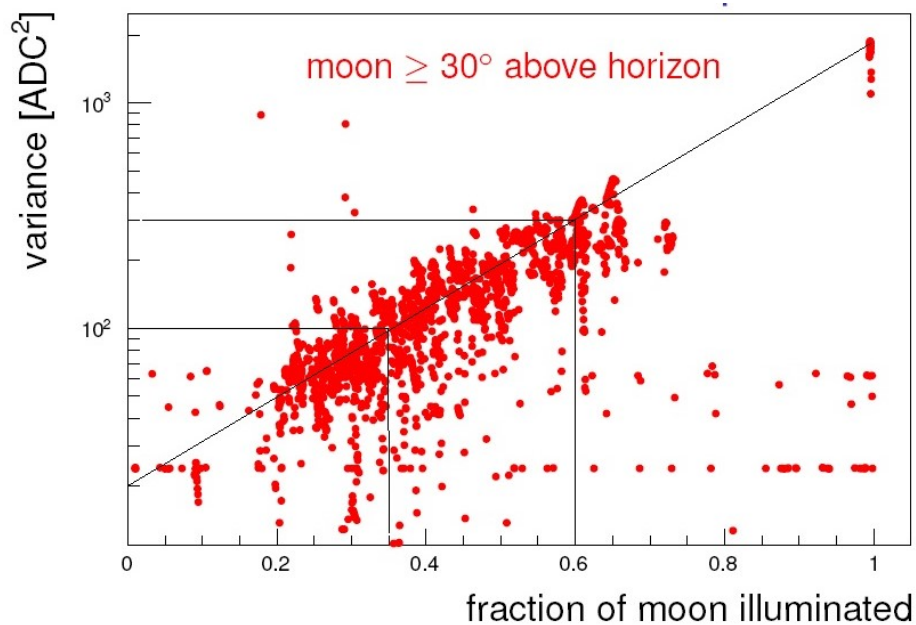


Figure 4.3: Measured NSB variance from the Fluorescence Detectors at Standard PMT HV setting with different moon illuminated fractions. The moon was 30° above horizon or greater. Image taken from [ref\(Radimir\)](#).

where ϵ is the optical efficiency of the telescope, A is the mirror area, b is the background light flux and $\Delta\Omega$ is the solid angle of the sky viewed by a single PMT. ϵ is $f \times Q$ where F is the optics factor shown in Table 4.3 and Q is the quantum efficiency of the photon sensitive device (i.e. photomultiplier tube). Next the fluctuations on the noise can be found which is the square root of the background signal:

$$N = \sqrt{B} \propto \sqrt{\epsilon A b \Delta\Omega \Delta t} \quad (4.9)$$

Next step is to calculate the signal (S) from an extensive air shower that a detector would observe.

$$S \propto \frac{\epsilon A n_+ n_\gamma c \Delta t}{4\pi R^2} e^{-R/\lambda_R} \quad (4.10)$$

where n_+ is the number of charge particles in the shower viewed by the photon sensitive device, n_γ is the photon yield per charged particle for atmospheric scintillation, R is the distance to the shower segment, $c\Delta t$ is the length of the shower segment, and λ_R is the Rayleigh attenuation length of light in the atmosphere. Substituting Eq. 4.9 and Eq. 4.10 into Eq. 4.8 and removing the proportionality gives:

$$\frac{S}{N} = n_+ n_\gamma c \frac{(1 + \cos\theta)}{4\pi(R \times \sin\theta)^2} \sqrt{\frac{\epsilon A \Delta t}{b \Delta\Omega}} e^{-R/\lambda_R} \quad (4.11)$$

where θ is the viewing angle of the EAS.

From here I use values specific to the Fluorescence Detectors to calculate the S/N ratio expected. The majority of the values used are shown in Table 4.6. The viewing angle is 90° as the shower is viewed at 15° with the center of the FD camera at 15° elevation. As the perpendicular segment of the shower is being observed therefore $R = R_P$ where R_P is the closest distance that the shower axis is to the FD. The Rayleigh attenuation length (λ_R) is calculated via:

$$\lambda_R = 2974 \left(\frac{\lambda}{400 \text{ nm}} \right)^4 \text{ g/cm}^2 \quad (4.12)$$

where λ is the chosen wavelength in nanometres. Currently R_P is in units of length where the Rayleigh attenuation length calculated in Eq. 4.12 in units of mass per length squared. A diagram of how R_P and the shower axis is related to the detector is shown in Fig. 4.4. To find the distance R_P in terms of grammage the term ΔX_P is defined. Substituting this term into Eq. 4.11 becomes:

$$\frac{S}{N} = n_+ n_\gamma c \frac{(1 + \cos\theta)}{4\pi(R \times \sin\theta)^2} \sqrt{\frac{\epsilon A \Delta t}{b \Delta\Omega}} e^{-\Delta X_P/\lambda_R} \quad (4.13)$$

The ΔX_P can be calculated from the distance R_P via

$$\Delta X_P = \Delta X_{\text{vertical}} / \cos 75^\circ \quad (4.14)$$

$$\Delta X_{\text{vertical}} = 860 - 860 \exp(-h/7500) \quad (4.15)$$

$$h = R_P \times \sin 15^\circ \quad (4.16)$$

where h is the vertical distance of the shower segment in meters and $\Delta X_{\text{vertical}}$ is the vertical path in g/cm^2 , the shower axis is at 15° elevation and 75° is the zenith angle. To find the grammage along the path to R_P the vertical distance h is substituted and then the path ΔX_P can be found. The relationship between ΔX_P and R_P is shown in Fig. 4.5 for a detector viewing the sky at 15° elevation. The relationship is curved due to the amount of atmospheric

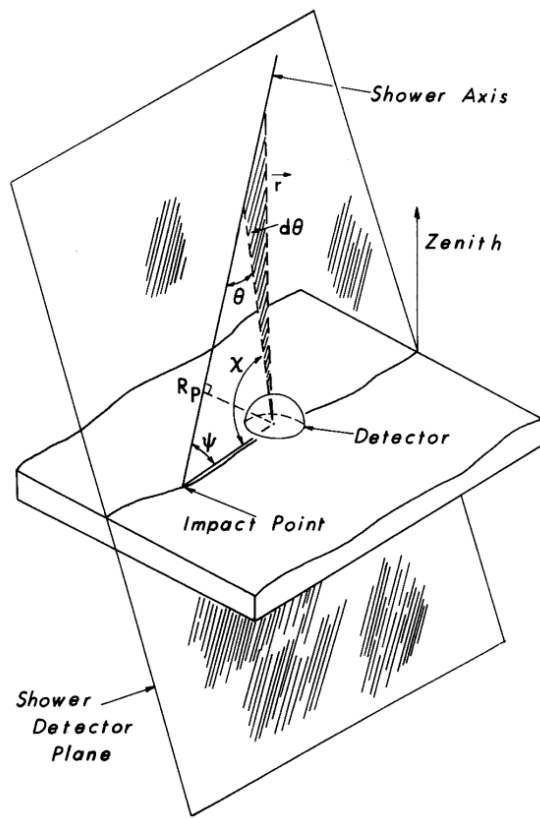


Figure 4.4: Diagram showing the parameters used. Also show how they relate to the plane of the shower axis and to the position of the detector.

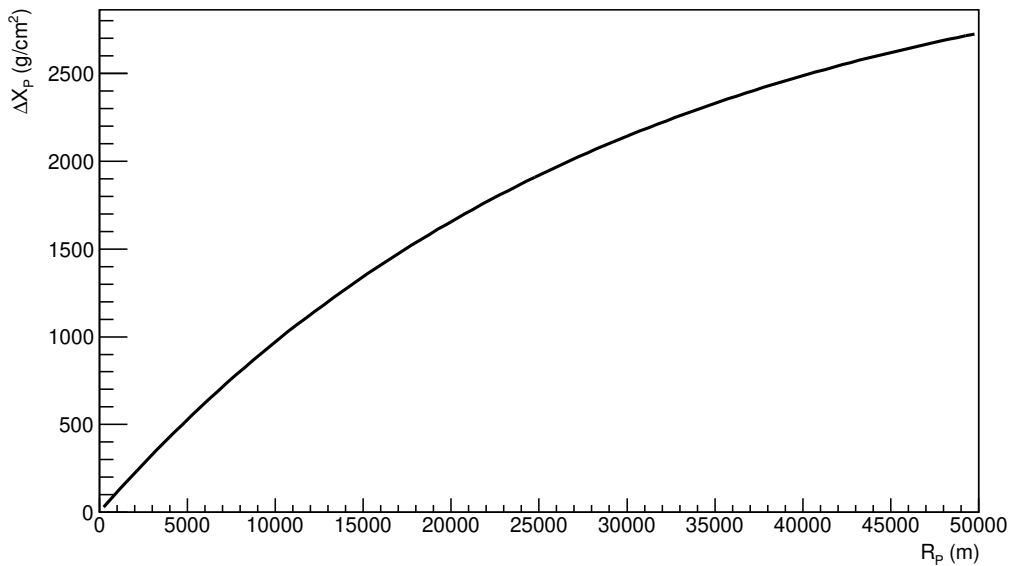


Figure 4.5: How the relationship between the distance to the shower axis and grammage along the path. In this case the distance to the shower axis is denoted R_P and the grammage is denoted ΔX_P . R_P is the closest distance that the shower axis is to the detector. The angle of the shower is 15°

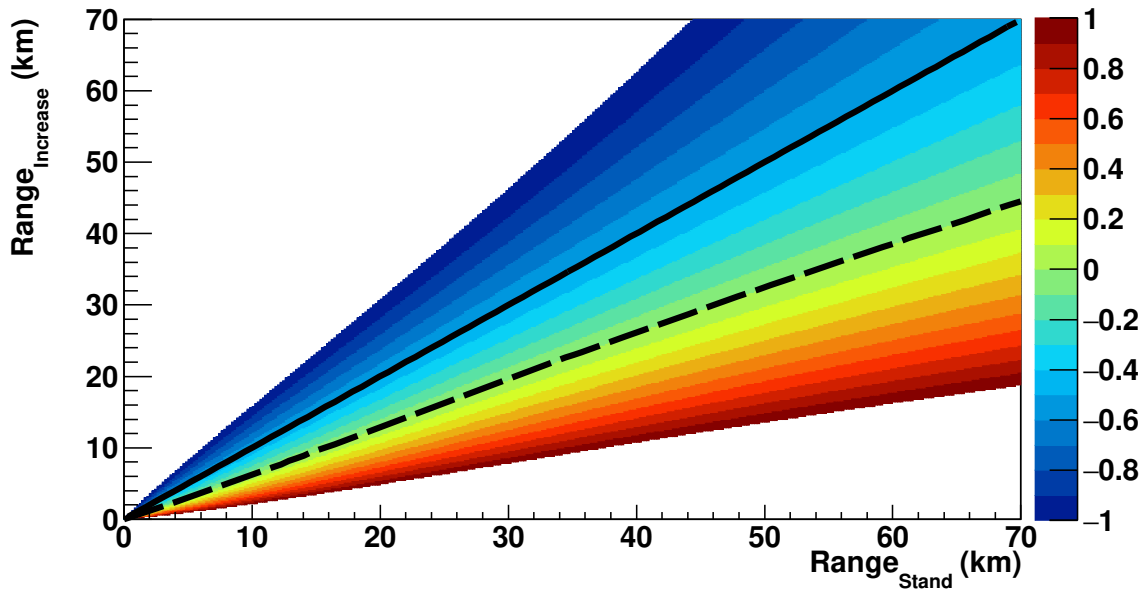


Figure 4.6: The image of the calculated Signal-to-Noise ratio the NSB at the Standard value and Increased NSB by a factor of 10 as a function of distance for an individual detector. The dashed black line denotes the distances where the Signal-to-Noise ratio is the same for the different NSB levels. The solid black line denotes where the distances are equal.

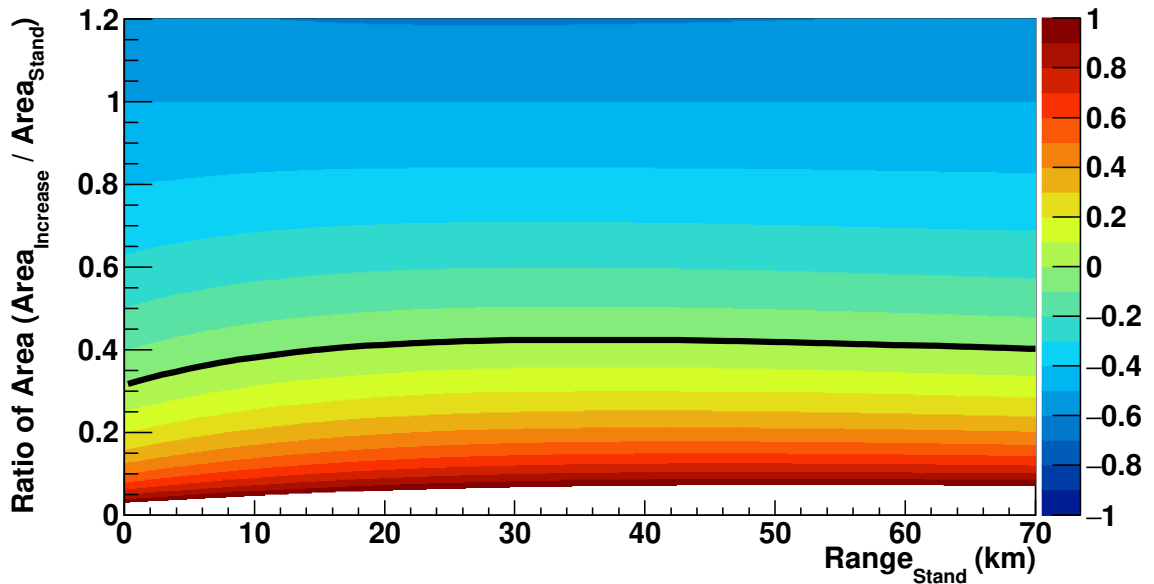


Figure 4.7: The image shows how the ratio of the detector viewing area changes with increasing the NSB by a factor of 10 as a function of distance from the detector. The solid black line denotes where the Signal-to-Noise ratio is the same.

optical efficiency	ϵ	0.135
mirror area	A	3.8 m ²
Standard background light flux	b_1	5e5 photons / m ² / sr / μ s
Increased background light flux	b_2	5e6 photons / m ² / sr / μ s
solid angle of a single PMT	$\Delta\Omega$	5.38e-4 sr
viewing angle	θ	90°
speed of light	c	3e2 m / μ s
number of charged particles	n_+	Particle Energy / 1e9
Fluorescence yield	n_γ	4 photons / m / charged particle
Chosen wavelength	λ	350 nm
Rayleigh attenuation length	λ_R	1743 g / cm ²

Table 4.6: Values specific to the Fluorescence Detectors.

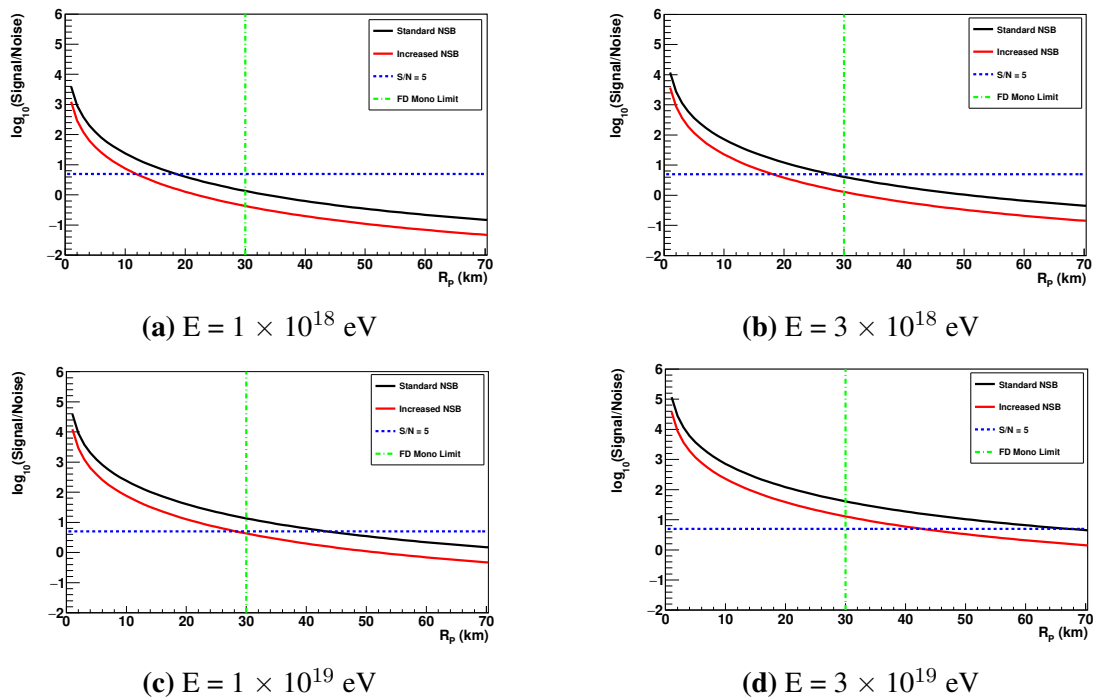


Figure 4.8: Using the FD values in Table 4.6 and Eq. 4.11 to calculate the Signal-to-Noise ratio from specific values for the FD, NSB and conversion's from shower energy to photons to photo-electrons. The black solid line represents the S/N ratio at typical NSB flux seen at Auger, the red solid line represents the S/N ratio if the NSB flux was increased by a factor of 10, the blue dash line represents the single pixel trigger threshold, and the green dashed line represents the viewing limit of a single FD telescope before an event is closer to another FD telescope.

molecules dropping off rapidly as the observed event moves further away both horizontally and vertically.

The result of calculating the theoretical of the Signal-to-Noise Ratio is shown in Fig. 4.6 and Fig. 4.7. The scale for both is shown in Log_{10} scale so the colour range above and below one is equidistant. $\text{Range}_{\text{Stand}}$ is the expected S/N ratio for the range with standard observed NSB and $\text{Range}_{\text{Increase}}$ is the expected S/N for the range with observed NSB increased by a factor of 10. Fig. 4.6 shows the relationship between the S/N ratio for $\text{Range}_{\text{Stand}}$ and $\text{Range}_{\text{Increase}}$. The solid black line represents the S/N ratio for when the distances are equal. The difference between ratio at the solid black line is $1/\sqrt{10}$. The dashed black line represents where the S/N ratio are equal. It can be seen that $\text{Range}_{\text{Increase}}$ is smaller than $\text{Range}_{\text{Stand}}$ which is expected when the NSB has been increased for $\text{Range}_{\text{Increase}}$. Fig. 4.7 shows how much the observing area changes from $\text{Range}_{\text{Stand}}$ to $\text{Range}_{\text{Increase}}$. The solid black line denotes where the S/N ratio is the same.

Table 4.6 and Eq. 4.11 were used to produce Fig. 4.8 which shows how the S/N ratio changes versus distance for cosmic-rays of four different primary energies. The black solid line represents the S/N ratio at typical NSB flux seen at Auger, the red solid line represents the S/N ratio if the NSB flux was increased by a factor of 10, the blue dash line represents the single pixel trigger threshold, and the green dashed line represents the viewing limit of a single FD telescope before an event is closer to another FD telescope. The figures show that for showers with energies above 3×10^{19} eV that increasing the NSB by a factor of 10 would expect no impact on the FD collecting area. For showers energies of 1×10^{19} eV and below it would be expected that the FD collecting area would be reduced as the NSB is increased.

4.3 Increasing NSB in Real Data to evaluate Reconstruction Efficiency

- Aim

To test the effect of increasing the NSB levels in real data to evaluate the effects on reconstruction efficiency. The reconstruction tool that Auger employs is a internally developed software package called OffLine. OffLine takes selected shower events and goes through the process of finding signals within pixles, and calculating energy and arrival direction. The real data set was the showers used for analysis for ICRC 2015.

4.3.1 Method

- Take shower set

- add artifical noise to the raw pixel traces
- Use OffLine to reconstruct shower with the increased noise
- Compare Selection Efficiency, Energy resolution and bias, and Xmax resolution and bias.

To evaluate the effects of increased NSB levels on the reconstruction efficiency the data set used for ICRC 2015 had artifical noise add to the raw pixel traces. Once the desired NSB level has been added OffLine is used to reconstruct the shower events again. The results from the standard NSB levels and the increased NSB levels can be compare. I mainly focused on the comparison between Efficiency, Energy resolution and bias, and Xmax resolution and bias. This method allows for any NSB flux levels to be investigated.

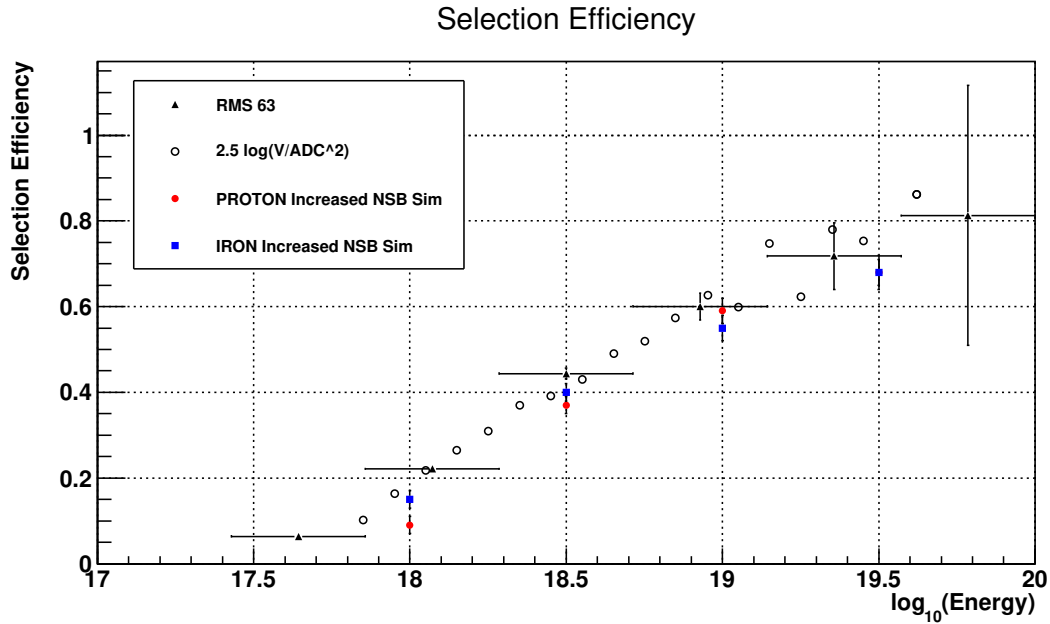


Figure 4.9: The selection efficiency with my repetition against the data points from M. Unger. The method and data sets are similar with the NSB used differing slightly.

The Efficiency is comparison of events that are successfully reconstructed at standard NSB compared to the number of events that are successfully reconstructed at the increased NSB levels. The Efficiency was calculated with the equation used:

$$\text{Efficiency}_{\text{Data}} = N'_{\text{SelectData}} / N^0_{\text{SelectData}} \quad (4.17)$$

where $N^0_{\text{SelectData}}$ is the number of selected events at the standard NSB level and $N'_{\text{SelectData}}$ is the number of selected events at the increased NSB level.

After the Efficiency was calculated the bias and resolution for Xmax and energy was determined. For real data, the bias is the relative change in the mean of the distributions at increased NSB to the mean of the distributions at standard NSB, both after reconstruction and selection cuts. The bias calculations for real data become:

$$\Delta E_{\text{Data}} = \frac{E_{\text{IncreasedNSB}} - E_{\text{StandardNSB}}}{E_{\text{StandardNSB}}} \quad (4.18)$$

$$\Delta X_{\text{maxData}} = X_{\text{maxIncreasedNSB}} - X_{\text{maxStandardNSB}} \quad (4.19)$$

The energy and Xmax resolution is calculated via:

$$\sigma_{\text{resData}} = \left(\frac{1}{N} \sum \sigma_i^2 \right)^{1/2} \quad (4.20)$$

where σ_i^2 is the reconstructed uncertainty on the individual shower events.

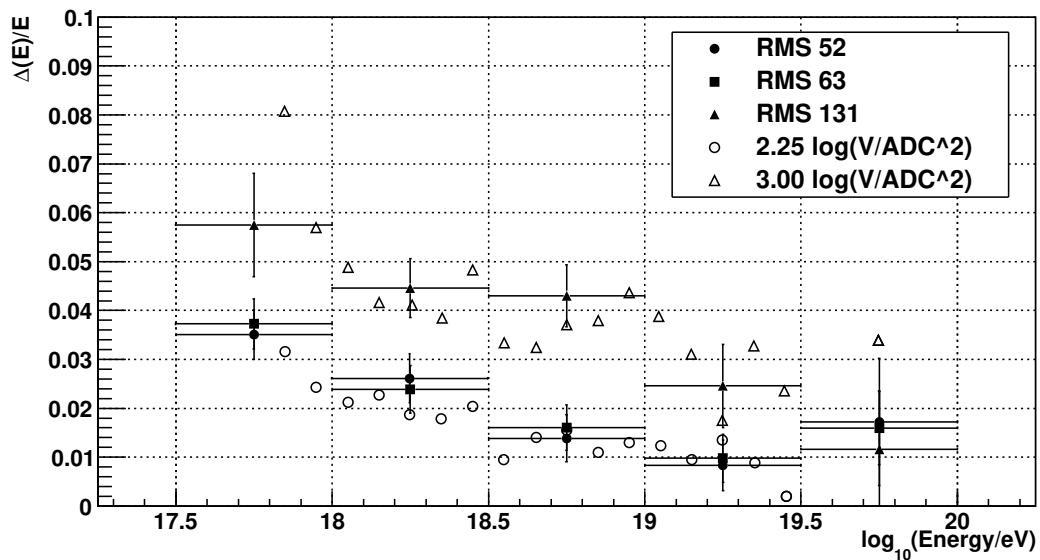


Figure 4.10: Energy Bias from increasing NSB in Real Data.

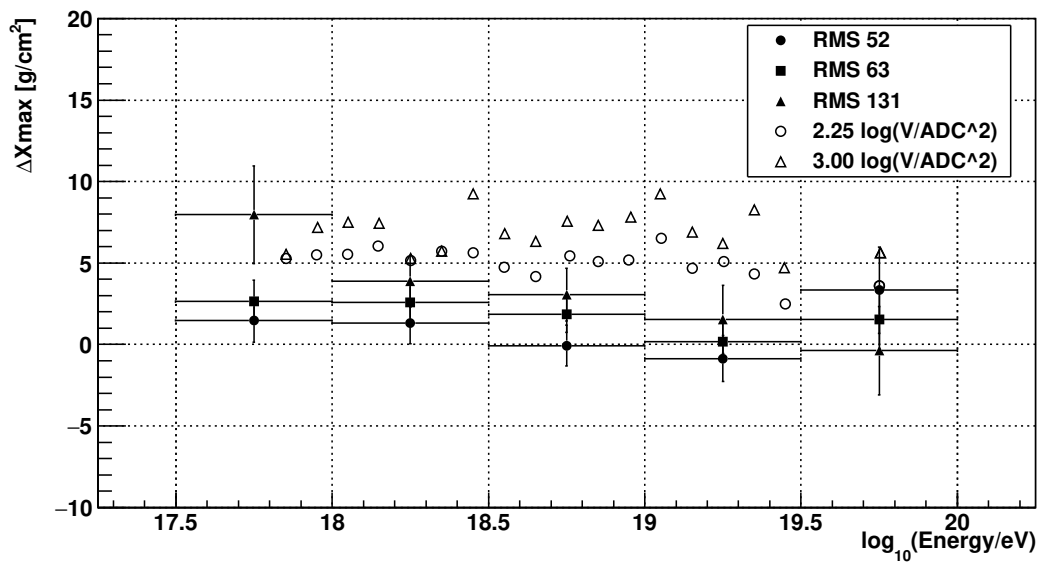


Figure 4.11: Xmax Bias from increasing NSB in Real Data.

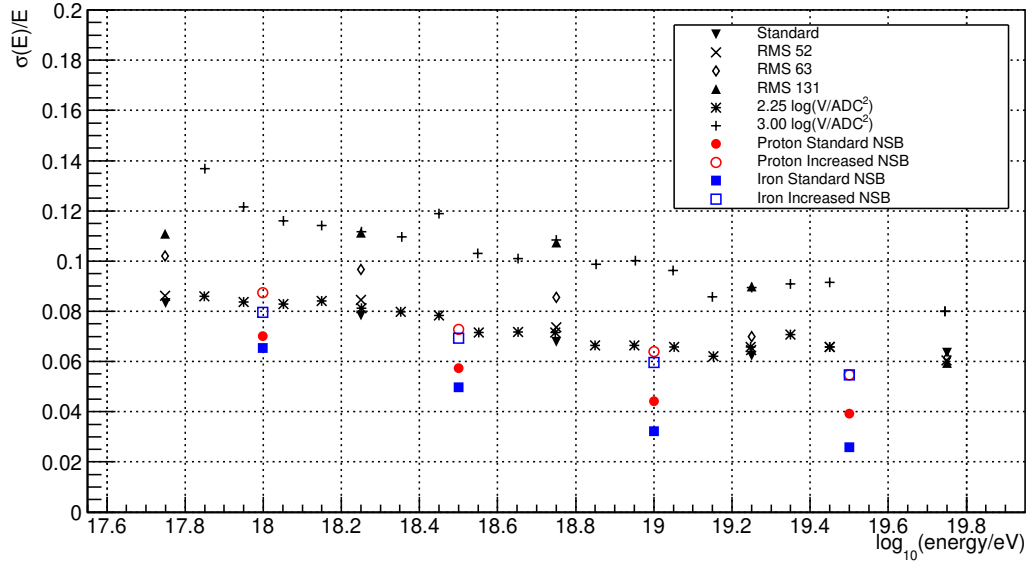


Figure 4.12: Energy Resolution using both Smearing Method data and simulated showers.

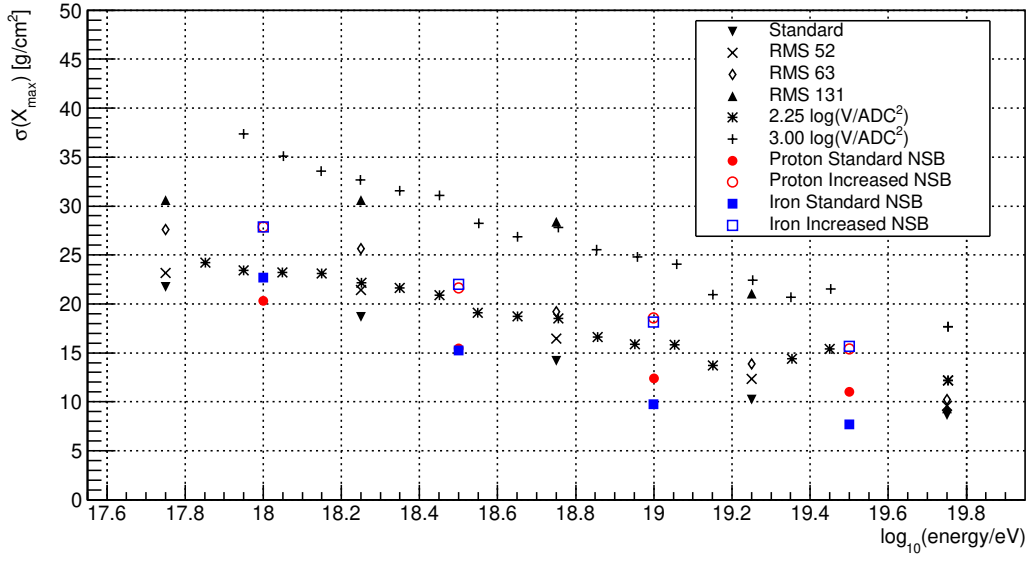


Figure 4.13: Xmax Resolution using both Smearing Method data and simulated showers.

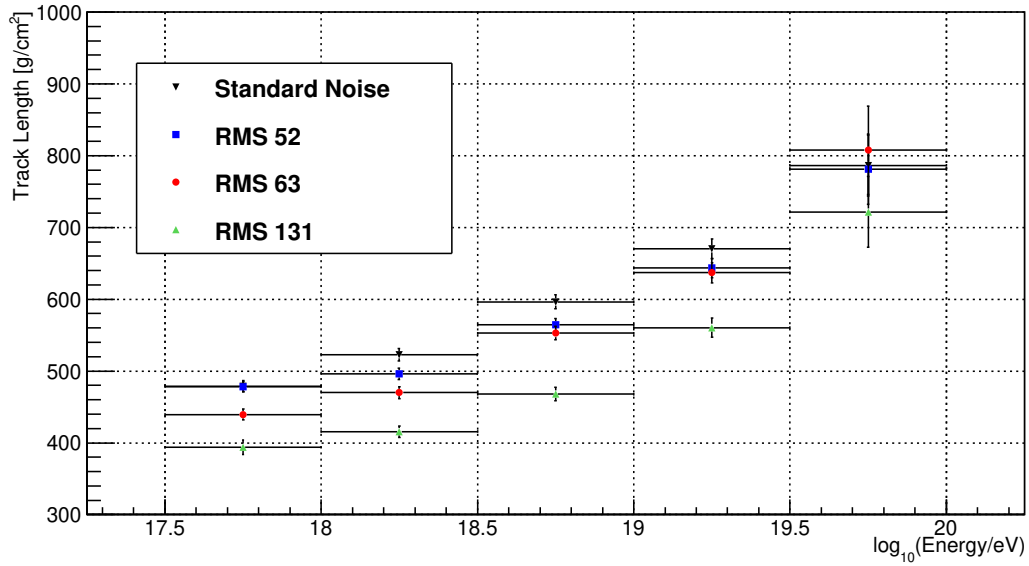


Figure 4.14: Track length calculated from events with standard NSB and those with increased NSB fluxes.

4.3.2 Results

4.3.3 Discussion

4.4 Increasing NSB in Simulations to evaluate Trigger/Reconstruction Efficiency

4.4.1 Method

The Efficiency was calculated with the equation used:

$$\text{Efficiency} = N'_{\text{Select}} / N^0_{\text{Select}} \quad (4.21)$$

where N^0_{Select} is the number of selected events at the standard NSB level and N'_{Select} is the number of selected events at the increased NSB level.

For simulated data the bias is the relative change in the mean of the distributions after the full simulation by EAS events going through an atmosphere with a specified NSB photon field, the FD telescopes optics, trigger, reconstruction and selection cuts compared with Monte-Carlo truth.

$$\Delta E_{\text{Sim}} = \frac{E_{\text{recon}} - E_{\text{true}}}{E_{\text{true}}} \quad (4.22)$$

$$\Delta X_{\text{maxSim}} = X_{\text{maxrecon}} - X_{\text{maxtrue}} \quad (4.23)$$

The energy and Xmax resolution is calculated via:

$$\sigma_{\text{resSim}} = \left(\frac{1}{N} \sum \frac{1}{\sigma_i^2} \right)^{1/2} \quad (4.24)$$

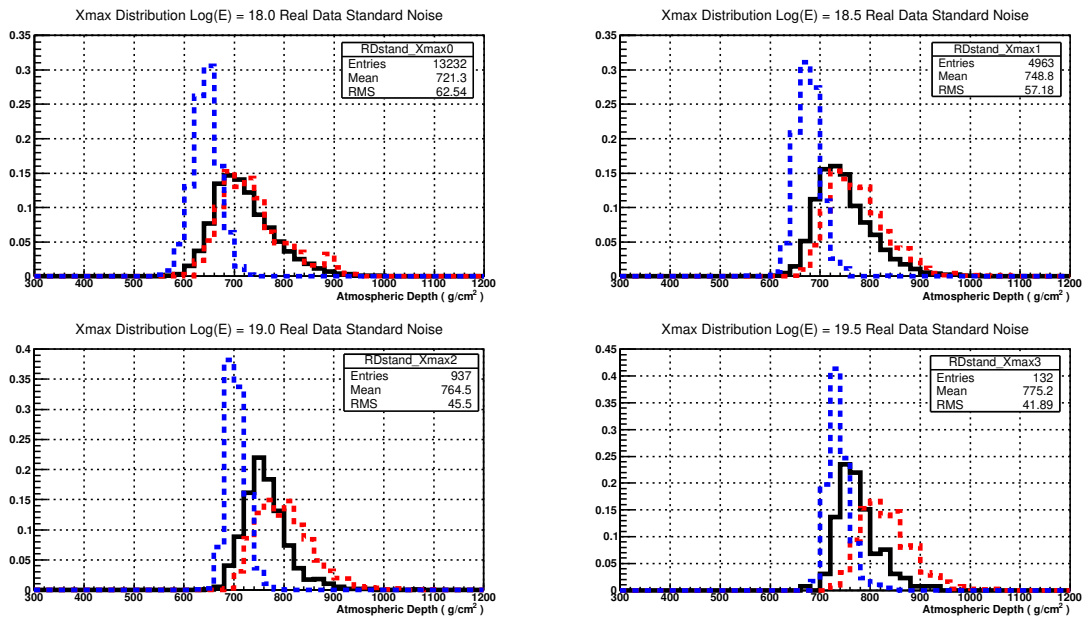


Figure 4.15: Distribution of Xmax with Real Data and simulation of proton and iron showers.

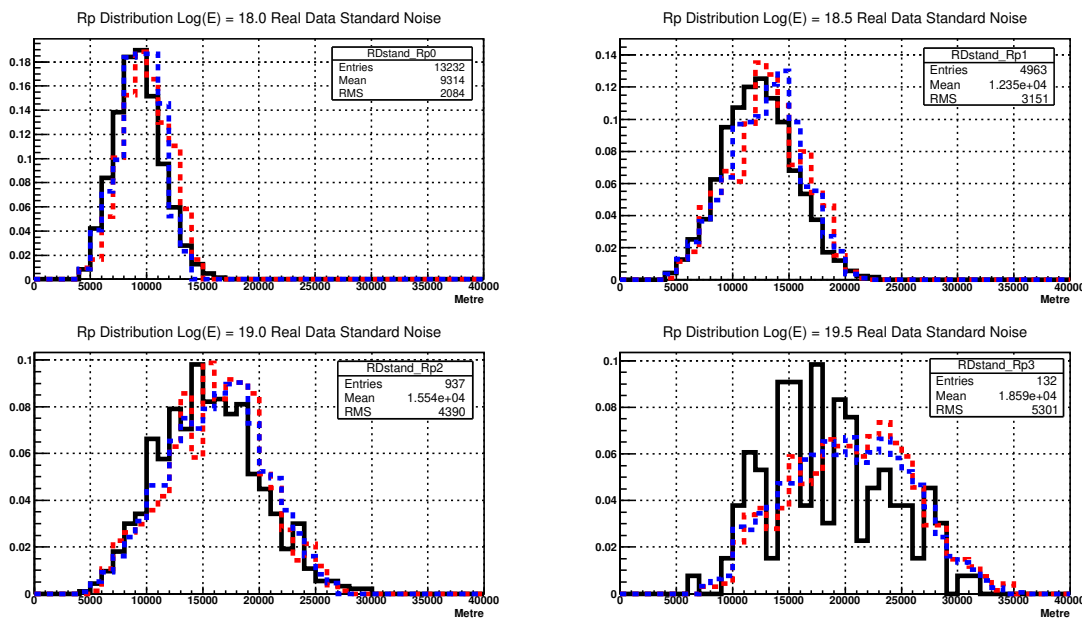


Figure 4.16: Distribution of Rp with Real Data and simulation of proton and iron showers.

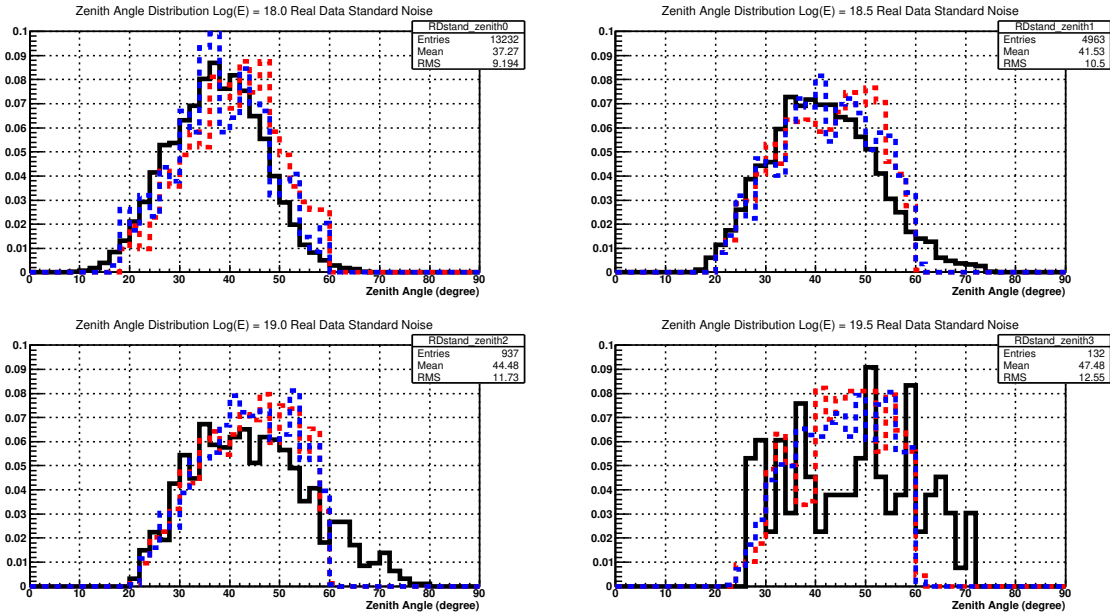


Figure 4.17: Distribution of Zenith angle with Real Data and simulation of proton and iron showers.

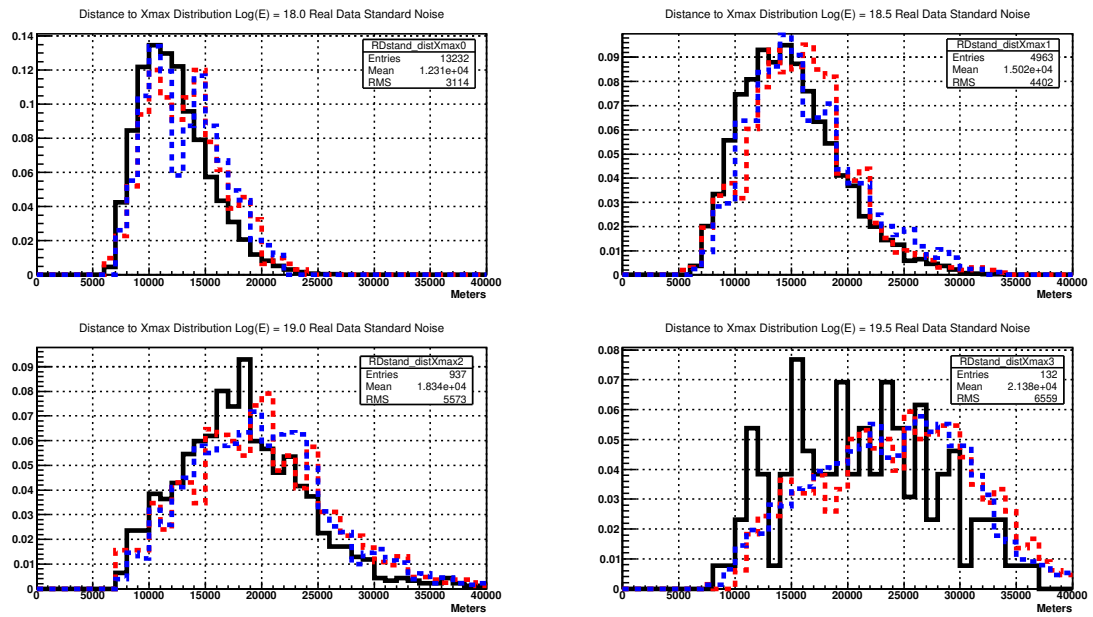


Figure 4.18: Distribution of Distance to Xmax with Real Data and simulation of proton and iron showers.

4.4.2 Comparison of Simulated Data to Real Data**4.4.3 Results****4.4.4 Discussion****4.5 Conclusion/Summary**

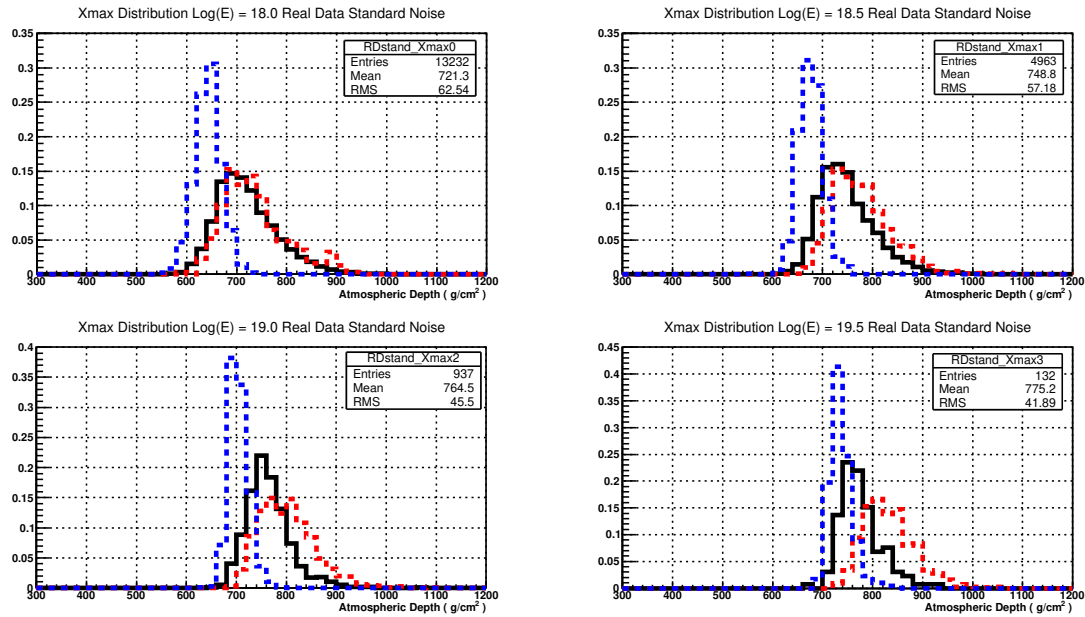


Figure 4.19: Distribution of X_{max} with Real Data and simulation of proton and iron showers.

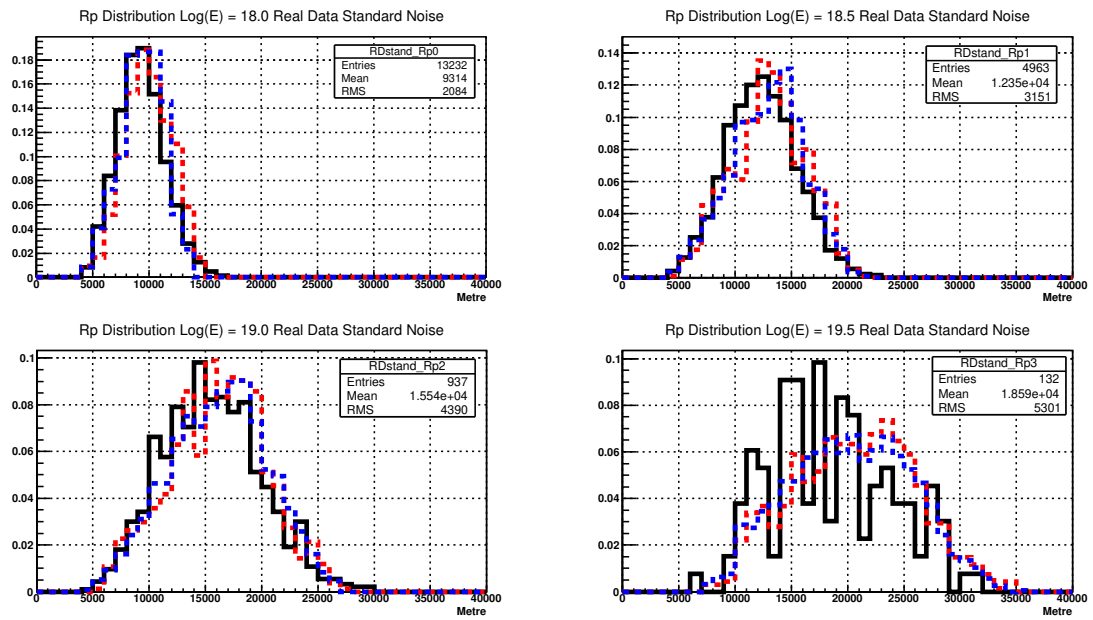


Figure 4.20: Distribution of R_p with Real Data and simulation of proton and iron showers.

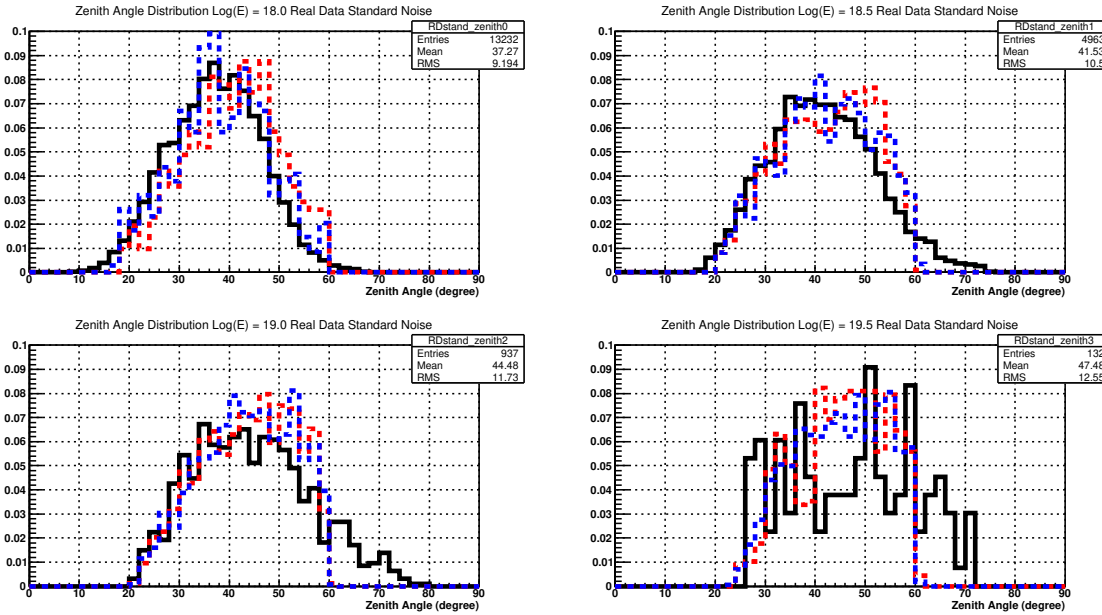


Figure 4.21: Distribution of Zenith angle with Real Data and simulation of proton and iron showers.

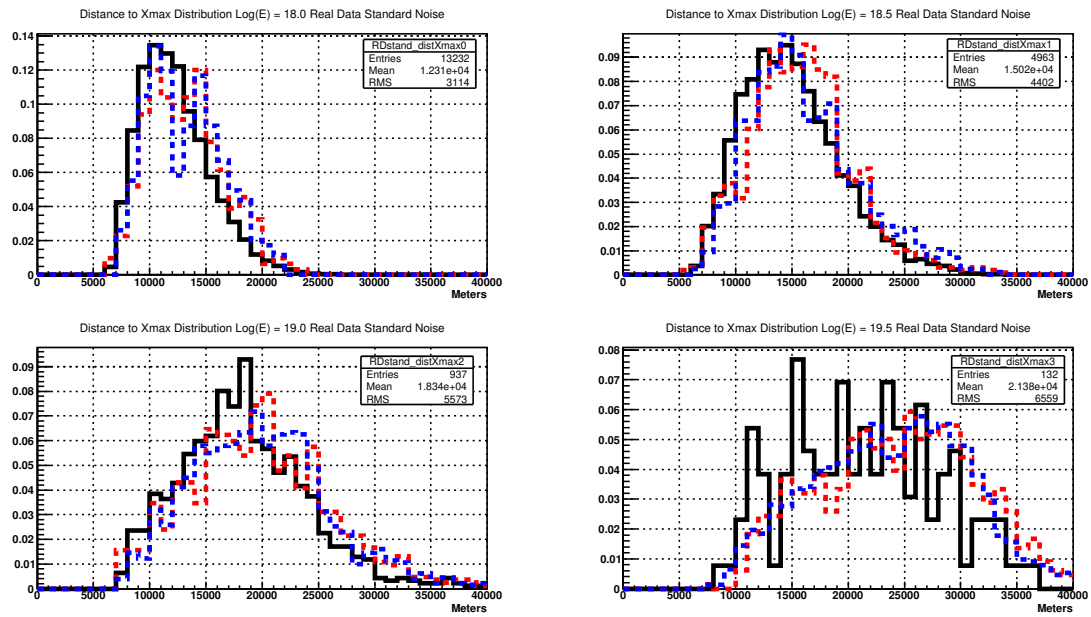


Figure 4.22: Distribution of Distance to Xmax with Real Data and simulation of proton and iron showers.

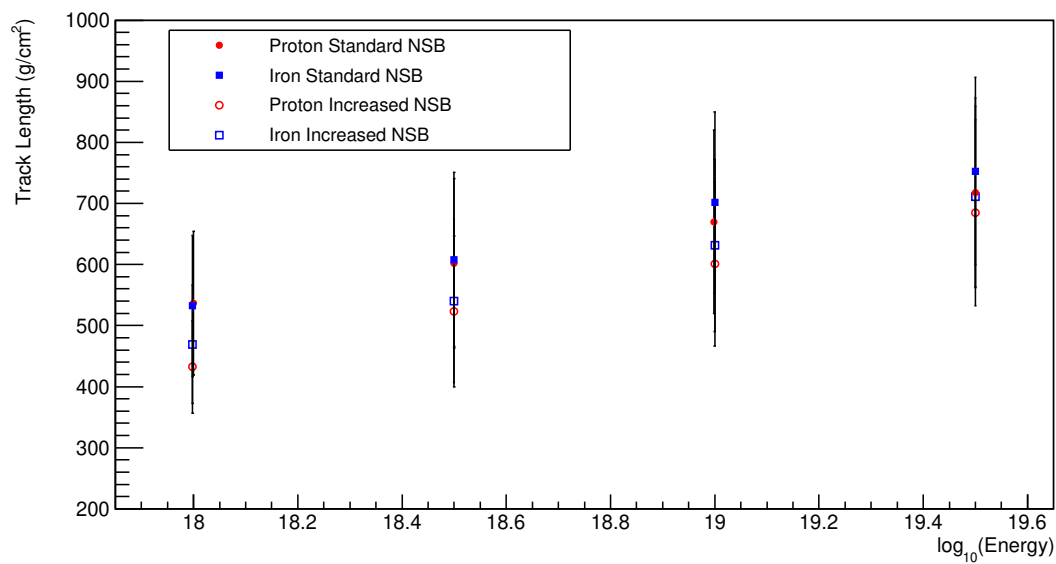


Figure 4.23: Track length using simulation of proton and iron CONEX showers.

Chapter 5

Quantifying Characteristics of the Fluorescence Detector Photomultiplier Tube

5.1 Motivation

The Pierre Auger Observatory has been operational since 2004 and the Collaboration is in the process of rolling out upgrades to improve the experiment. The current upgrade has been name AugerPrime ([ref](#)) and is a large project to improve both the Surface Detectors (SD) and the Fluorescence Detectors (FD). The FD portion of AugerPrime involves extending the duty cycle to observe Extensive Air Shower (EAS) events while the moon is above the horizon. The main purpose for extending the FD duty cycle to include observation times while the moon is visible is to increase the statistics per year for EAS events at the highest energy ($> 10^{19.5}$ eV).

In this chapter I will explore the linearity and effects of temperature on the gain for a HAMAMATSU XP3062 Photomultiplier Tube (PMT) at the Hight Voltage setting of 600V. I will use the measurements obtained at 900V as the baseline of expected performance. The Fluorescence Detectors (FDs) at Auger use Photomultiplier Tube (PMT) as camera pixels within the telescopes to view the Extensive Air Showers. The PMTs are operated at a gain of 5×10^4 electrons per photo-electron. This gain relates to a High Voltage about 900V. The investigation into running the Fluorescence Detectors under moonlight has lead to the proposal of running the PMTs under decreased gain. The PMT gain is expected to decreased by a factor of 10 to compensate. Therefore the PMT High Voltage would be dropped to about 600V to have a gain of 5×10^3 electrons per photo-electron.

5.2 Background

- HAMAMATSU XP3062 Photomultiplier Tube (PMT) - 8 dynodes - sensitive within the wavelength range - is behind a UV filter - Voltage across each dynode layout - data sheet of expected behaviour

5.3 PMT Linearity

One of the major characteristics of interest when operating a Photomultiplier Tube (PMT) is its linearity. A PMT linearity is where if a light intensity is doubled the PMT response doubles as well. It is important to quantify this region to be confident that if the light intensity changes the PMT response follows.

I look at two methods to measure the PMT linearity - using Neutral Density filters and the Two LED method.

5.3.1 Neutral Density Filters

The method of using Neutral Density filters involves employing filters to reduce the light intensity reaching the PMT cathode by a known amount. The filters were used singularly and in combination to get different Optical Transmission. The filters are label with optical density which is different to optical depth. To convert optical density to transmission:

$$\text{Optical Depth} = -\log_{10} \left(\frac{\text{Transmission}}{100} \right) \quad (5.1)$$

To get different transmission values, the filters can be stack and the optical depth values just add together (IE. if using two filters one with ND 0.4 and ND 0.1 the total ND will be 0.5).

I repeated a study done by Privitera et. al. (1990) [ref.](#) on Auger PMTs. I wanted to use the result done at an High Voltage value of 900V as my baseline then continue the study to observe the result at an High Voltage value of 600V.

Some of the disadvantages of using Neutral Density filters it that you are restricted to fixed units of transmission depending on which filters you have access too. Also you are relying on the fact that the optical density do not deteriorate over time and is not effected by handing and storage. There is also some uncertainty on the optical density value quote.

5.3.2 Two LED Method

Another method investigate was the two LED method. This method was used in the original measurement of the SD PMTs [ref.](#). To measure the linearity, two LEDs are pointed at the PMT and with one set of observations taken with the LEDs on separately then one set taken with the LEDs on at the same time. A graphical representation is shown in Fig. 5.3 of the set-up used to measure the PMT linearity at both 900V and 600V. Two pulse generators are used to drive the LEDs separately and to allow the two pulses to overlap when needed to measure the PMT response to the LEDs on at the same time. To find the linearity a ratio is plotted against peak pulse ampere. the ratio is calculated via:

$$\text{Ratio} = \frac{\text{LED}_{1+2}}{\text{LED}_1 + \text{LED}_2} \quad (5.2)$$

where LED_{1+2} is the measurement when both LEDs are on at the same time, and LED_1 and LED_2 is the measurement when they are on separately. The principle employed here is that while the intensity is within the linearity region the peak of LED_{1+2} should equal the addition of LED_1 and LED_2 separately. Therefore the ratio should be one while both peak anode ampere from the LEDs on separately and LEDs on together are within the region of linearity. As the light intensity is increased the LEDs on together will first move out of the region of linearity first. Typically this means that the peak ampere measured from both LEDs

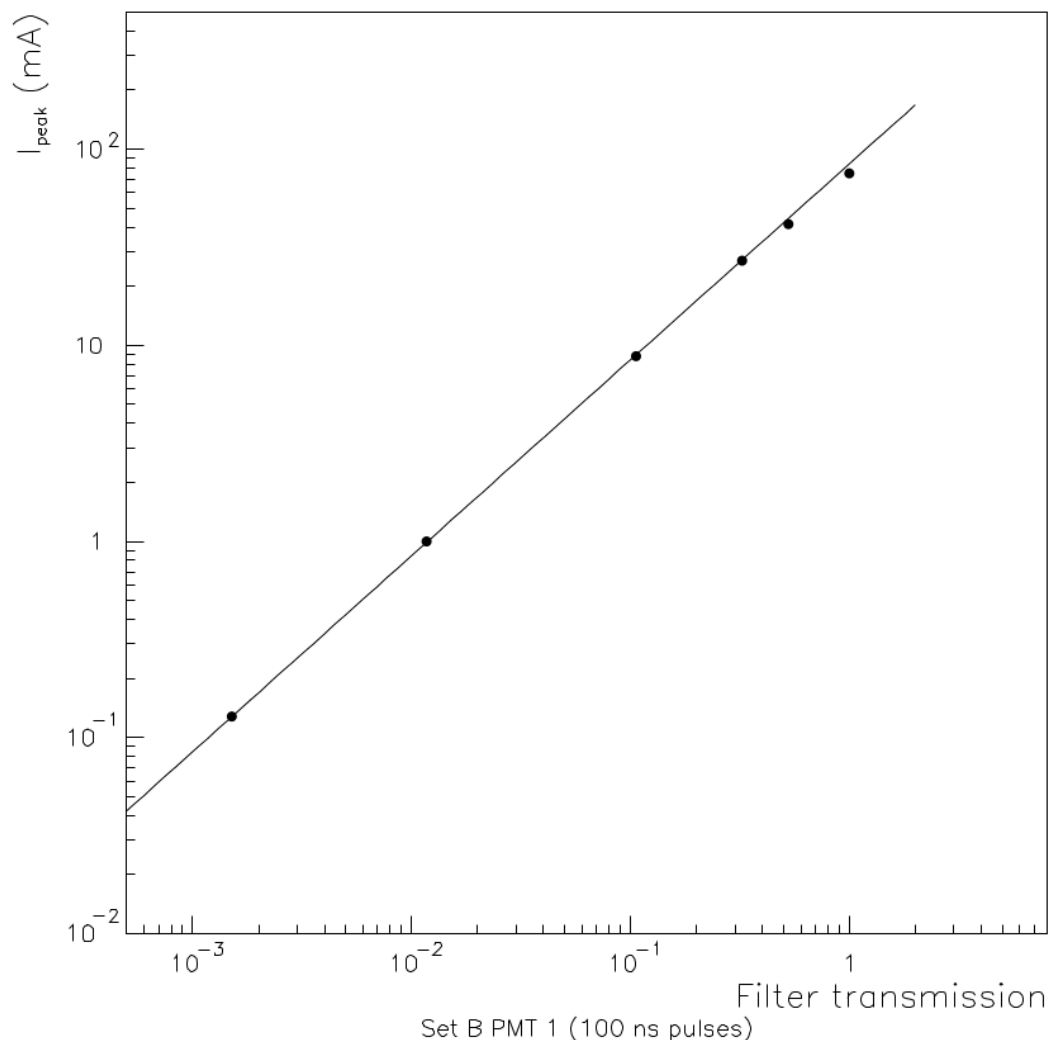


Figure 5.1: Previous PMT linearity test done by Privitera et. al. 1999 with Neutral density filters. The linearity of the PMT is shown by peak of the current against the filter transmission.

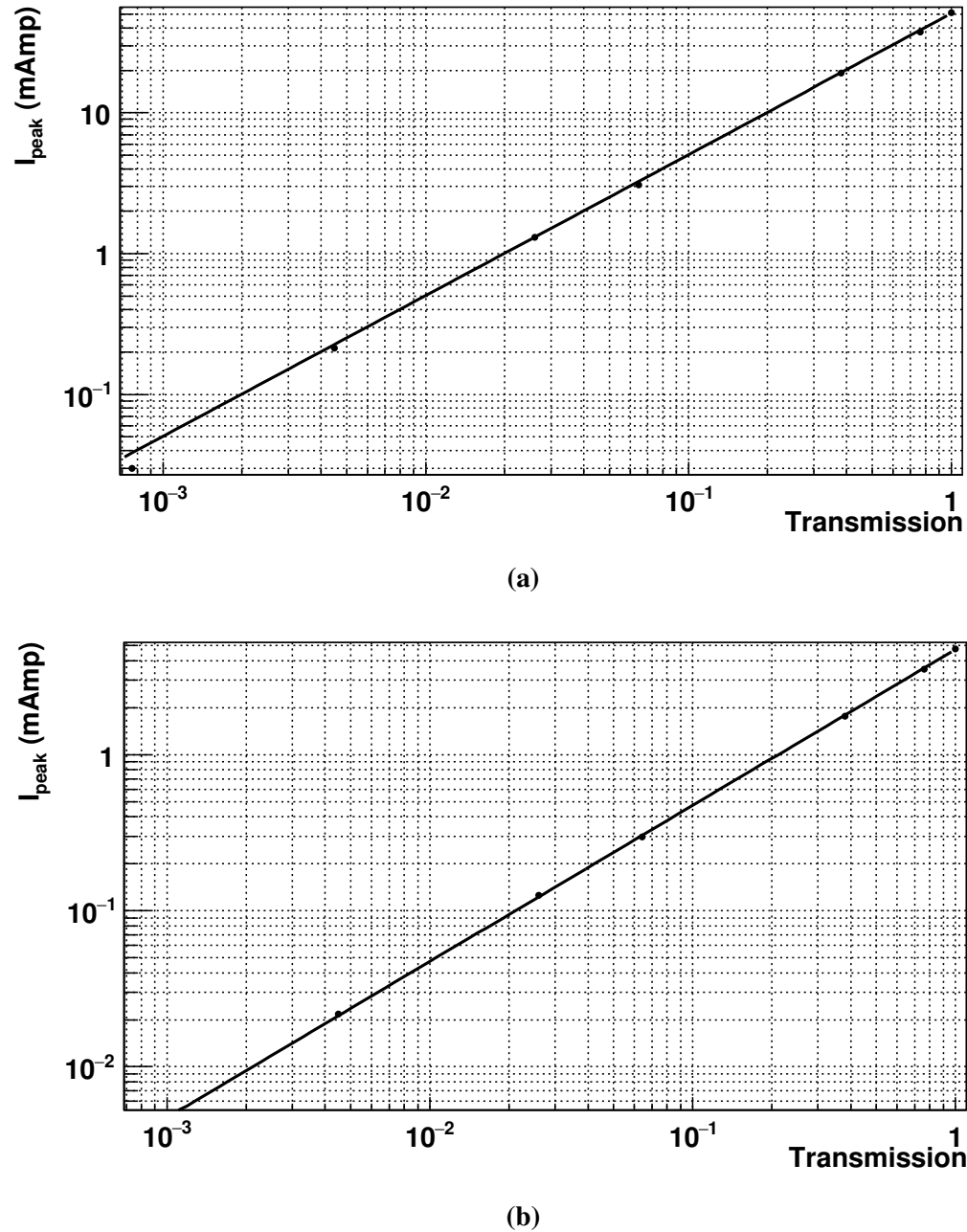


Figure 5.2: Neutral density method at 900V and 600V.

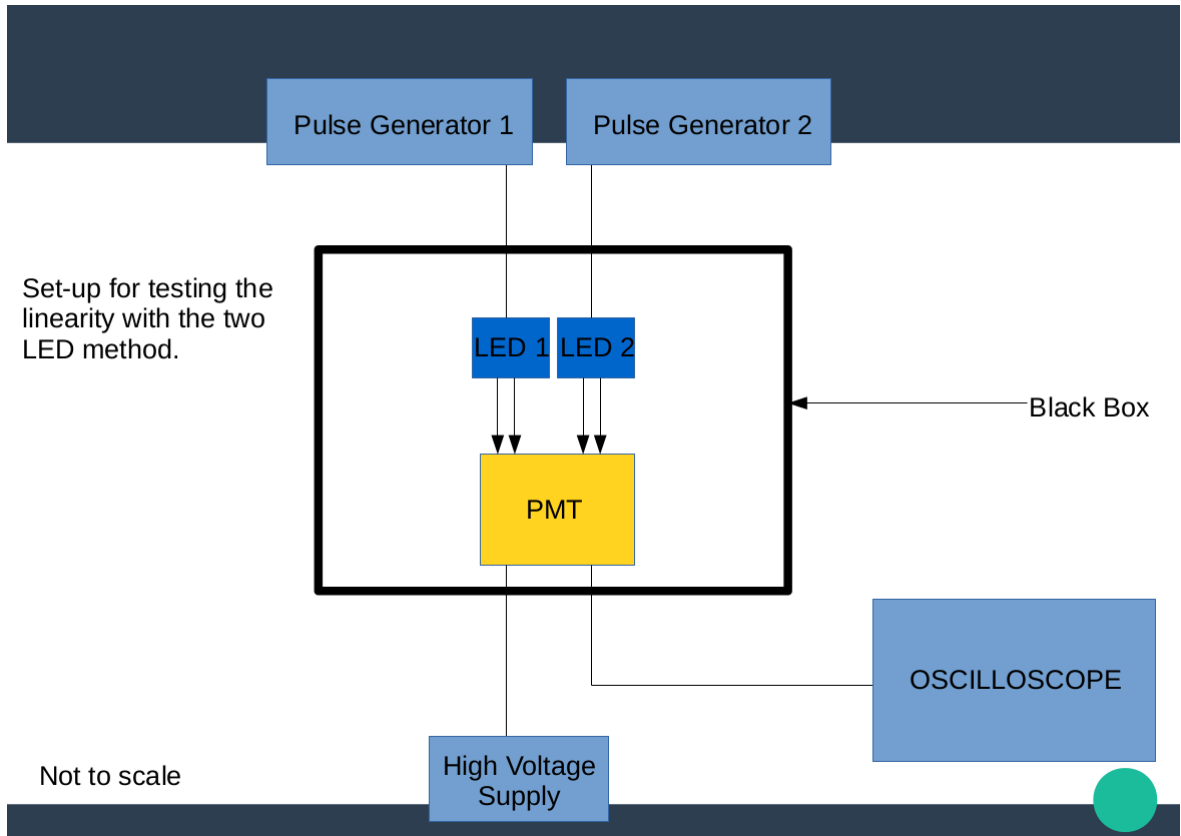


Figure 5.3: A graphical representation of the Two LED Setup used in the lab at University of Adelaide.

on at the same time will be less than the combination of the peak ampere when measured separately. This will cause the ratio to dip below one.

The advantages of this method is that any LED levels can be used and do not have to worry about the two LEDs linearity. As long as the two LED intensities are different it will produce a different response in the PMT.

The result of the two LED Method is shown in Fig. 5.4 for both 900V and 600V. The x-axis is the peak ampere of the measured pulses when both LEDs are on at the same time. The plots show that while the peak anode currents change by a close factor of 10, the gain of the PMT has also been reduced by a similar factor. This seems to indicate that the cathode is the limiting factor for the PMT linearity for this type. **Maybe quote theoretical peak anode current for a 10^{21} eV shower.**

5.4 Effects of Temperature on PMT Gain

Quoted on any PMT data sheet is the expected change in gain as a function of energy. The XP3062 PMT used in the FD telescopes is quoted to be $-0.2\%/\text{K}$. I measured this value in the lab at University of Adelaide at both 900V and 600V. The set-up to monitor the gain of the PMT involved a LED inside a copper oven pointed at the cathode pulsed once per second, and a temperature gauge. I was able to control the laboratory temperature to see the gain change over a variety of temperature values. The LED was inside a copper oven to maintain an independent constant temperature so the number of photons emitted could be considered to be fixed. The PMT was inside a box that highly light proof - the top was held

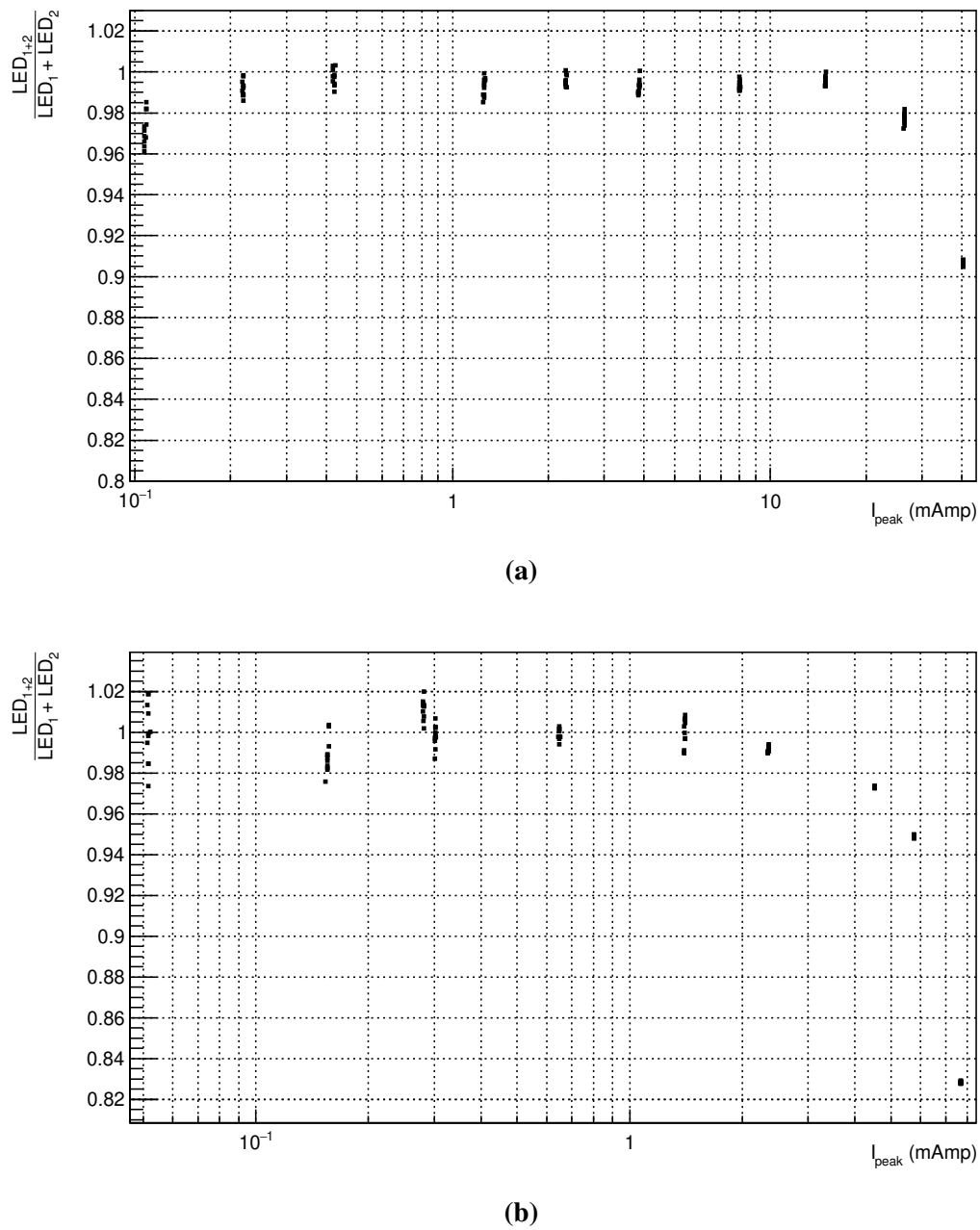


Figure 5.4: Two LED method at 900V and 600V.

down with screws, then two layers of black electrical tape was applied to the lid joinings and then a black out curtain was draped over the top. Only the temperature was allowed to vary over the measurement period. Therefore any changes in the absolute ADC measurements are related to changes in the PMT gain.

Measurements for temperature vs PMT gain was taken at both High Voltage values of 900V and 600V. The plots in Fig. 5.5 the effects of temperature on the PMT can be clearly seen at both high voltage values. For either high voltage value the measured PMT gain changer per K was $-0.6\%\text{K}$ **needs uncertainty**. This maybe different to the quoted data sheet but is not unreasonable. The quoted data sheet is an average of many PMTs while this is a measurement of one particular PMT. What was interested was that this value did not deviate if using the PMT at 900V or 600V.

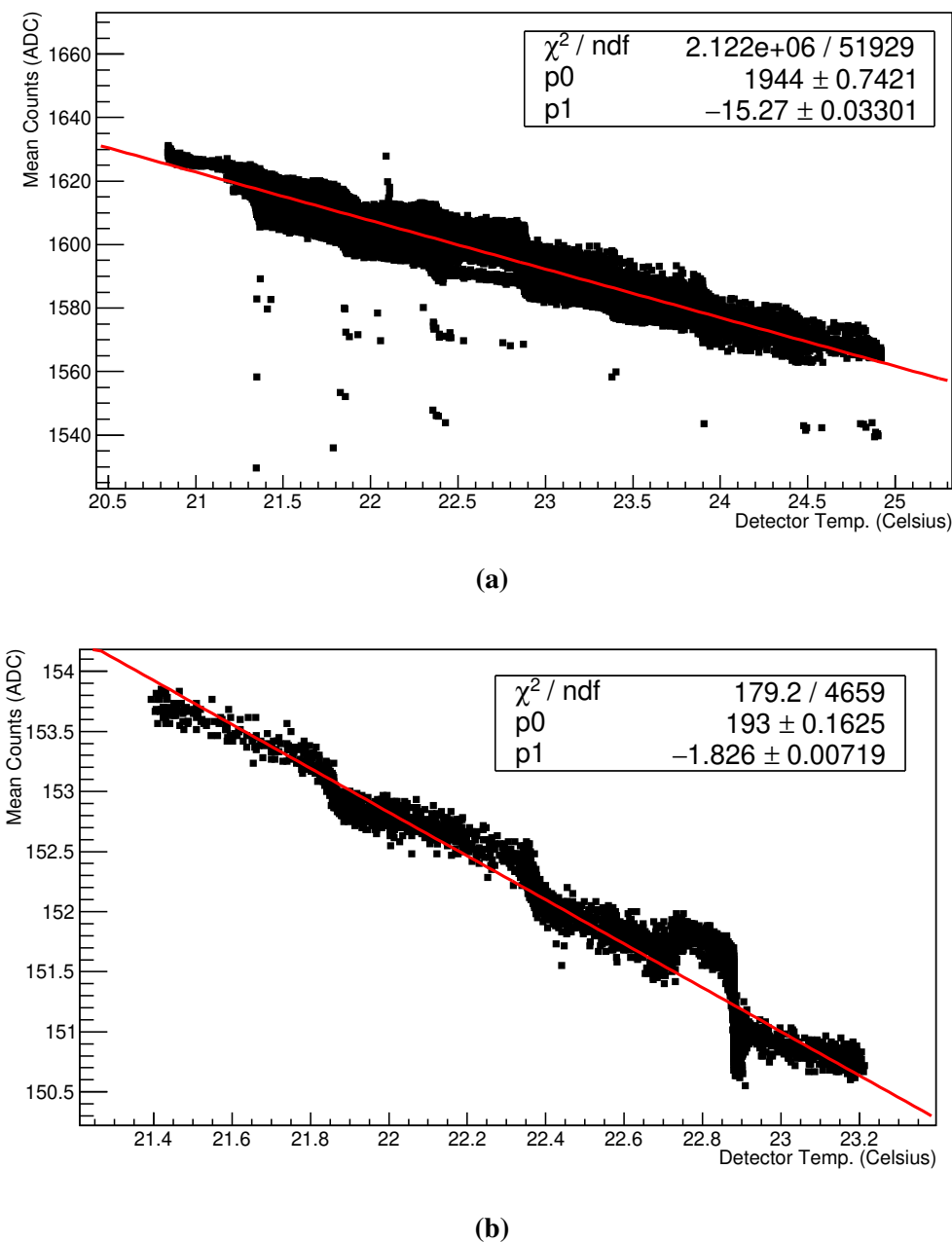


Figure 5.5: Showing the how PMT gain correlates with surrounding temperature.

Chapter 6

Computer Simulation of Fluorescence Detector Photomultiplier Tubes

Simulating the FD PMT under differing NSB and for different reasons.

- Theoretical value for Gain Variance
- PMT Gain Variance
- Show both for flat distribution and Gaussian variations for dynodes
- Results
- FD FLT under increased NSB

6.1 Motivation

- PMT Theory/Background

6.2 Method and Theory

For a deeper understanding of how the PMT gain variance works I used a toy model Monte Carlo to simulate electrons moving throughout the PMT dynode chain. Gain Variance is the Gaussian broadening of the measured anode signal. The number of electrons that are emitted from each dynode follows a Poisson distribution. When an electron hits a dynode the number of electrons emitted follow a probability distribution that is Poisson in shape. As electrons travel further down the dynode chain and the number of electrons emitted per dynode increase the distribution becomes more Gaussian like.

To simulate the Gain Variance within a PMT I set-up my toy model to match the number of stages with the XP3062 PMT. I was only looking at the single photo-electron case (ie. where only a single electron is emitted from the cathode.). If there was no extra broadening then the distribution would be dictated by the Poisson distribution. For each electron that hits a dynode a random number generator is used to determine the number of electrons that leave the dynode.

- Lot more detail. Through how the toy model is produced.

Draw flow chart of toy model Monte Carlo.

6.2.1 Theoretical value of Gain Variance?

I investigated different scenarios - firstly each dynode able to emit electrons with uniform Poission distribution across its surface and secondly each dynode having some sort of irregularity across its surface. The irregularity was added by shifting the mean of the Poisson distribution by sampling from a random Gaussian distribution. The gain variance was investigated at different PMT gain values. The PMT gain values picked was equivalent to a high voltage across the PMT of 1300V, 900V and 600V. The high voltage of 1300V was picked as a direct gain variance measurement was preformed by **some group within Auger**, 900V is the typical high voltage used when the FD telescopes are operating and 600V is the approximate high voltage that is expected to be used when the FD telescopes are observing under increased NSB conditions.

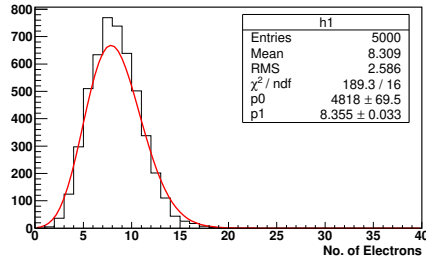
6.3 Results of PMT Gain Variance Simulation

6.4 Simulation of Gain Variance Method

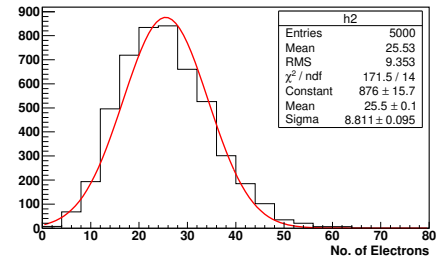
- Show off histogram of simulated Gain Variance Ratios
- Show that there's a natural spread
- some of the calculated ratio's will be less then one due to spread in measure variances
- differences in methods? Pairs vs averages method should return the same results
- benefits of combining noise traces over using just 140 bins per trace.

6.5 FD FLT under different NSB levels

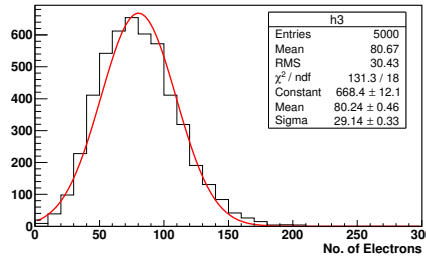
Looked at study to simulate the effects of increased NSB on the First Level Trigger (FLT). The Auger maintains the FLT to trigger at 100 Hz range. From simulations with different NSB levels it can be seen trigger threshold above the mean would be required to maintain the expected trigger level. The NSB of $2.71 \backslash 100$ ns is the typical NSB level observed at the site. From there I picked 5 increased NSB levels to show how threshold above the mean changes.



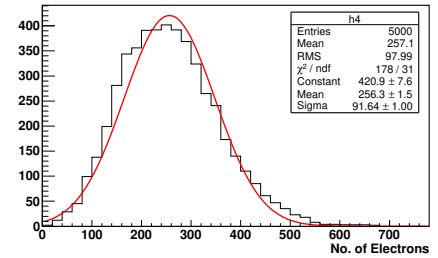
(a) Distribution of simulated electrons leaving dynode 1. The red line is a fitted Poisson distribution.



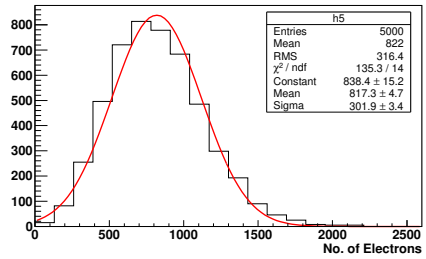
(b) Distribution of simulated electrons leaving dynode 2. The red line is a fitted Gaussian distribution.



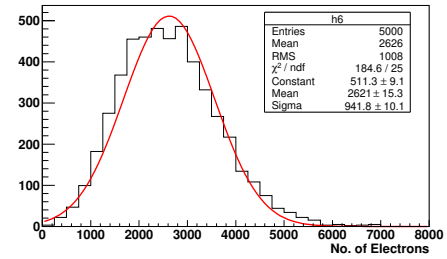
(c) Distribution of simulated electrons leaving dynode 3. The red line is a fitted Poisson distribution.



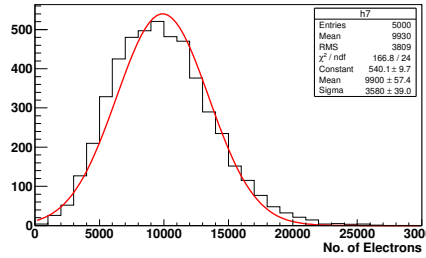
(d) Distribution of simulated electrons leaving dynode 4. The red line is a fitted Gaussian distribution.



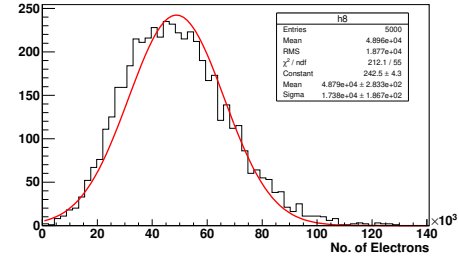
(e) Distribution of simulated electrons leaving dynode 5. The red line is a fitted Poisson distribution.



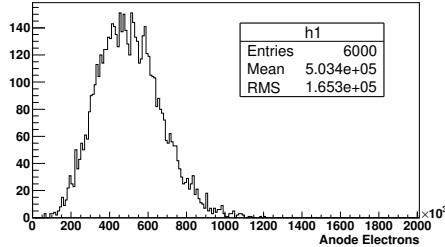
(f) Distribution of simulated electrons leaving dynode 6. The red line is a fitted Gaussian distribution.



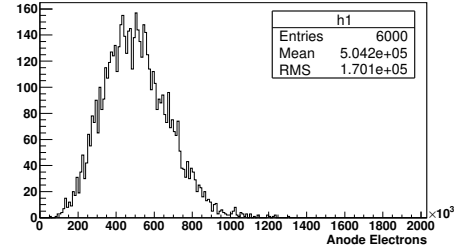
(g) Distribution of simulated electrons leaving dynode 7. The red line is a fitted Poisson distribution.



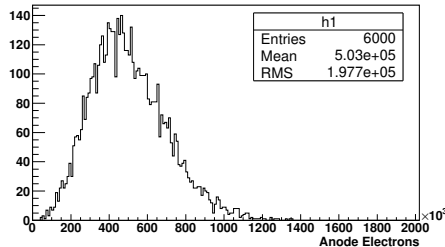
(h) Distribution of simulated electrons leaving dynode 8. The red line is a fitted Gaussian distribution.



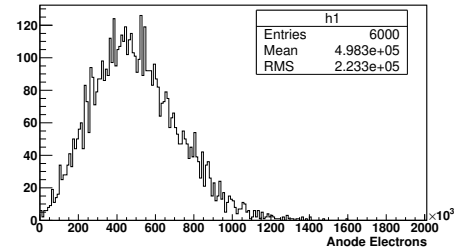
(a) Simulated observed signal from PMT anode with 8 stages and gain of 5×10^5 . Poisson fluctuations at each stage only. No each Gaussian broadening at any dynode.



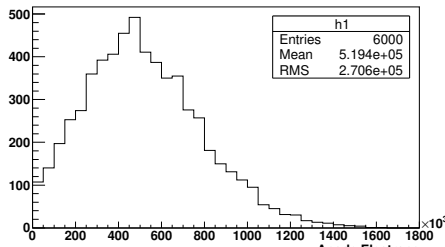
(b) Simulated observed signal from PMT anode with 8 stages and gain of 5×10^5 . Poisson fluctuations at each stage only. Added Gaussian broadening at each dynode of 10%.



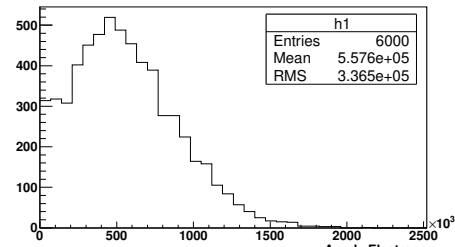
(c) Simulated observed signal from PMT anode with 8 stages and gain of 5×10^5 . Poisson fluctuations at each stage only. Added Gaussian broadening at each dynode of 20%.



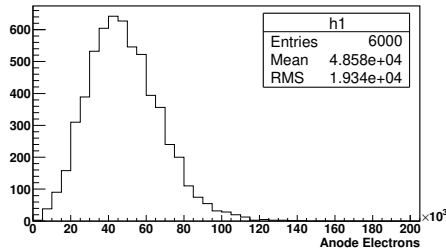
(d) Simulated observed signal from PMT anode with 8 stages and gain of 5×10^5 . Poisson fluctuations at each stage only. Added Gaussian broadening at each dynode of 30%.



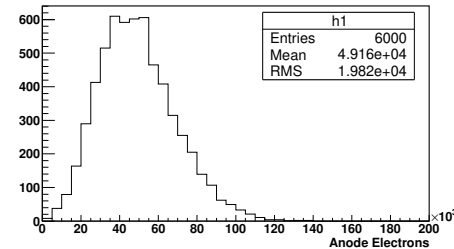
(e) Simulated observed signal from PMT anode with 8 stages and gain of 5×10^5 . Poisson fluctuations at each stage only. Added Gaussian broadening at each dynode of 40%.



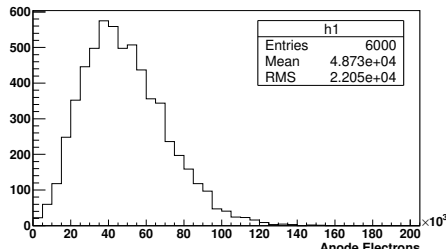
(f) Simulated observed signal from PMT anode with 8 stages and gain of 5×10^5 . Poisson fluctuations at each stage only. Added Gaussian broadening at each dynode of 50%.



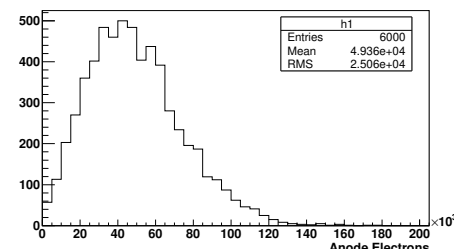
(a) Simulated observed signal from PMT anode with 8 stages and gain of 5×10^4 . Poisson fluctuations at each stage only. No Gaussian broadening at any dynode.



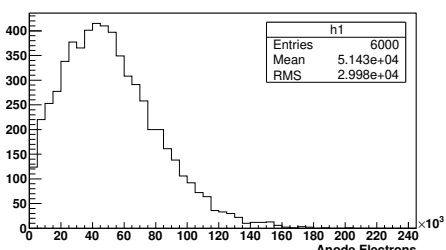
(b) Simulated observed signal from PMT anode with 8 stages and gain of 5×10^4 . Poisson fluctuations at each stage only. Added Gaussian broadening at each dynode of 10%.



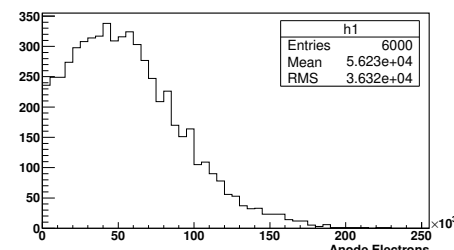
(c) Simulated observed signal from PMT anode with 8 stages and gain of 5×10^4 . Poisson fluctuations at each stage only. Added Gaussian broadening at each dynode of 20%.



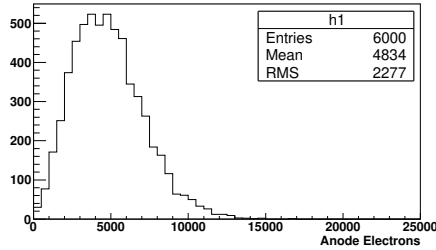
(d) Simulated observed signal from PMT anode with 8 stages and gain of 5×10^4 . Poisson fluctuations at each stage only. Added Gaussian broadening at each dynode of 30%.



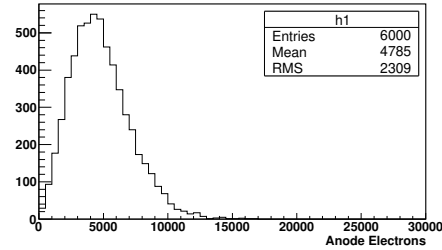
(e) Simulated observed signal from PMT anode with 8 stages and gain of 5×10^4 . Poisson fluctuations at each stage only. Added Gaussian broadening at each dynode of 40%.



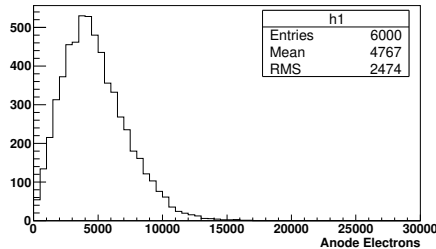
(f) Simulated observed signal from PMT anode with 8 stages and gain of 5×10^4 . Poisson fluctuations at each stage only. Added Gaussian broadening at each dynode of 50%.



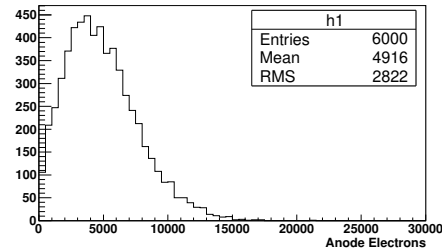
(a) Simulated observed signal from PMT anode with 8 stages and gain of 5×10^3 . Poisson fluctuations at each stage only. No Gaussian broadening at any dynode.



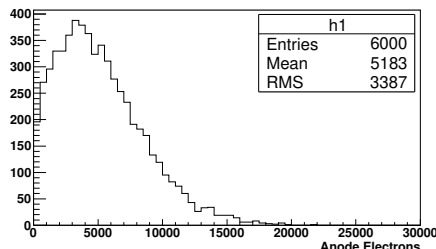
(b) Simulated observed signal from PMT anode with 8 stages and gain of 5×10^3 . Poisson fluctuations at each stage only. Added Gaussian broadening at each dynode of 10%.



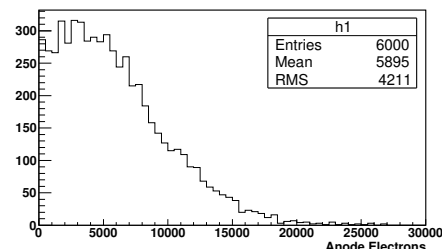
(c) Simulated observed signal from PMT anode with 8 stages and gain of 5×10^3 . Poisson fluctuations at each stage only. Added Gaussian broadening at each dynode of 20%.



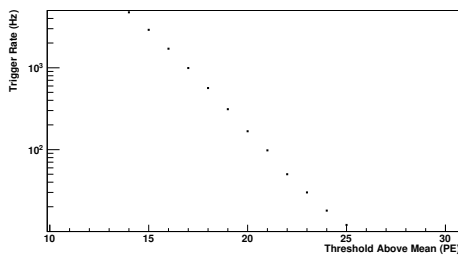
(d) Simulated observed signal from PMT anode with 8 stages and gain of 5×10^3 . Poisson fluctuations at each stage only. Added Gaussian broadening at each dynode of 30%.



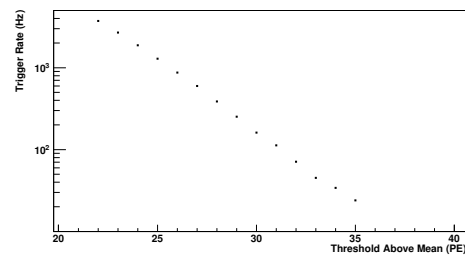
(e) Simulated observed signal from PMT anode with 8 stages and gain of 5×10^3 . Poisson fluctuations at each stage only. Added Gaussian broadening at each dynode of 40%.



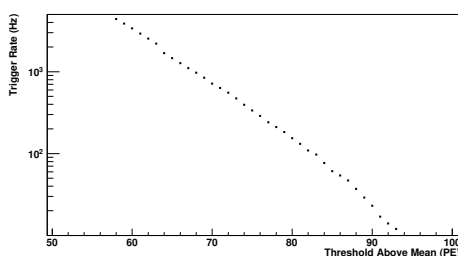
(f) Simulated observed signal from PMT anode with 8 stages and gain of 5×10^3 . Poisson fluctuations at each stage only. Added Gaussian broadening at each dynode of 50%.



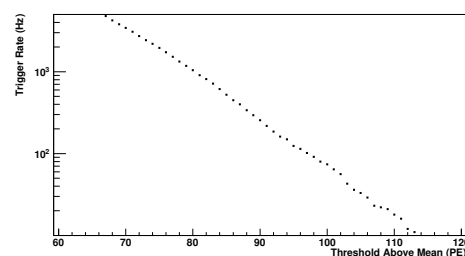
(a) FLT simulation with NSB of 2.71 pe / 100ns.



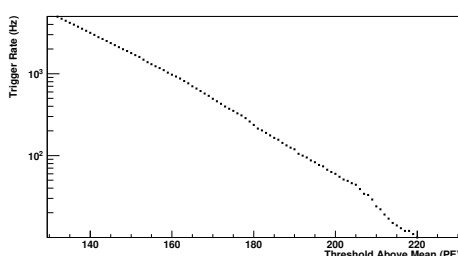
(b) FLT simulation with NSB of 6.60 pe / 100ns.



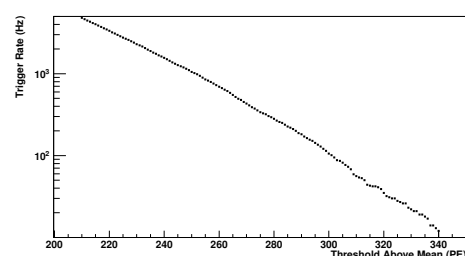
(c) FLT simulation with NSB of 46.8 pe / 100ns.



(d) FLT simulation with NSB of 65.8 pe / 100ns.



(e) FLT simulation with NSB of 263 pe / 100ns.



(f) FLT simulation with NSB of 657 pe / 100ns.

Chapter 7

Measuring Fluorescence Detector Photomultiplier Gain Variance with CalA Data

Measuring Gain Variance of FD PMT with CalA Data

- Measuring Gain Variance in the lab did not work. Equipment was not sensitive enough to the low current.
- There were issues with calibrating the LED light source with another PMT (QE curve and wavelength response not the same?)
- Using Low/Standard measurements of CalA to find Gain Variance Ratio
- Two different methods
- Bootstrap method to find uncertainties on Method 2

7.1 Motivation

- Background

- Why?

The absolute value of the gain variance cannot be found but using the CalA data a relative change can be found. This is useful for the collaboration simulations as a Gain variance is coded for the PMT at standard voltage settings. Finding out the relative change in gain variance would be useful to be used for simulations of the FD PMTs at a lower voltage settings (eg. 600V).

7.2 Using CalA to measure relative changes in Gain Variance

I am using CalA data from the FD telescopes to measure the relative changes in PMT gain variance as the gain was changed by a factor of 10. CalA data is calibration data used to monitor any changes in PMT gain as a function of time. CalA is performed at the beginning and end of a nightly observation while FDs are operated. Pulses of light are piped via fibre

optics cables which is pointed at each of the Fd telescope cameras. Each CalA run is a set of 50 pulses which have a width of approximately $60 \mu\text{s}$.

show image of CalA pulse

One of the values that can be calculated from the CalA is denoted K_V . The value K_V is calculated via:

$$K_V = \frac{\text{Mean}}{\text{Sigma}^2} = \frac{10}{2 \times G(1 + V_G) \times F} \quad (7.1)$$

The Mean is the average ADC count of the observed CalA pulse seen in the FD pixel. The Sigma² is the variance calculated around a fit to the signal in ADC². The signal has a slope due to the effects of a capacitor used to remove the DC component of the signal. The slope is proportional to the time constant of the capacitor employed. G is the PMT gain, F is the noise equivalent bandwidth (Hz) and V_G is the PMT gain variance.

The method used to measure the ratio in gain variance is to take the calculated means and sigmas from the pulses and then finding a ratio between the K_V and Gains at the two different voltage settings.

$$K = \frac{\text{Mean}}{\text{Sigma}^2} = \frac{10}{2 \times G(1 + V_G) \times F} \quad (7.2)$$

$$\frac{(K_V)_{\text{Low}}}{(K_V)_{\text{Stand}}} = \frac{\text{Mean}_{\text{Low}}}{\text{Sigma}_{\text{Low}}^2} \div \frac{\text{Mean}_{\text{Stand}}}{\text{Sigma}_{\text{Stand}}^2} \quad (7.3)$$

$$\frac{\text{Mean}_{\text{Low}}}{\text{Sigma}_{\text{Low}}^2} \div \frac{\text{Mean}_{\text{Stand}}}{\text{Sigma}_{\text{Stand}}^2} = \frac{G_{\text{Stand}}(1 + V_G)_{\text{Stand}}}{G_{\text{Low}}(1 + V_G)_{\text{Low}}} \quad (7.4)$$

$$\frac{G_{\text{Stand}}}{G_{\text{Low}}} = \frac{\text{Mean}_{\text{Stand}}}{\text{Mean}_{\text{Low}}} \quad (7.5)$$

$$\frac{(1 + V_G)_{\text{Low}}}{(1 + V_G)_{\text{Stand}}} = \frac{\text{Sigma}_{\text{Low}}^2 \times \text{Mean}_{\text{Stand}}^2}{\text{Sigma}_{\text{Stand}}^2 \times \text{Mean}_{\text{Low}}^2} \quad (7.6)$$

7.3 Electronic Noise

I investigated the consistency of the electronic noise across a set of 50 CalA traces. The consistency was looked at as there is only about 140 bins of noise before each of the signal pulse starts. Therefore finding an accurate mean and variance of the electronic noise on individual pulses is difficult. An accurate measurement of the electronic noise mean and variance was required as the measured change in the relative gain variance ratio was only a few percent.

Need to show electronic noise as function of time.

An example of a pixel electronic noise trace is shown in Fig. ???. It can be seen in this figure that stitching all of the noise bins from the 50 traces is remarkably stable. This result allows for all the noise for a single PMT pixel to be placed into a histogram to find a more accurate value for the mean and variance.

7.4 Pairs Method

For both standard and lower voltage settings, 50 sets of pulses are recorded for the CalA analysis. The pair method involves taking single CalA shots from standard and lower voltage settings and fitting an exponential to the signal. The fitted exponential is used to find the mean value at the top of the signal and the variance around the fit. For each pixel 50 values

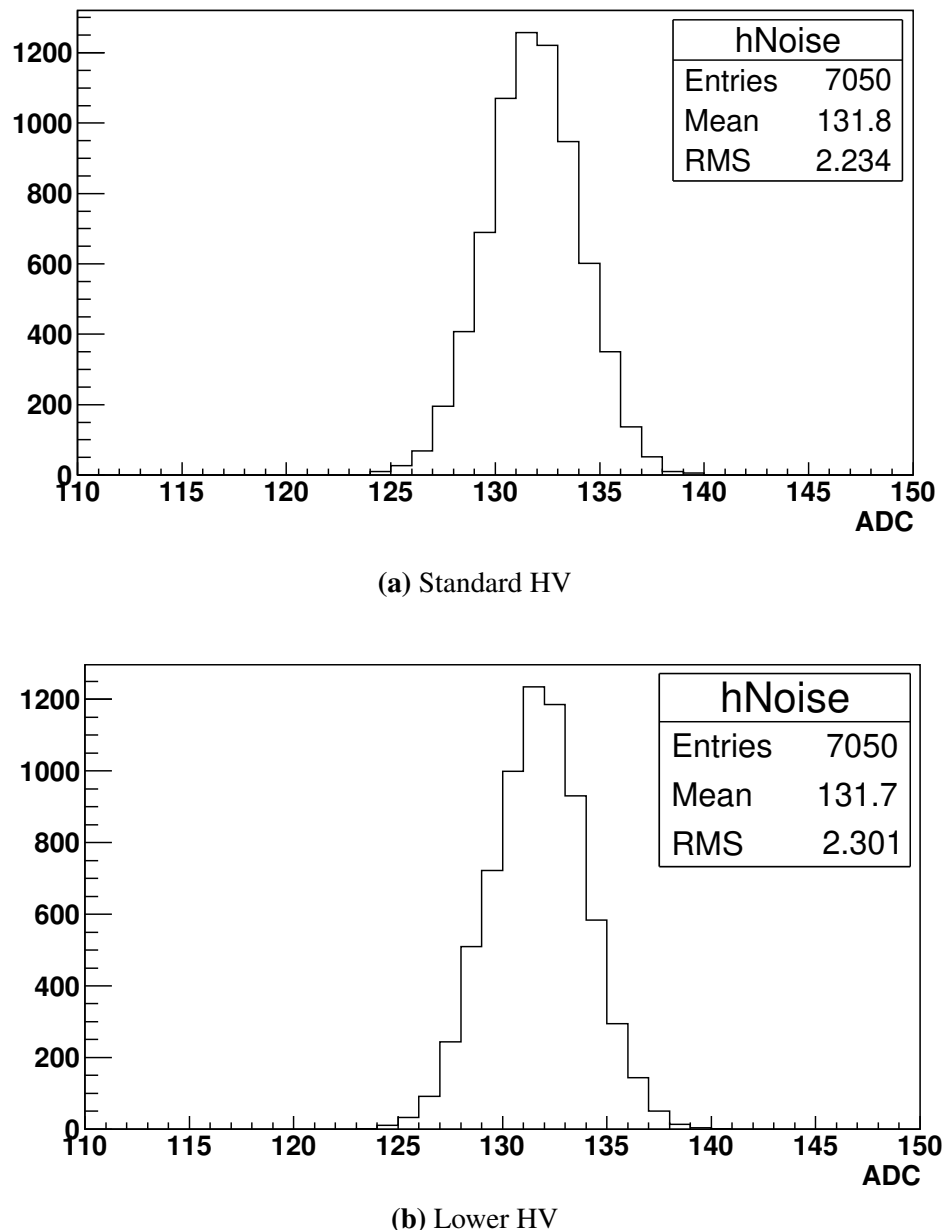


Figure 7.1: Sample of the observed electronic noise observed for a single pixel within Los Leones telescope 4. Electronic noise outside of the PMT so will be the same separate from the HV setting across the PMT.

for the Gain Variance ratio was found and this was repeated for the 440 pixels within the FD telescope camera.

Fig. 7.3 shows the average ADC found across a camera for a FD telescope. The pattern follows how the camera is illuminated by the LED pointing at it. It shows that the spot is brightest in the middle and the intensity drops off towards the edges **need to add in diagram of labelled pixel no. across a FD camera**. There are uncertainties on the averages, but are smaller than the points displayed on the figures. The variance measured in Fig. 7.5 shows an expected pattern also. The variance is proportional to the mean and is expected to follow a similar shape. This will not be exact but a good indicator of whether the variance was calculated correctly.

7.4.1 Results

Fig. 7.6 and Fig. 7.7 shows a demonstration of using the Pairs Method to calculate the Gain Variance Ratio. The CalA data used was taken on the night of the 11-06-2016 by Los Leones Mirror 4. The mean value in Fig. 7.6 shows a 3.7% change in the ratio which translates to a 10% change in the actual value of the PMT gain variance.

Fig. 7.7 shows the gain variance ratio measured per pixel. There can be seen no major structure or pattern. This is desired as the Gain variance is tied to individual PMTs and it would not be a great sign if the ratio followed a pattern like what was seen for the means and variances.

7.5 Averaging Sets of Traces Method

Instead of calculating the Gain Variance ratio on pairs of CalA traces then finding an average value the 50 traces for each set are stacked. This forms an average trace consisting of the 50 traces. To find the mean and variances of the noise a linear line of form $f(x) = x$ is fitted to the first 140 bins. The fitted x is used as the mean and the variance is calculated around this value. Next an exponential is fitted to the signal. The value of the fit at the top of the signal is used as the mean while the variance is calculated around the fitted exponential.

7.5.1 Results

There is a larger spread in the histogram of calculated Gain Variance ratio than when the Pairs Method was employed. One good property is that no visible structure or pattern can be seen. There are definitely some extreme values of the ratio measured. To see what could cause the large outliers I had a look at the reduced chi-square of the fitted function to the noise and signal. There was no obvious problems when looking at the chi-squares as a function of pixel number for the signal. Examples are shown in Fig. 7.14 and Fig. 7.15. Examining the reduced chi-square of the fits to the noise it was seen that there were some large values. This was shown in Fig. 7.16 and Fig. 7.17. What was causing these weird fits was one or more of the noise bins having a larger deviation than expected from the measured average. **Add in plot showing off this behaviour**. This led to the process of investigating whether Least Trimmed Squares would be useful.

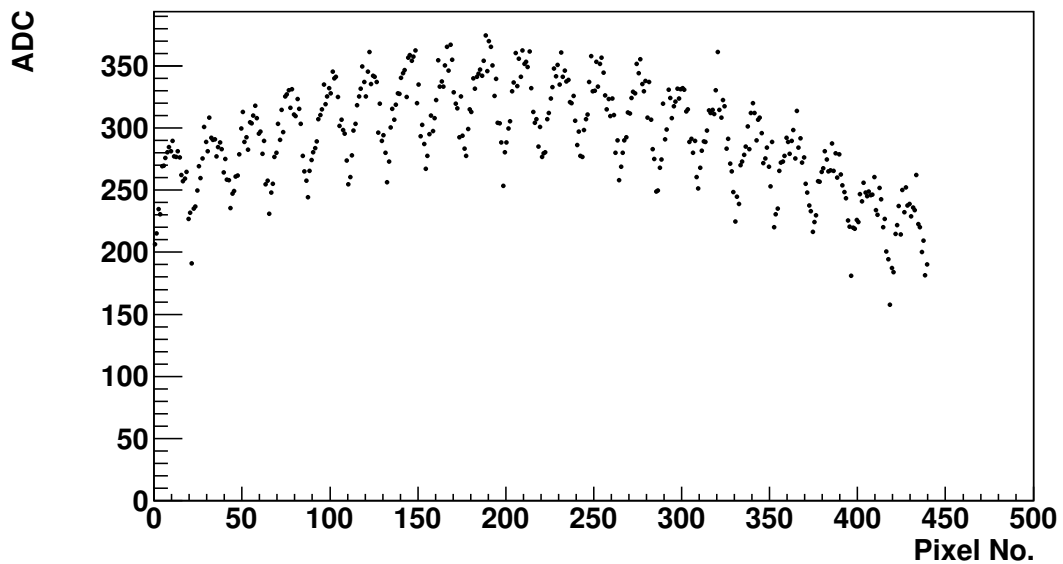


Figure 7.2: Mean measured at Standard HV for Los Leones Mirror 4. CalA data taken on the 11-06-2016.

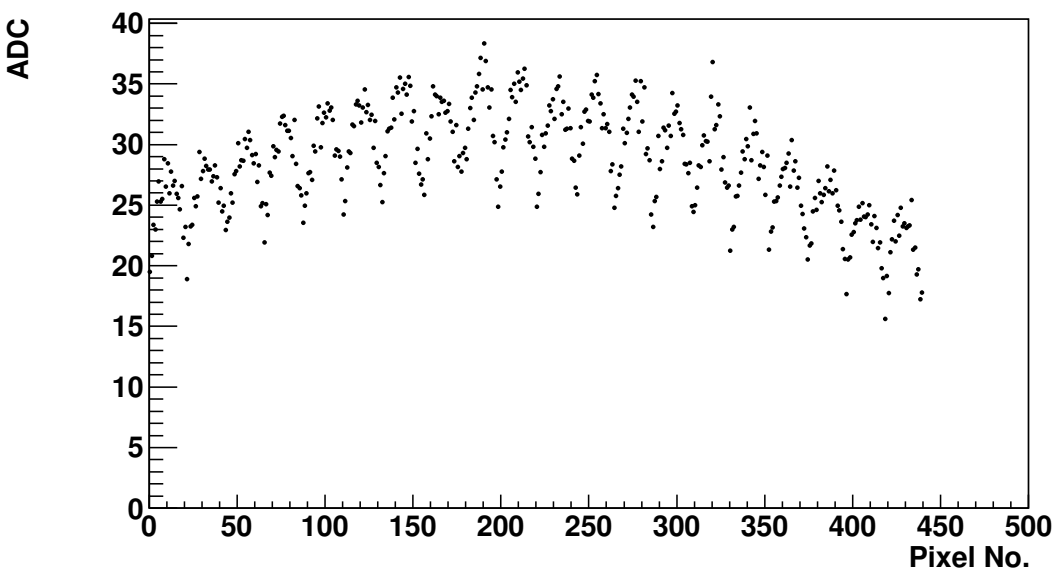


Figure 7.3: Mean measured at Lower HV for Los Leones Mirror 4. CalA data taken on the 11-06-2016.

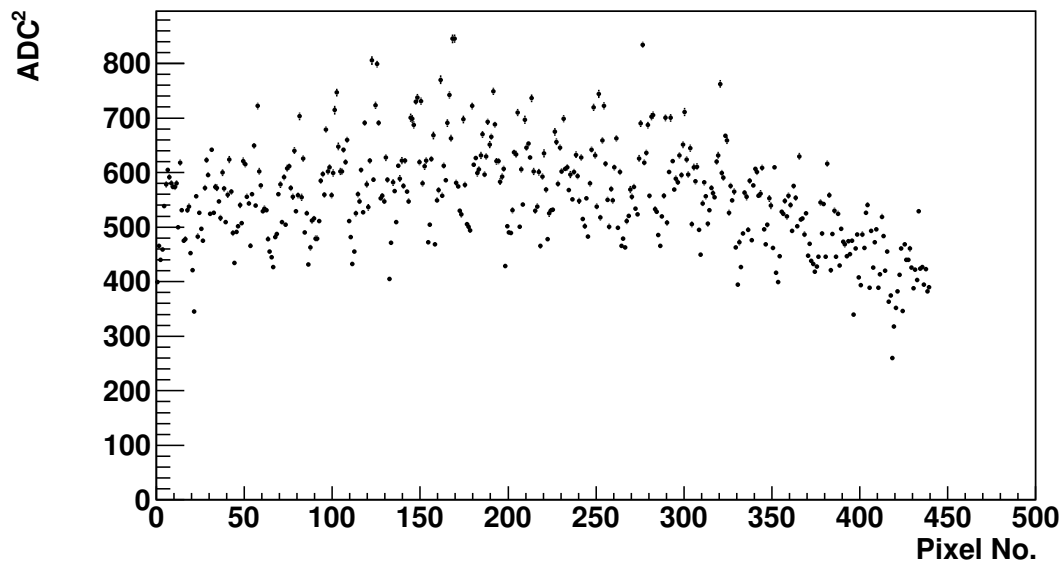


Figure 7.4: Variance measured at Standard HV for Los Leones Mirror 4. CalA data taken on the 11-06-2016.

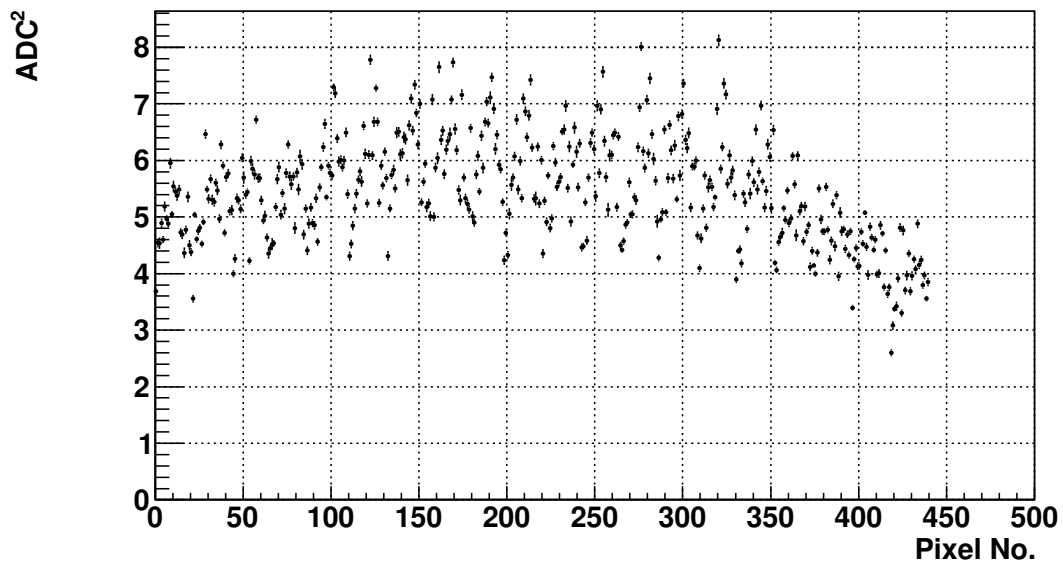


Figure 7.5: Varaince measured at Lower HV for Los Leones Mirror 4. CalA data taken on the 11-06-2016.

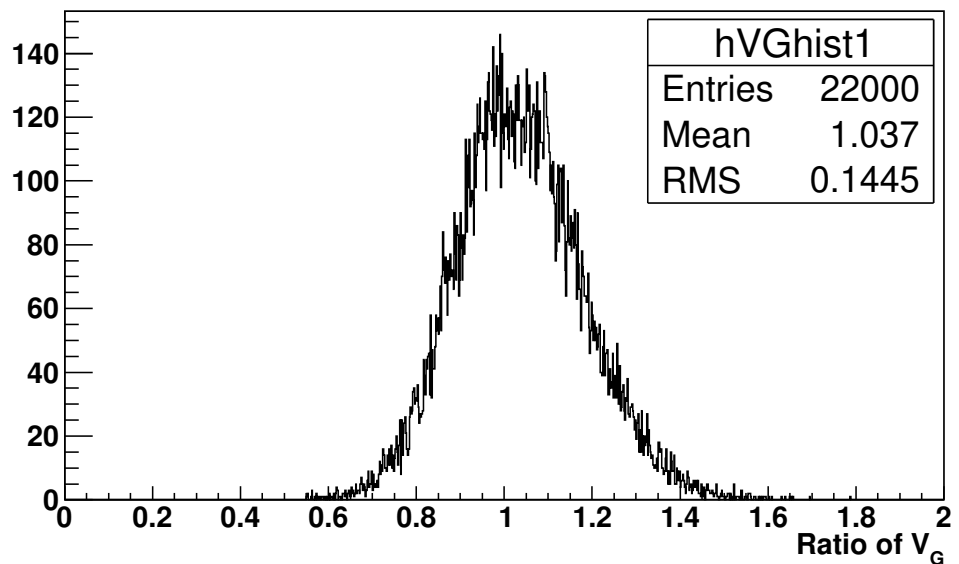


Figure 7.6: Histogram of the all the pairs methods for Los Leones Mirror 4. CalA data was taken on the 11/06/2016 at both Standard and Lower gain settings. There are 50 traces for each of the 440 pixels recorded at both gain settings.

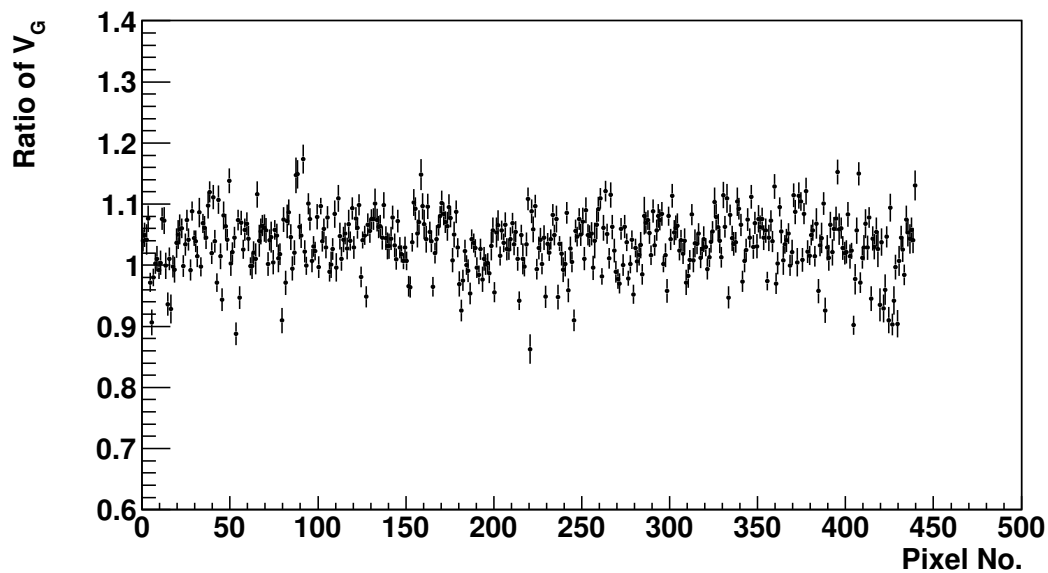


Figure 7.7

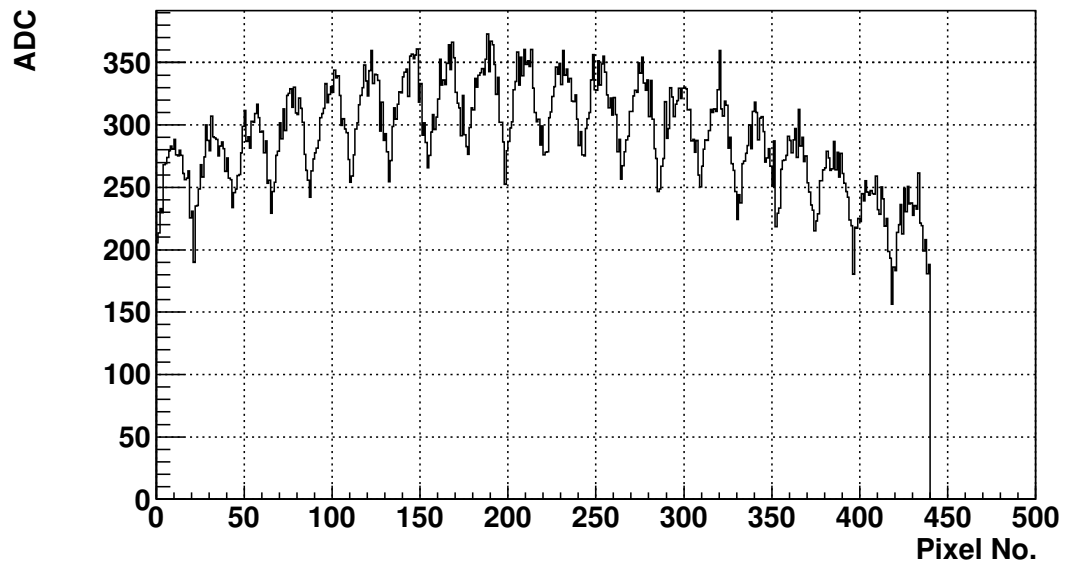


Figure 7.8

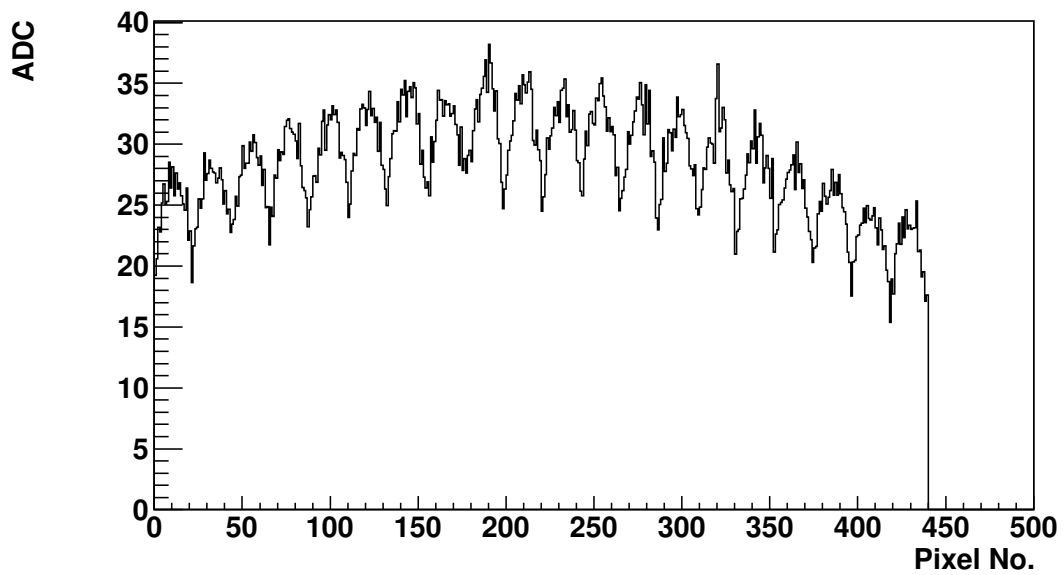


Figure 7.9

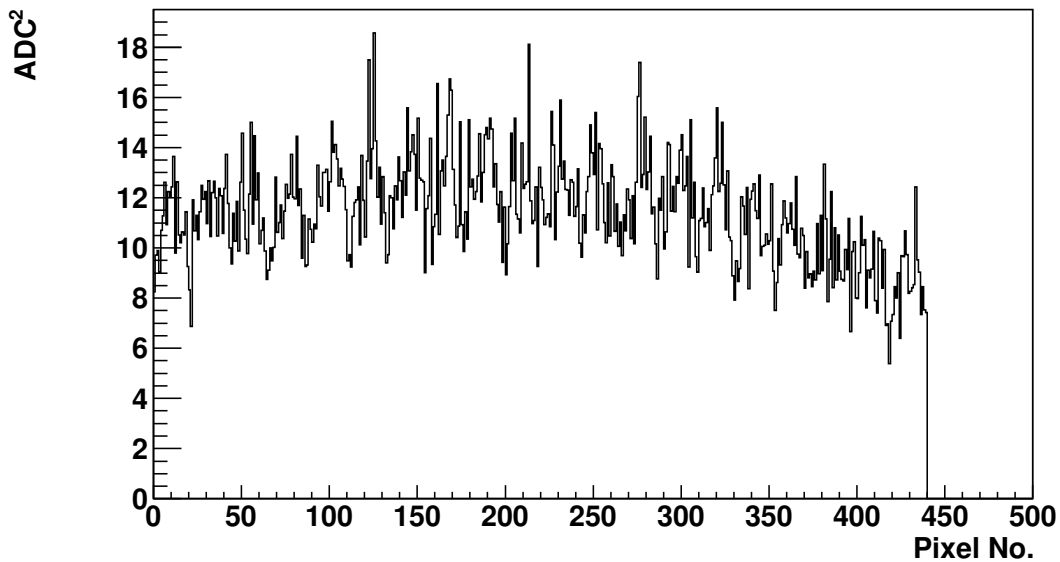


Figure 7.10

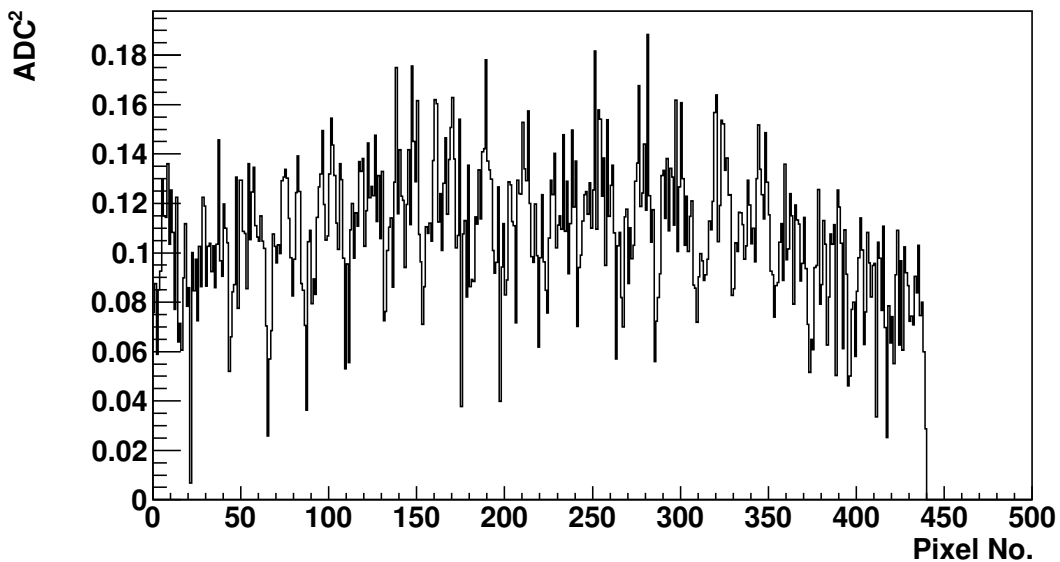


Figure 7.11

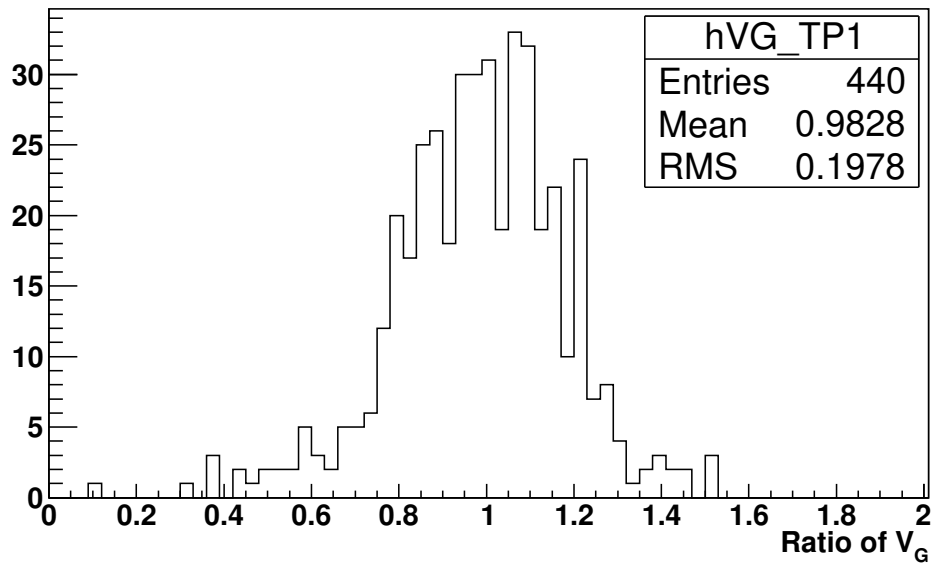


Figure 7.12

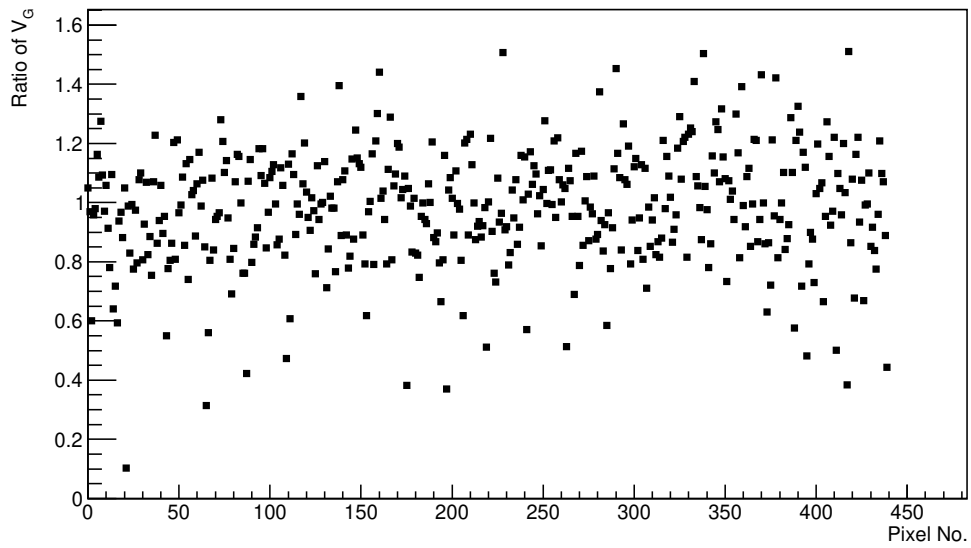


Figure 7.13

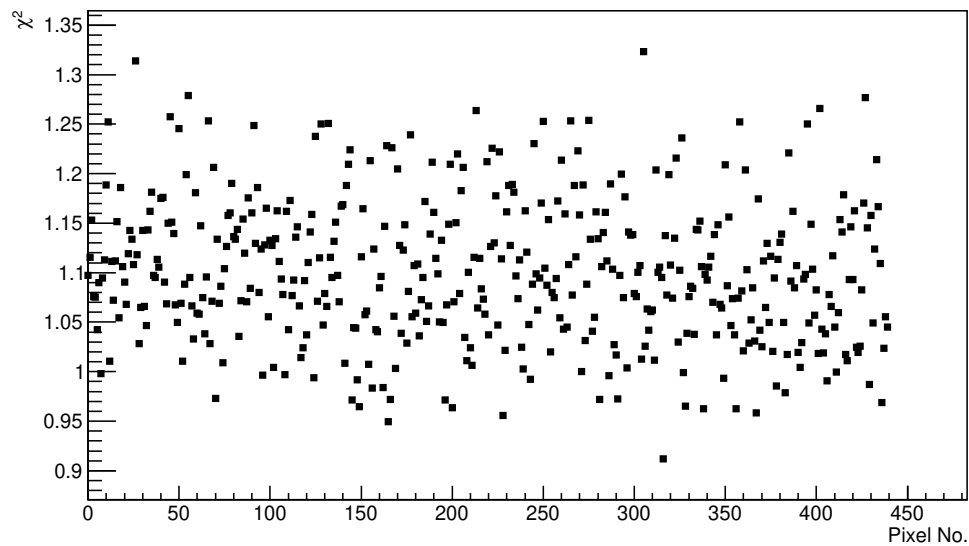


Figure 7.14: Reduced Chi-square for fitted exponential on the signal for CalA events measured at Standard HV.

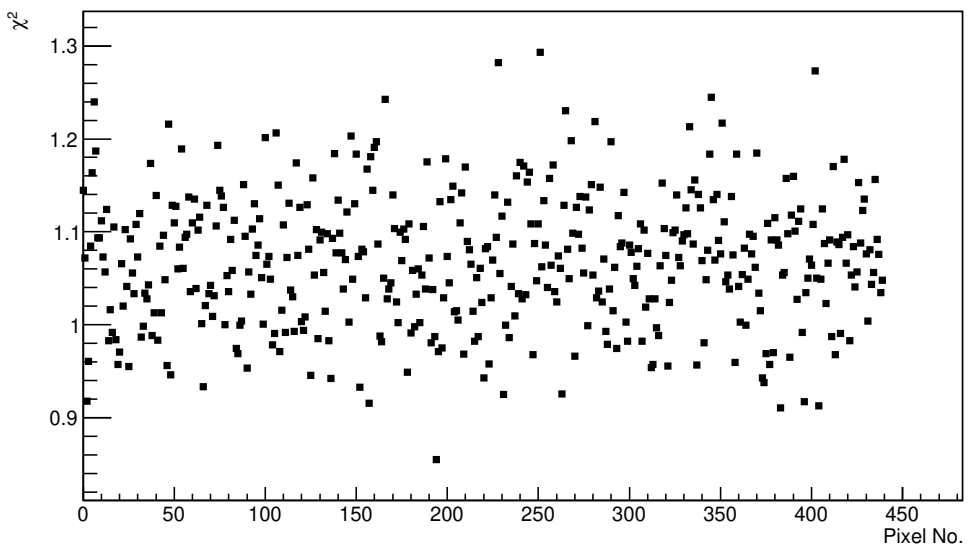


Figure 7.15: Reduced Chi-square for fitted exponential on the signal for CalA events measured at Lower HV.

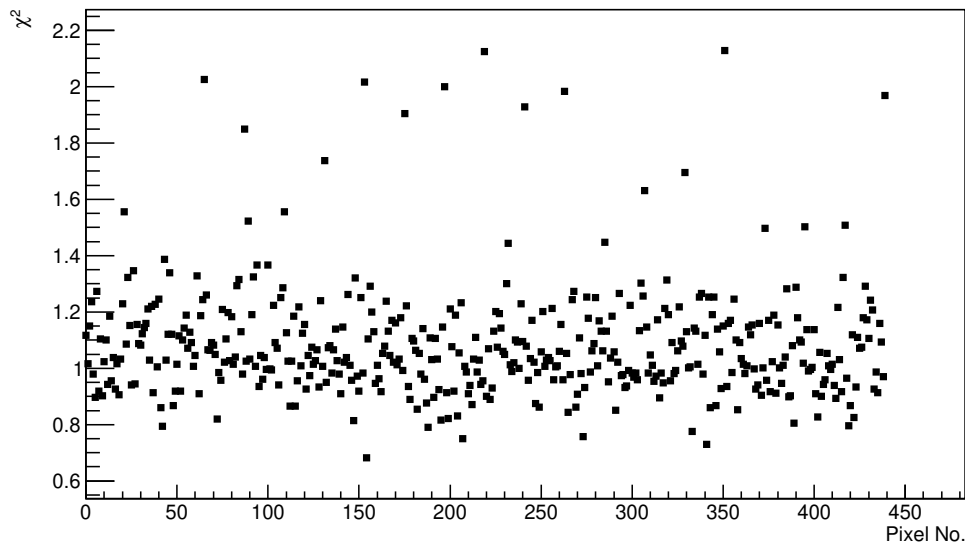


Figure 7.16: Reduced Chi-square for fitted line on the signal for CalA events measured at Standard HV.

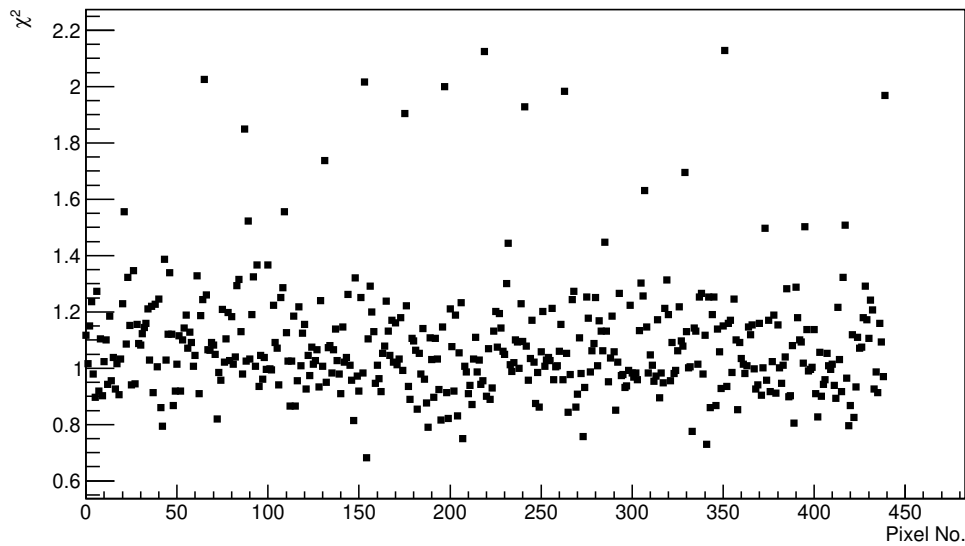


Figure 7.17: Reduced Chi-square for fitted line on the signal for CalA events measured at Lower HV.

7.6 Result of Averaging Sets of Traces Method with Least Trimmed Squares

Least Trimmed Square is the method that involves removing points that have the greatest sigma away from an initial fit. A point is removed one at a time with the fit repeated and the reduced chi-square checked. This method is repeated until the reduced chi-square is below a threshold.

7.7 Result of Averaging Sets of Traces Method using Noise Distribution

7.8 Attempts to measure Gain Variance directly in the Lab

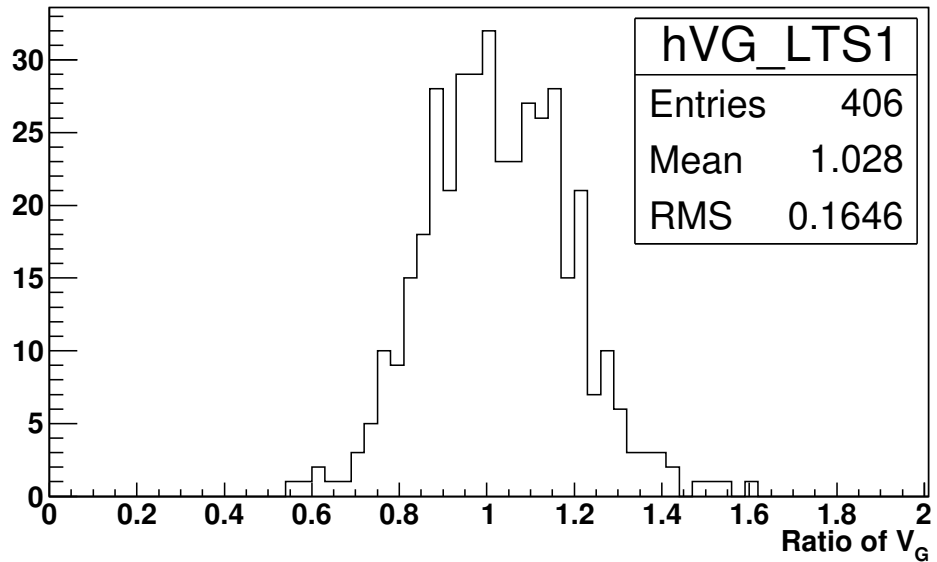


Figure 7.18

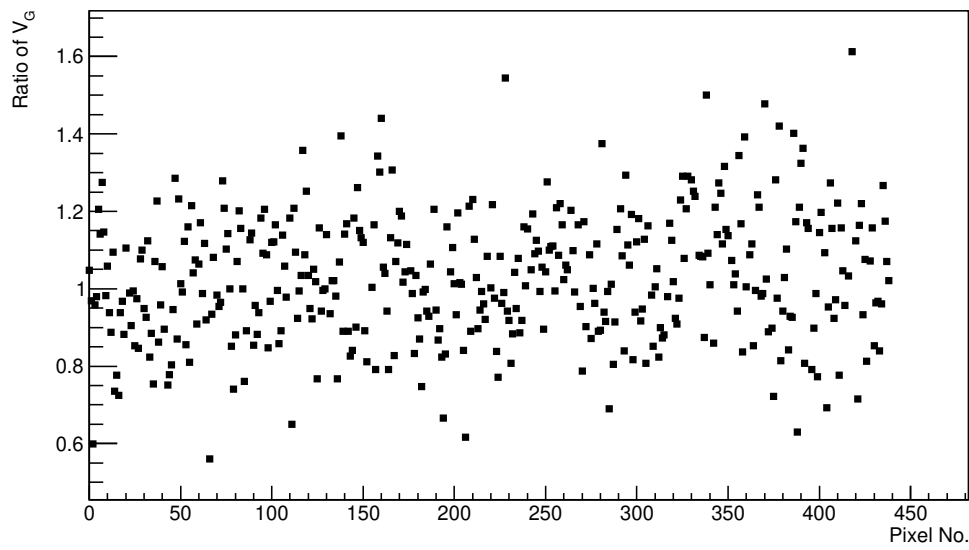


Figure 7.19

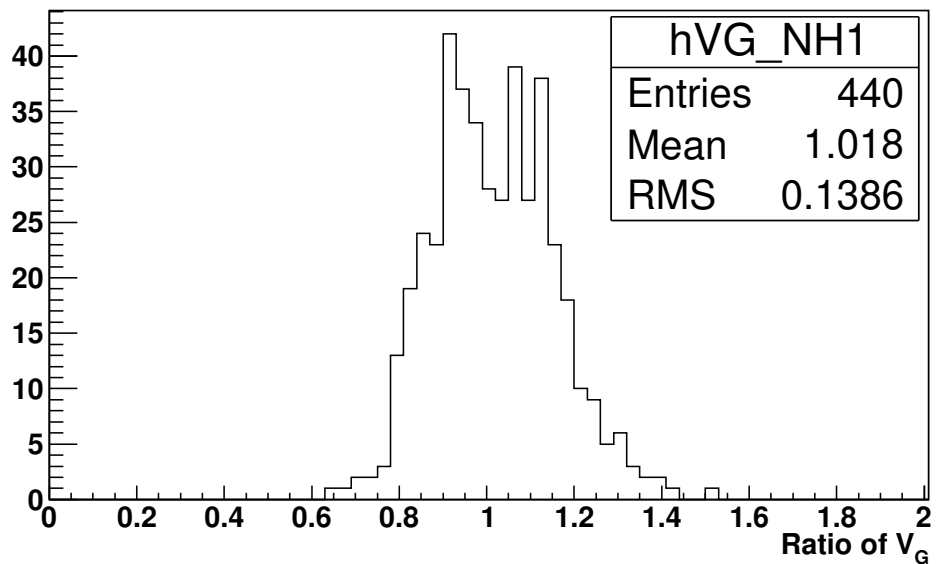


Figure 7.20

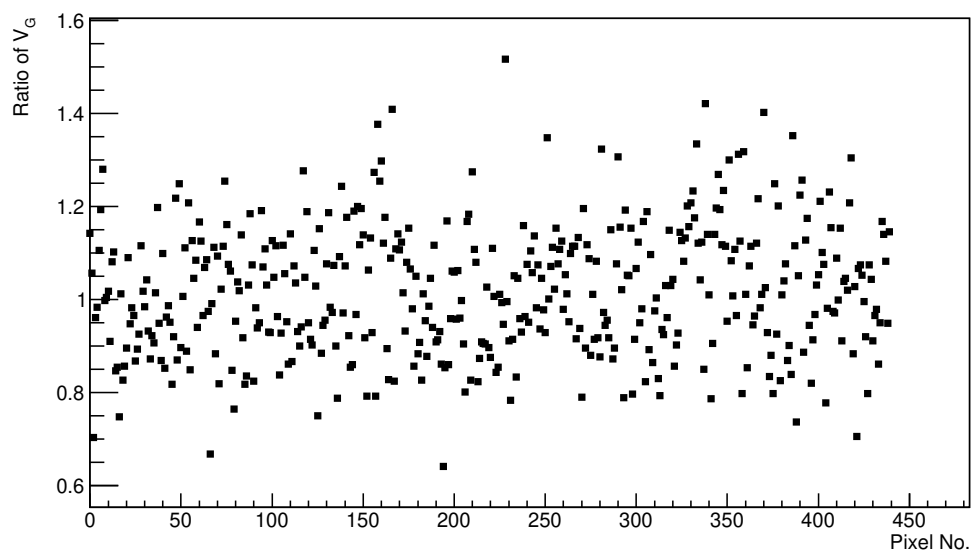


Figure 7.21

Chapter 8

Results of Fluorescence Detector Photomultiplier Gain Variance from CalA Data

Chapter 9

Laboratory Simulation of FD shift

Laboratory Simulation of FD shift under differing NSB levels.

- Measurements for both 900V and 600V (900V used as baseline)
- Different length shifts
- Changing NSB
- measuring how the relevant Gain changes throughout a run

9.1 Motivation

9.2 Method and equipment set-up

9.3 Results

9.4 Discussion

9.5 Conclusion

Chapter 10

Evaluation of Cloud Cuts on Auger Event Data

First look into the effectiveness of the Cloud cuts on Auger Golden Hybrid data from 2004 to 2018. I investigated the effects of removing the cloud cut from the list of quality cuts. This list includes cuts to remove events within known bad data taking periods, cuts on aerosol levels, event quality etc. Below is an example of a cuts file that is used within Auger.

This investigation was done to quantify the effects that the cloud cuts had on the data set. A question had been raised about whether the quality cuts on fitted values, Chi2 and requiring events with large gaps were doing the same job as the cloud cuts. There is a lot of uncertainty about whether a detected cloud had impacted each events.

Cloud information has large uncertainty about quantities like cloud height, distance from telescopes and timing. The timing uncertainty is due to atmospheric data being snapshots with time gaps between shots. Examples are Cloud camera scans are performed every 5 minutes. A cloud could move quite a far distance within this time.

10.1 Equipment used to detect cloud over the array

IR Cloud Cameras - Two version of IR camera has been running in tandem with the operation of the FD's. Find dates of operation

GOES Satellite data

CLF and XLF

LIDAR

10.2 Method - Cloud Flags and Their Impact

Take reconstructed Golden Hybrid events from 2004 to 2018

Extract camera flag data.

Two set of camera flags - positive ones that say that an event has pass one of the conditions saying that these is no cloud. the negative flags say that the event has failed to pass any of the test looking for clouds. If the flag is zero then there is no cloud information available.

Four different flags - IR Cloud camera, LIDAR, GOES satellite data and something else.

Look at the histograms of Xmax distributions for data passing cloud cuts, data failing cloud cuts and combined.

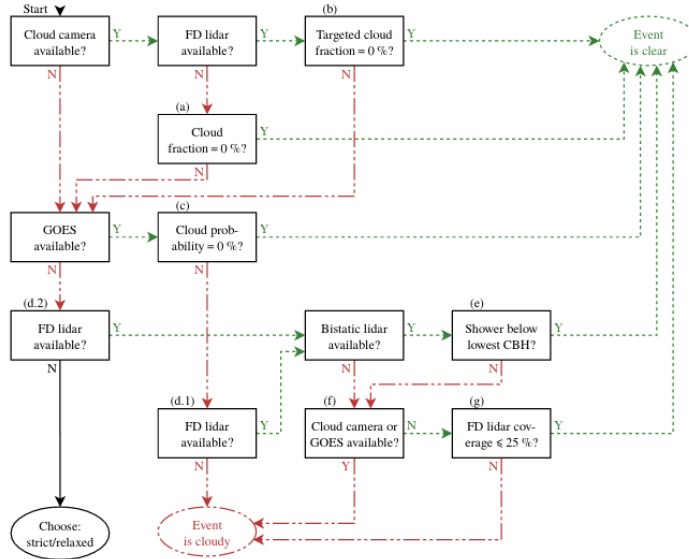


Figure 3: The cloud cut procedure for event analysis. Boxes represent steps of the procedure and ellipses represent exit points. Each step poses a question which may be answered “yes” (Y) or “no” (N). Refer to the text for detail on the steps labelled (a) through (g).

Figure 10.1: Diagram of how the cloud cuts are applied to the data set when called with the Auger event selection program.

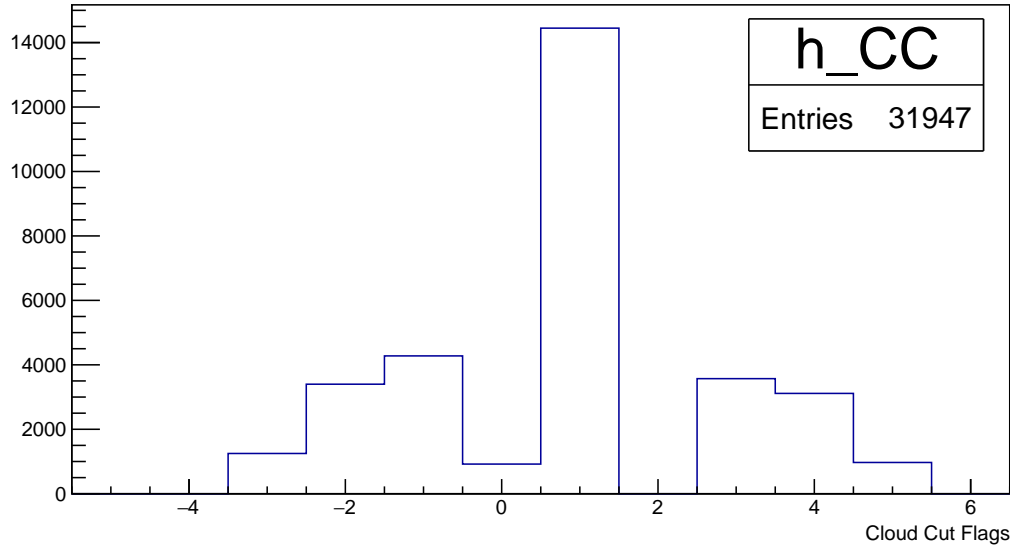


Figure 10.2: Distribution of cloud flags. Positive flag values are for events that would pass one of the cloud cuts. Negative flag values are for events that would one of the cloud cuts. A flag value of zero is for events that have no cloud data.

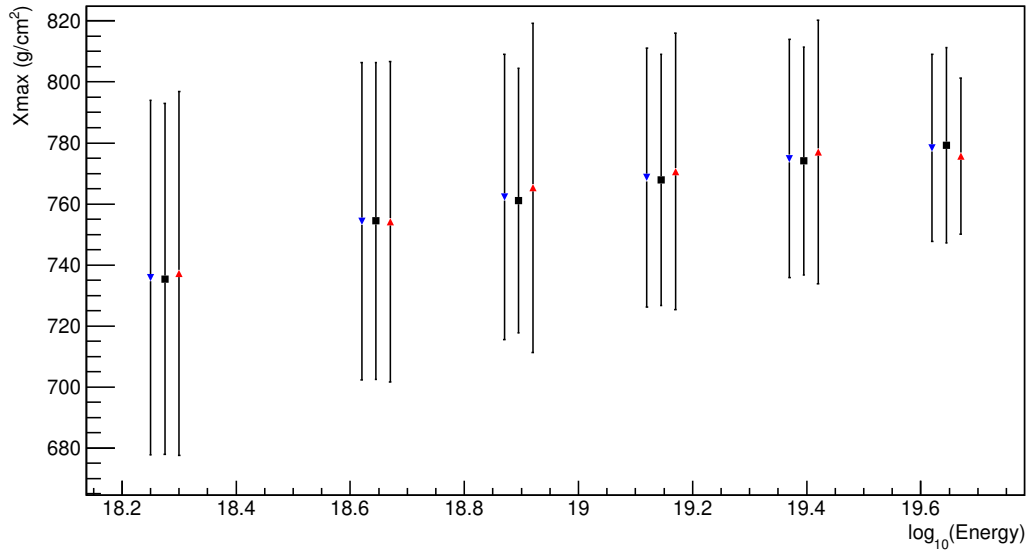


Figure 10.3: Elongation Rate with Cloud cuts applied (blue downward triangle), without any cloud cuts (black square) and only events that would fail the cloud cuts (red upward triangle).

10.3 Results - Effect on Mean Xmax and Spread in Xmax

- Cloud Cut Flags distribution
 - Xmax distributions within energy bins
 - Elongation rate
 - Is distance to Xmax or distance to shower axis needed?

10.4 Discussion - Are we being too conservative?

Gaining 30% more events cut is removed

Have to be careful of outliers

Mean Xmax and spread in Xmax does not change significantly

With cloud cut confident that events that could be cloud effected are removed. Without the cloud cut no significant impact is seem expect for the increase of statistics by 30%.

10.5 Conclusion

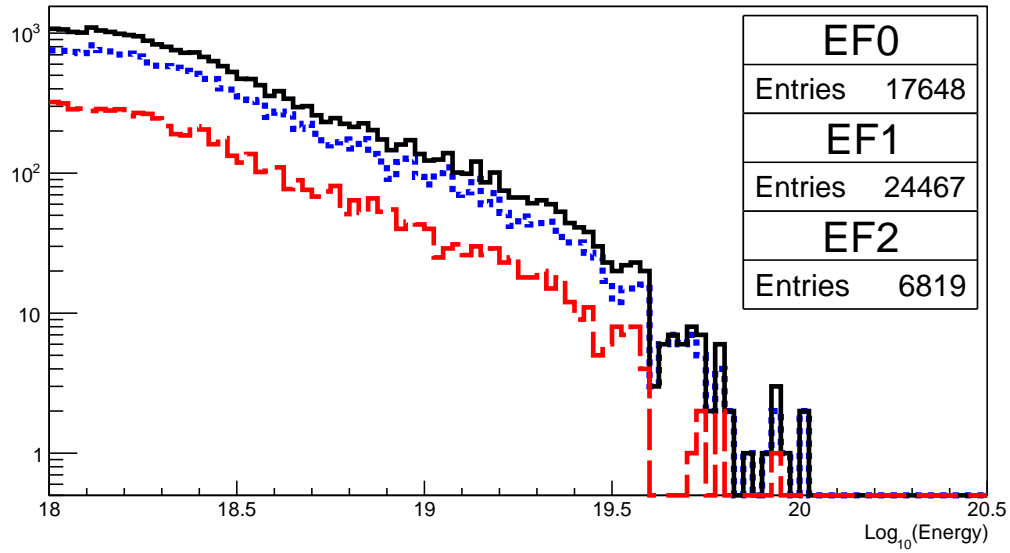


Figure 10.4: Distribution of the energy of events within the bin of $\log(E)$ of 18.0 to 20.5. Black (EF1) denotes events that passed with cloud cut removed, blue (EF0) denotes events that would pass the cloud cuts and red (EF2) denotes events that would fail the cloud cuts. All other cuts used for the ICRC19 have been applied.

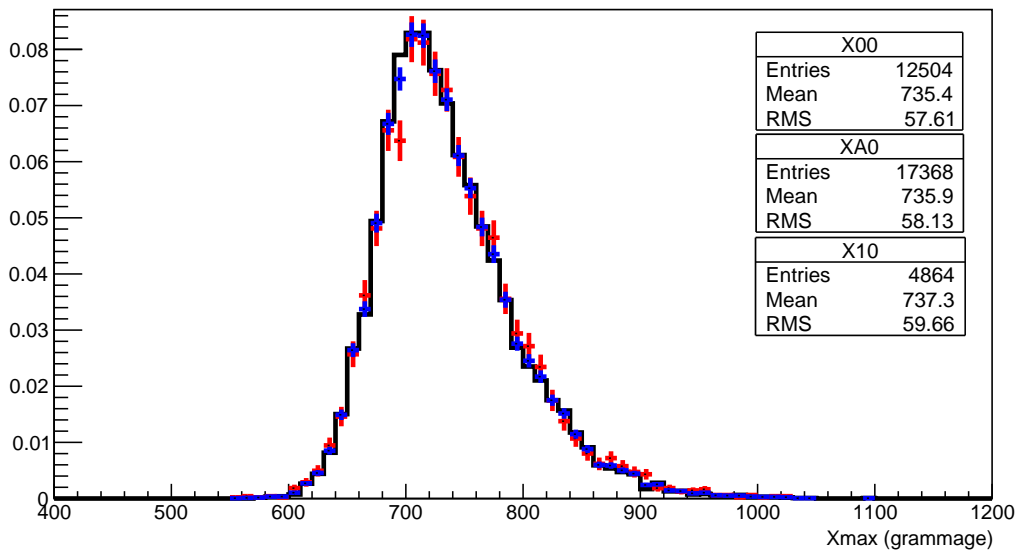


Figure 10.5: Distribution of the X_{max} of events within the bin of $\log(E)$ of 18.0 to 18.5. Black (XA0) denotes events that passed with cloud cut removed, blue (X00) denotes events that would pass the cloud cuts and red (X10) denotes events that would fail the cloud cuts. All other cuts used for the ICRC19 have been applied.

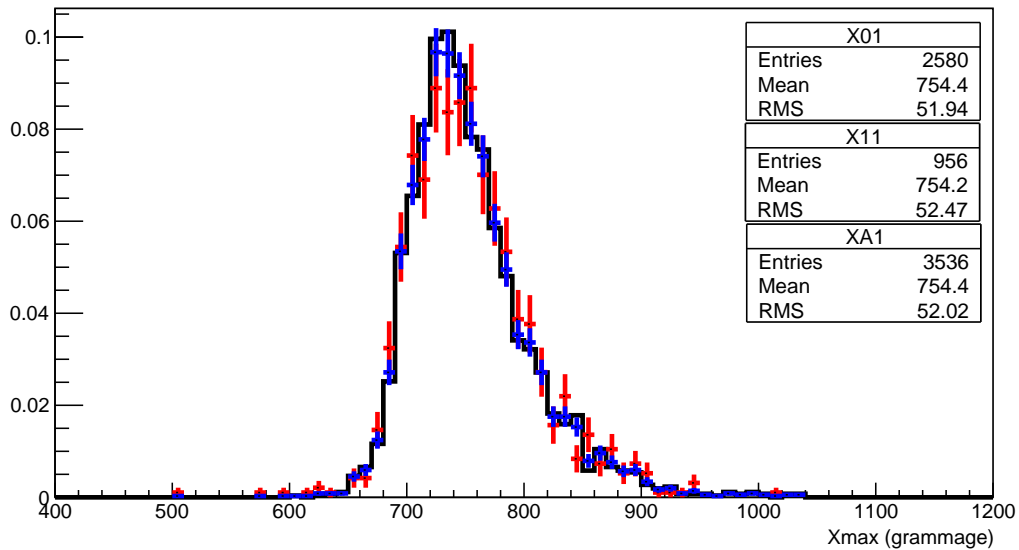


Figure 10.6: Distribution of the X_{max} of events within the bin of $\log(E)$ of 18.5 to 18.75. Black (XA1) denotes events that passed with cloud cut removed, blue (X01) denotes events that would pass the cloud cuts and red (X11) denotes events that would fail the cloud cuts. All other cuts used for the ICRC19 have been applied.

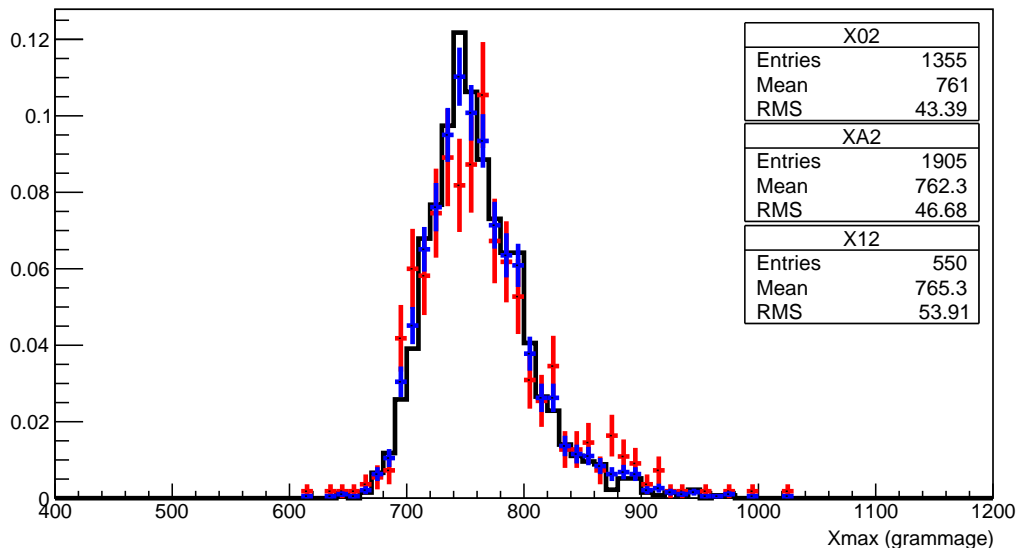


Figure 10.7: Distribution of the X_{max} of events within the bin of $\log(E)$ of 19.0 to 19.25. Black (XA2) denotes events that passed with cloud cut removed, blue (X02) denotes events that would pass the cloud cuts and red (X12) denotes events that would fail the cloud cuts. All other cuts used for the ICRC19 have been applied.

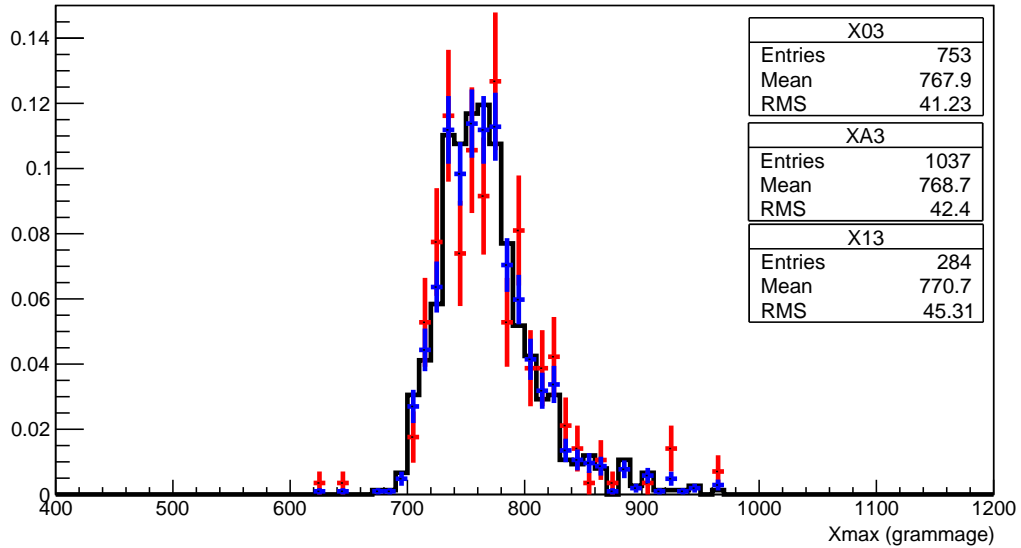


Figure 10.8: Distribution of the X_{max} of events within the bin of $\log(E)$ of 19.0 to 19.25. Black (XA3) denotes events that passed with cloud cut removed, blue (X03) denotes events that would pass the cloud cuts and red (X13) denotes events that would fail the cloud cuts. All other cuts used for the ICRC19 have been applied.

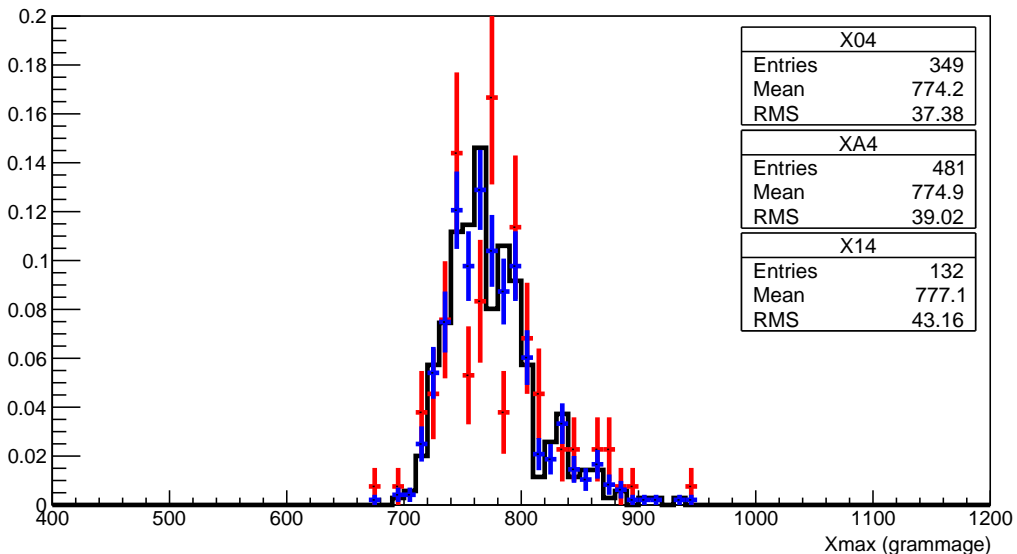


Figure 10.9: Distribution of the X_{max} of events within the bin of $\log(E)$ of 19.25 to 19.5. Black (XA4) denotes events that passed with cloud cut removed, blue (X04) denotes events that would pass the cloud cuts and red (X14) denotes events that would fail the cloud cuts. All other cuts used for the ICRC19 have been applied.

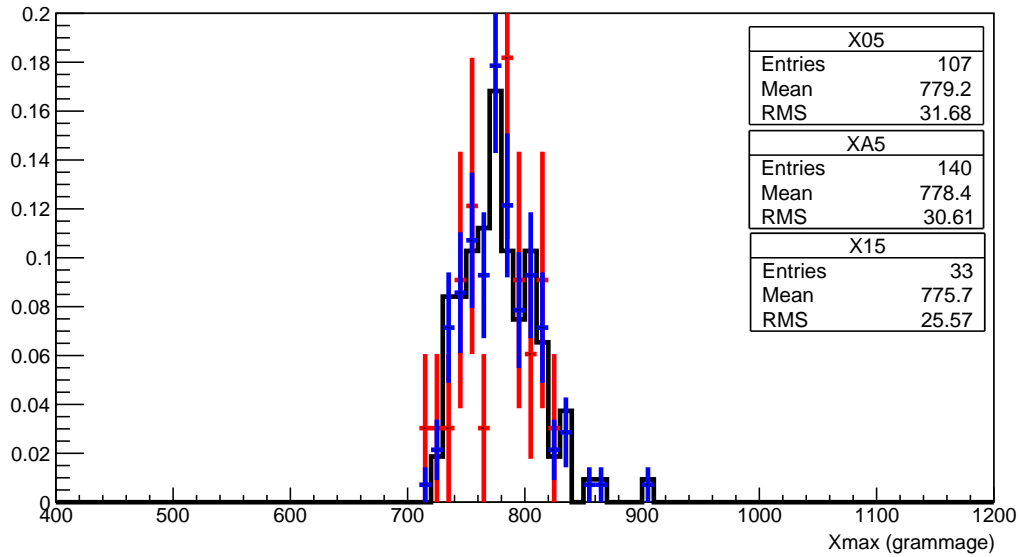


Figure 10.10: Distribution of the X_{max} of events within the bin of $\log(E)$ of greater than 19.5. Black (XA5) denotes events that passed with cloud cut removed, blue (X05) denotes events that would pass the cloud cuts and red (X15) denotes events that would fail the cloud cuts. All other cuts used for the ICRC19 have been applied.

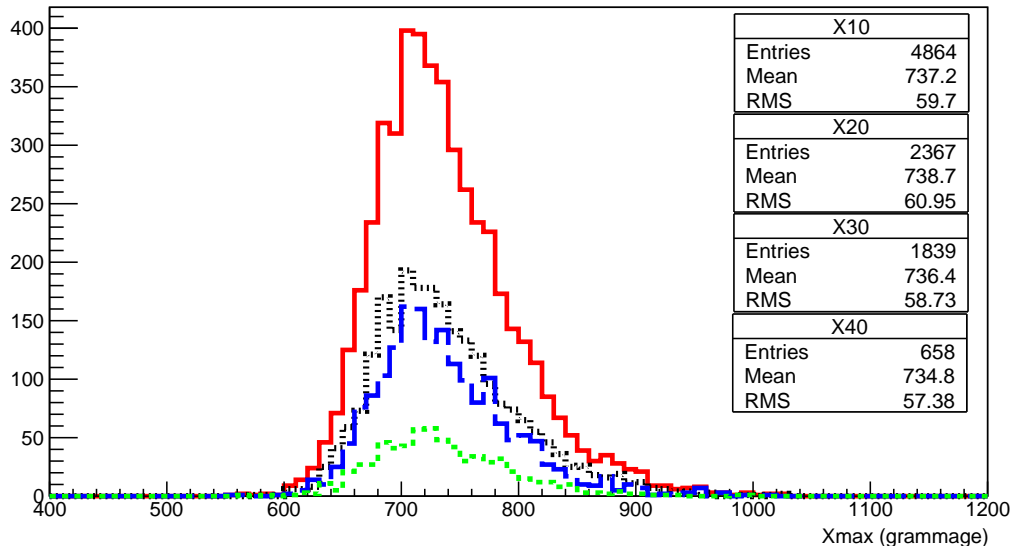


Figure 10.11: Distribution of the energy of events within the bin of $\log(E)$ of 18.0 to 18.5. Red (X10) denotes all event that failed the cloud cuts, black (X20) denotes events that failed the cloud camera/lidar cut, blue (X30) denotes events that failed the GOES data cut and green (X40) are events that have fail a combination of CLF/XLF, GOES and Cloud camera cut.

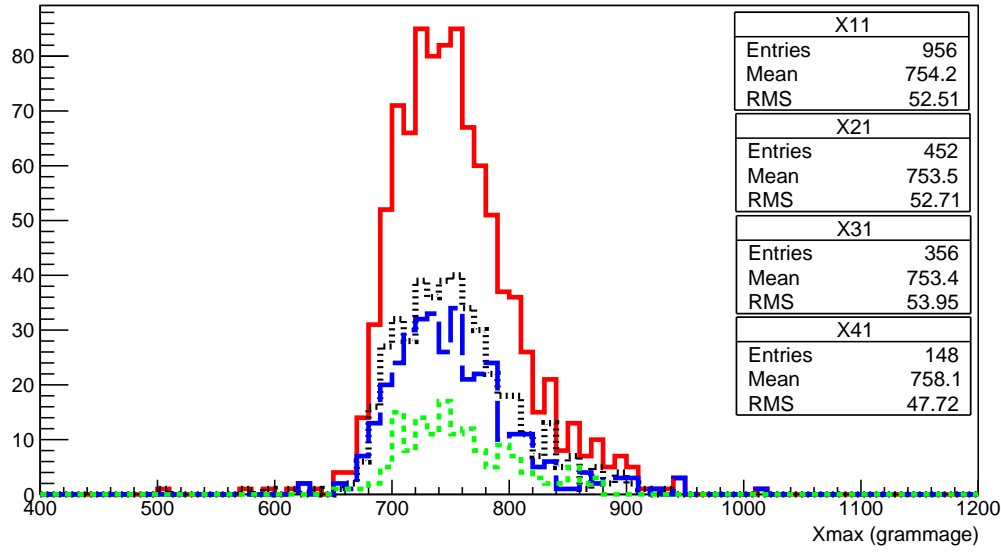


Figure 10.12: Distribution of the energy of events within the bin of $\log(E)$ of 18.5 to 18.75. Red (X11) denotes all event that failed the cloud cuts, black (X21) denotes events that failed the cloud camera/lidar cut, blue (X31) denotes events that failed the GOES data cut and green (X41) are events that have fail a combination of CLF/XLF, GOES and Cloud camera cut.

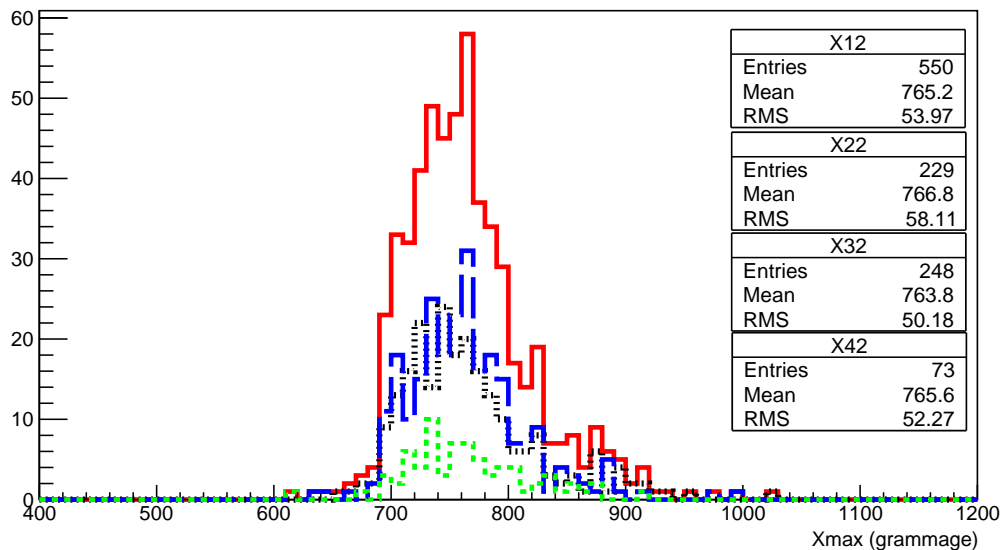


Figure 10.13: Distribution of the energy of events within the bin of $\log(E)$ of 18.75 to 19.0. Red (X12) denotes all event that failed the cloud cuts, black (X22) denotes events that failed the cloud camera/lidar cut, blue (X32) denotes events that failed the GOES data cut and green (X42) are events that have fail a combination of CLF/XLF, GOES and Cloud camera cut.

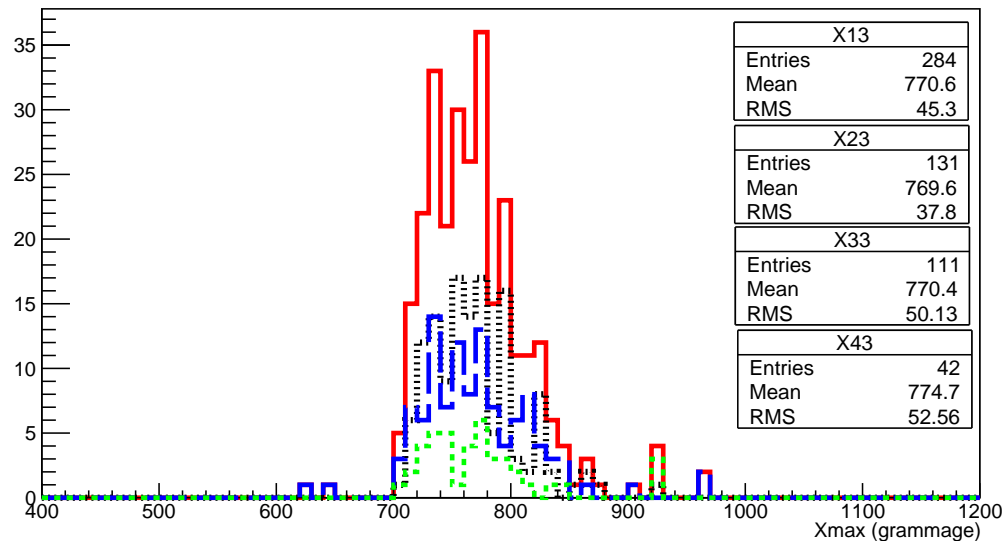


Figure 10.14: Distribution of the energy of events within the bin of $\log(E)$ of 19.0 to 19.25. Red (X13) denotes all event that failed the cloud cuts, black (X23) denotes events that failed the cloud camera/lidar cut, blue (X33) denotes events that failed the GOES data cut and green (X43) are events that have fail a combination of CLF/XLF, GOES and Cloud camera cut.

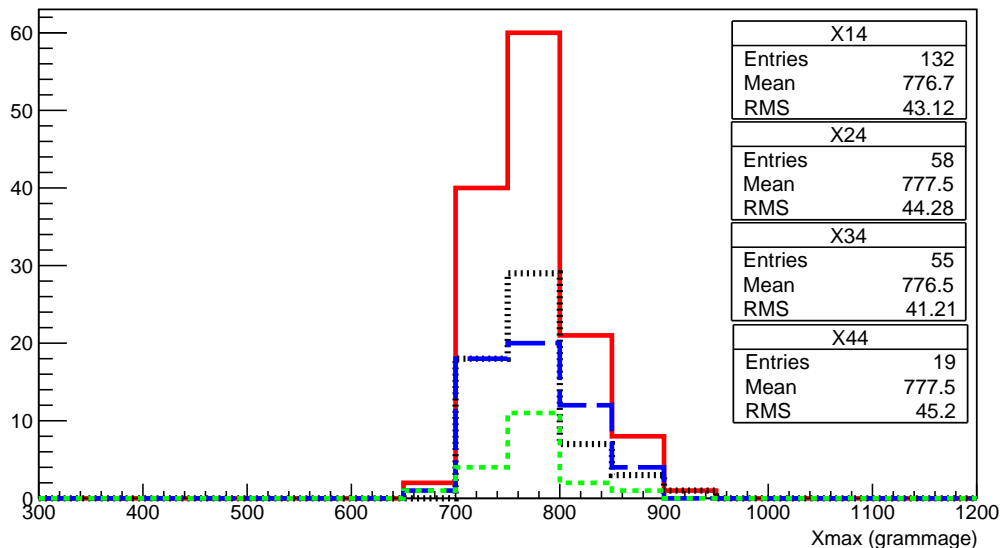


Figure 10.15: Distribution of the energy of events within the bin of $\log(E)$ of 19.25 to 19.5. Red (X14) denotes all event that failed the cloud cuts, black (X24) denotes events that failed the cloud camera/lidar cut, blue (X34) denotes events that failed the GOES data cut and green (X44) are events that have fail a combination of CLF/XLF, GOES and Cloud camera cut.

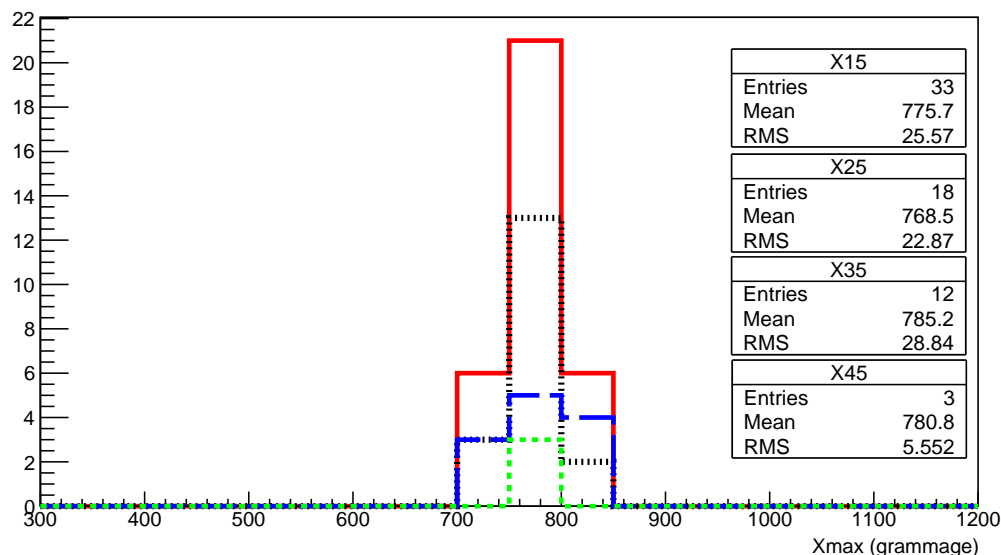


Figure 10.16: Distribution of the energy of events within the bin of $\log(E)$ of greater than 19.5. Red (X15) denotes all event that failed the cloud cuts, black (X25) denotes events that failed the cloud camera/lidar cut, blue (X35) denotes events that failed the GOES data cut and green (X45) are events that fail a combination of CLF/XLF, GOES and Cloud camera cut.

Chapter 11

Conclusion

11.1 Future Work

Bibliography

- [1] W. Heitler, *The quantum theory of radiation*. Oxford: (Clarendon Press, Ed. 3, Oxford), 1954. (Cited on page 9.)